Structural Characterization of Dynamic Protein Machines by Cryo-electron Microscopy

by

Adam Lee Yokom

A dissertation in partial fulfillment
of the requirements for the degree of
Doctor of Philosophy
(Chemical Biology)
in The University of Michigan
2017

Doctoral Committee:

Associate Professor Daniel Southworth, Chair
Professor Yoichi Osawa
Professor Stephen W. Ragsdale
Associate Professor Raymond C. Trievel

Adam Lee Yokom
alyokom@umich.edu
ORCID iD:0000-0002-3746-7961

Dedication

My dissertation is dedicated to my parents Larry and Robin Yokom. Throughout my life they have given all the support and freedom I have required to explore, learn and satisfy my inherent curiosity. Having their encouragement allowed me to take on all challenges and trials leading me to where I am today.

Acknowledgements

I would like to thank my thesis mentor, Daniel Southworth for taking me into his lab and guiding me into the scientist I am today. Dan has taught me a great deal through the years not only in my thesis research but also in life outside of research. The impact of his guidance will continue with me for decades to come. Also, I would like to thank my committee members; Yoichi Osawa, Raymond Trievel and Stephen Ragsdale for continual advice on my thesis research. Likewise, the numerous mentors who fueled my early interest in science while studying at Oakland University deserve recognition. Namely, my organic chemistry teacher, Arthur Bull and my research advisor, John Finke both whom were always encouraging, kind and supportive.

I would like to acknowledge, thank and applaud my lab mates for their support throughout my PhD research. Especially, Eric Tse, who has been thoroughly involved in all aspects of my research but in addition has become a wonderful, caring friend. As well, Min Su offered me an immense amount of training, conversation and advice. Additionally, I would like to thank all those in the Michigan scientific community, especially in the Program in Chemical Biology cohort of 2012 and other structural biology labs who I have had the pleasure of interacting with and cherish as coworkers and friends.

I express my love and thanks to my parents, Larry and Robin Yokom and my brother Allen Yokom. All whom have given tremendous support throughout this process. It would be unjust to say only those mentioned here are deserving of my acknowledgements, therefore I would like to thank those who have helped in anyway. Every small or large act of friendship, support, advice, or encouragement was treasured and got me to the end of this five year process.

Lastly, I would like to thank the person who has had to deal with all my ups and downs throughout my PhD, my wife, Stephanie Gates. Having meet someone who understands the rigors of research and also shares my passion in all aspects of life is an incredible blessing. Stephanie makes for the perfect partner and aided immensely in my ability to obtain my PhD.

Table of Contents

List of Figures

List of Tables

List of Abbreviations

AAA+	ATPases Associated with diverse cellular Activities
ATP	Adenosine triphosphate
ADP	Adenosine diphosphate
AMPPNP	Adenylyl-imidodiphosphate
ATPγS	Adenosine 5′-[γ-thio]triphosphate
BH_4	(6*R*)-5,6,7,8-tetrahydro-L-biopterin
CaM	Calmodulin
CXL	Crosslinked
CTD	C-terminal Domain
DED	Direct electron detector
DQE	Dynamic quantum efficiency
EM/TEM	Electron Microscopy/Transmission Electron Microscopy
FAD	flavin adenine dinucleotide
FMN	flavin mononucleotide
eNOS	endothelial Nitric Oxide Synthase
HSP	Heat Shock Proteins
iNOS	inducible Nitric Oxide Synthase
ISAC	Iterative stable alignment and clustering
M_W	Molecular weight

M_{WAA}	Molecular weight calculated from amino acids seqeuce
NTD	N-terminal Domain
MD	Middle Domain
Oxy	Oxygenase
RCT	Random Conical Tilt
Red	Reductase
SEC-MALS	Size Exclusion Chromatography and Multi-angle Light scattering

Abstract

Conformational changes of proteins are a primary factor for proper cellular signaling, protein folding and substrate interaction. Specifically, molecular chaperones, which are required to maintain protein homeostasis, traverse large conformational landscapes to bind client proteins. However, studying the conformational changes in these proteins has long been a challenge. Recent advancements in electron microscopy (EM) have dramatically improved our ability to capture protein conformational states. Therefore, EM was utilized as a structural tool to further our understanding of two dynamic protein systems, Heat shock protein 104 (Hsp104) and nitric oxide synthase (NOS).

Yeast Hsp104 is a powerful disaggregase that functions to pull apart amorphous and amyloid aggregates. Hsp104 contains two AAA+ domains which, through a mechanism not fully understood, translocates substrate through its central channel. Cryo EM 3D reconstructions of three unique Hsp104 conformations have been determined. Hsp104-AMPPNP was observed in an open state (5.6Å) and shows a large asymmetric offset around the AAA+ domains. This spiral arrangement of the AAA+ domains creates a unique heteromeric NBD1-NBD2 interaction. Furthermore, the open state captured structural information on many critical regulatory domains, such as the middle domain, N-terminal domain and C-terminal domain. 3D classification of a substrate bound Hsp104-ATPγS complex revealed a mix of closed and extended states

to ~4Å resolution. Tyrosine pore loop contacts are seen to interact directly with the polypeptide backbone threaded into the central channel of the Hsp104 hexamer. Moreover, these structures revealed a two-residue translocation step for substrate threading in Hsp104. Together these high-resolution reconstructions have led to a novel model of Hsp104 function, which encompasses both nonprocessive and processive substrate translocation.

Secondly, EM techniques were used to study Nitric Oxide Synthase (NOS). NOS is a critical signaling protein and is the sole source of NO within mammals. NOS involves a complex electron transfer cycle to convert L-arginine to NO and L-citrulline. This vital enzyme has been a challenge to study structurally, and full-length information has been lacking. By utilizing 2D and 3D classification methods we were able to obtain the first full-length structure of nNOS bound to its critical regulatory partner, calmodulin (CaM). 2D analysis revealed a large degree of flexibility around the NOS dimer showing both open, intermediate and closed states. By using glutaraldehyde crosslinking and random conical tilt, a 23Å reconstruction of nNOS-CaM showed how CaM binding allows FMN ‘deshielding’. The FMN domain undergoes a 115° rotation away from the flavin core, and toward the heme co-factor allowing for efficient electron transfer and subsequent NO production. Mechanistic, structural and functional information have been determined for both Hsp104 and NOS and the details of these studies follow.

Chapter 1 – Introduction

1.1 Protein conformational changes are required for function

Large scale dynamics are vital aspects of all biological macromolecules. These dynamics assist to conserve, modify or induce function within all aspects of biology. Specifically, these changes are crucial for both protein homeostasis and cellular signaling processes (Grant et al., 2010). There are two main types of large scale dynamics which occur; energy dependent and independent. Energy-dependent changes regularly rely on the hydrolysis of ATP or GTP to produce domain rearrangements. Nucleotide dependent machines, such as molecular chaperones, are a prime example of this type of energy dependent process. These molecular machines cycle through apo, ATP and ADP-bound states to modulate substrate binding affinities (Gutteridge and Thornton, 2004). Molecular chaperones use this cycle to maintain protein homeostasis within the crowded cellular environment (Hartl et al., 2011).

Energy independent motions frequently function by using complicated allosteric mechanisms to induce similar conformational cycles. These changes commonly occur around highly flexible regions. Flexible linker regions tether larger protein domains together and randomly change position in solution. Energy independent changes are especially important for membrane proteins which respond to extracellular ligand binding for allosteric conformational change and intracellular signaling (Nishida et al., 2014). Both types of conformational change can correspond to ligand binding, protein-

protein interactions and cellular processes (Henzler-Wildman and Kern, 2007; van den Bedem and Fraser, 2015). Since nearly all systems in biology undergo conformational changes, the study of proteins in motion has been a difficult target for structural biologists. This problem is particularly challenging within weak affinity complexes, such as those found in the protein quality control network, or proteins with large flexible regions. Traditional protein structure determination techniques such as X-ray crystallography, nuclear magnetic resonance (NMR), and hydrogen-deuterium exchange mass spectroscopy have been ineffective at capturing large conformational motions. However, the use of single particle electron microscopy can be an efficient tool to study these conformational changes and was the main technique used for my thesis research, as described in detail in Chapter 2.

1.2 Heat shock proteins in protein quality control

Heat shock response

Heat Shock Proteins (HSP) are a family of molecular chaperones which are critical during all aspects of cellular life. Under normal cellular conditions HSPs are expressed at basal levels. Hsp70, Hsp90, Hsp40 and Hsp100s maintain proteostasis and monitor protein quality control pathways (Jeng et al., 2015). HSPs are highly upregulated in the cell stress response network (Liu, 1997), an event that is triggered by Heat shock factor 1 (HSF1). HSF1 transitions from a monomeric to a trimer state during cell stress, prompting binding to target promoter regions on DNA to transcribe HSPs (Figure 1-1) (Krivoruchko and Storey, 2010). These HSPs play vital roles in thermal tolerance and cell protection mechanisms.

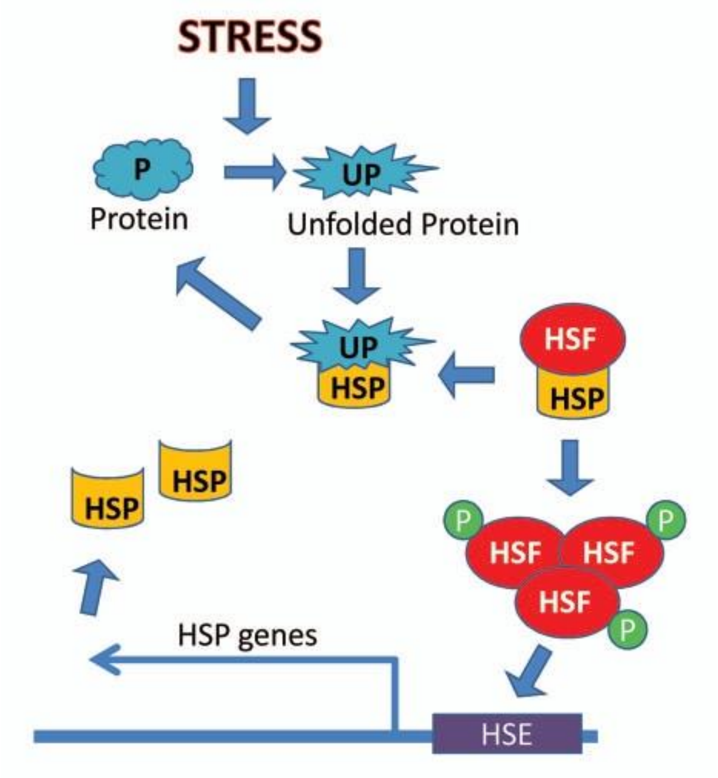

Figure 1-1 Cellular heat shock response Diagram depicting the cascade of heat shock response within the cell. HSF trimers upregulated the chaperone machinery at the DNA level. (Krivoruchko and Storey, 2010)

The HSP network functions in folding, unfolding, degradation and disaggregation of proteins and is conserved throughout bacteria and eukaryotic organisms (Liu, 1997). Hsp70 and Hsp90 are HSP family members that have been extensively characterized across many species, and maintain a large portion of quality control functions (Proctor and Lorimer, 2011; Stephanou and Latchman, 2011). Hsp70 and Hsp90 both function by utilizing energy dependent conformational changes to cycle through substrate binding states, facilitating client binding and release.

Conformational Cycles of Hsp70/90

Hsp70 cycles between a high substrate affinity, ADP state and a low substrate affinity, ATP state. This nucleotide exchange induces numerous conformational changes, namely where the ‘lid’ region swings between binding to the nucleotide binding domain (NBD) in the presence of ATP and binding the substrate binding domain (SBD) in the post hydrolysis state when ADP is bound (Figure 1-2) (Zhuravleva and Gierasch, 2015). In this ADP bound state Hsp70 can stabilize unfolded proteins and allow for proper folding pathways to transpire. Hsp70 hydrolysis is regulated by another chaperone, Hsp40, which stimulates nucleotide exchange and thus modulates client binding. Additionally, Hsp70 plays a critical role in the ubiquitin proteasomal degradation pathway. Hsp70 can bind the E3 ubiquitin ligase, carboxyl terminus of Hsc70 interacting protein (CHIP), to mark misfolded proteins for degradation (Luo et al., 2010). An example of a client of the Hsp70/CHIP targeted degradation is nitric oxide synthase (NOS) (Pratt et al., 2010). NOS forms a functional dimer, and when properly folded NOS is protected from Hsp70/CHIP ubiquitination. However, when NOS becomes misfolded, it transitions to monomeric NOS. This monomeric state is recognized by the Hsp70/CHIP ubiquitin machinery, and ubiquitinated NOS is degraded by the proteasome, thus protecting the cell from toxic misfolded proteins.

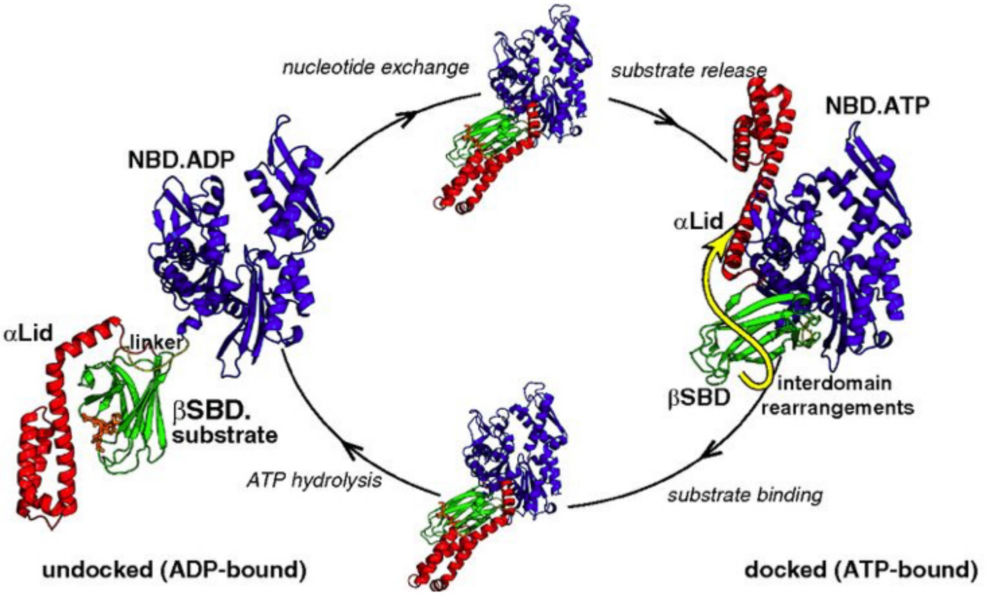

Figure 1-2 Conformational cycle of Hsp70 Hsp70 undergoes large conformational cycling balancing substrate affinity with nucleotide state. The majority of this motion revolves around the 'lid' regions flexibility (Zhuravleva and Gierasch, 2015).

Hsp90 undergoes a similar nucleotide dependent conformational cycle where hydrolysis greatly influences the overall domain architecture (Hessling et al., 2009; Southworth and Agard, 2008). This cycle also controls substrate binding affinity and function of Hsp90. Hsp90 is a functional homodimer, differing from the monomeric state of Hsp70. Hsp90s conformational cycle involves an apo, open state, (Figure 1-3) (Li and Buchner, 2013), and a closed, ATP bound and catalytically active state. The transition between these states is a highly dynamic process, regulated by cochaperones and client binding. Functionally, Hsp90 is thought to act downstream of Hsp70 in protein folding and to fuel proper maturation of many client proteins (Wayne et al., 2011). This protein maturation process is critical for numerous proteins in cellular signaling and quality control pathways.

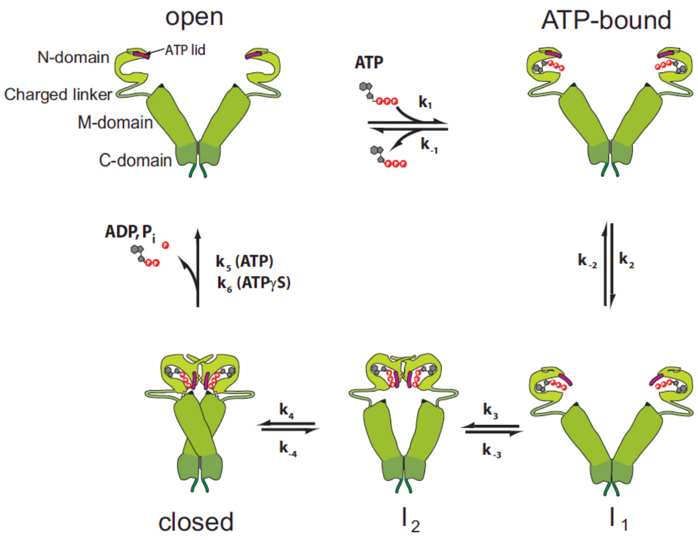

Figure 1-3 Hsp90 nucleotide dependent cycle Hsp90 is known to have a large degree of conformational change during apo, ATP and ADP bound states. This states are critical in the regulation and binding of client proteins (Li and Buchner, 2013).

An example of Hsp90 aiding in protein maturation is the insertion of heme into the NOS oxygenase domain (Peng et al., 2012). Heme serves as a critical catalytic co-factor for NOS and is required NOS dimerization (Chen et al., 2002). For proper heme insertion, Hsp90 binds to the heme binding cleft of monomeric NOS. Without Hsp90 interaction, heme incorporation is depleted and NOS becomes incapable of forming dimeric complexes. This lack of dimerization would subsequently result in NOS ubiquitination by Hsp70/CHIP. Often a balance of Hsp70/90 function is a critical aspect of protein quality control and is supported via a large set of other chaperones and co-chaperones (Pratt et al., 2010). One such chaperone is Hsp104, which is described in more detail below and collaborates with Hsp70 and Hsp40. Of note, the nature of the HSP chaperone network relies on weak, transient client binding interactions and large dynamic conformational cycles. As a consequence, structural determination of both clients and chaperones is challenging, therefore many of aspects of the HSP network lack structural characterization.

1.3 Heme containing enzymes as client proteins

Heme containing enzymes

Client proteins are processed by chaperone machines to become fully folded or mature. One such client is NOS, which is heavily involved in the triage decisions of HSPs. Cytochrome P450s along with NOS make-up the heme mono-oxygenase super family of proteins that serve as chaperone client proteins (Correia et al., 2011). Heme mono-oxygenases perform a wide range of catalytic functions from drug metabolism to NO synthesis. These enzymes function through a conserved heme co-factor, FMN and FAD to activate molecular oxygen for electron transfer. Cytochrome P450s require a similar insertion of heme for protein maturation and function. Cytochrome P450s have been highly studied due to their role in drug metabolism. There are four classes of P450 enzymes which have a range of structural tethers and functions (Figure 1-4) (Roberts et al., 2002). Class 1 and 2 are untethered and interact weakly without substrate, but affinity if greatly increased in the presence of substrate, while class 3 and 4 are tethered together via flexible linker regions. Important to my thesis work are the class 3 enzymes which are most homologous with nitric oxide synthase. A classic model for P450 function is BM3 a self-sufficient bacterial mono-oxygenase. Studying the BM3 system has revealed many of the intricate steps of catalysis and substrate binding for this enzyme (Munro et al., 2002). However, there are still major functional questions on the mechanism of heme monooxygenases. Specifically, the interaction between both tethered and untethered domains need to form for efficient electron transfer complexes. This complex formation for tethered P450s and NOS is thought to function through a variety of conformational states, but many questions remain due to the lack of full length structural information.

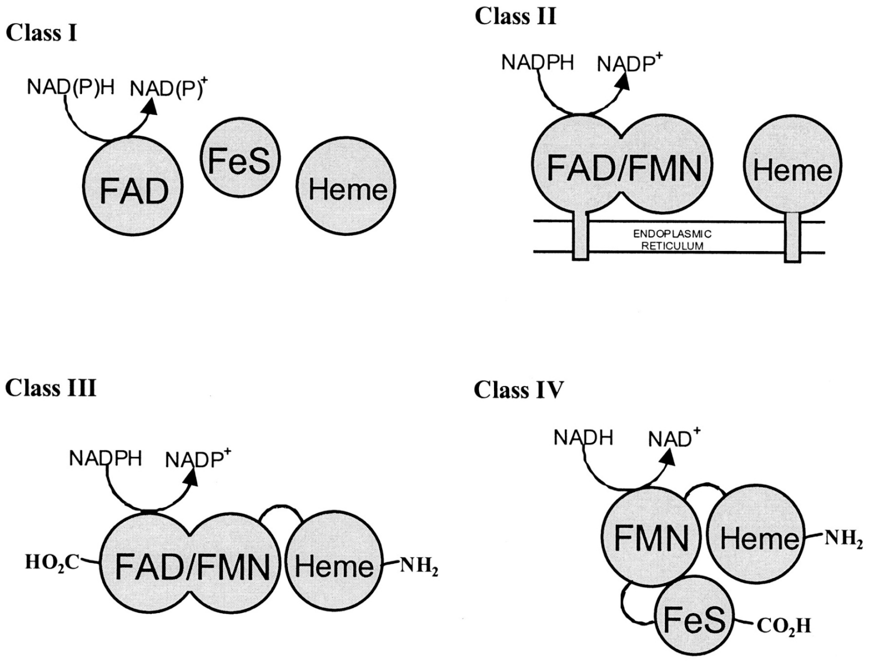

Figure 1-4 Schematic of p450 classes The family of p450s are broken down into four main classes. Shown here are the connections between co-factor domains and membrane associations of these classes (Roberts et al., 2002).

NOS function

Nitric Oxide (NO) serves as a common cellular signaling molecule triggering vasodilation, neuronal and immune responses. NO is synthesized by three Nitric Oxide Synthase (NOS) isoforms; endothelial (eNOS), neuronal (nNOS) and inducible (iNOS). Each isoform differs in NO production rate and their expression is tissue specific (Park et al., 2000). eNOS and nNOS require Calcium (Ca2+) release through cellular signaling cascades to trigger calmodulin (CaM) binding (Marletta, 1994). iNOS is regulated at a transcriptional level and is constitutively bound with CaM at all cellular Ca^{2+} concentrations. Therefore, iNOS is constitutively active and produces a large amount of NO. NOS generates NO via a two-step electron transfer cycle which catalyzes L-Arginine and molecular oxygen into L-citrulline and NO (Figure 1-5). The last step of this mechanism takes place when electrons from the heme prosthetic group are transferred to L-Arginine. The electron transfer mechanism has been shown to be limited by an upstream electron transfer step where electrons move from FMN to heme. This step also spans across the two major domains of NOS and is thought to require conformational changes.

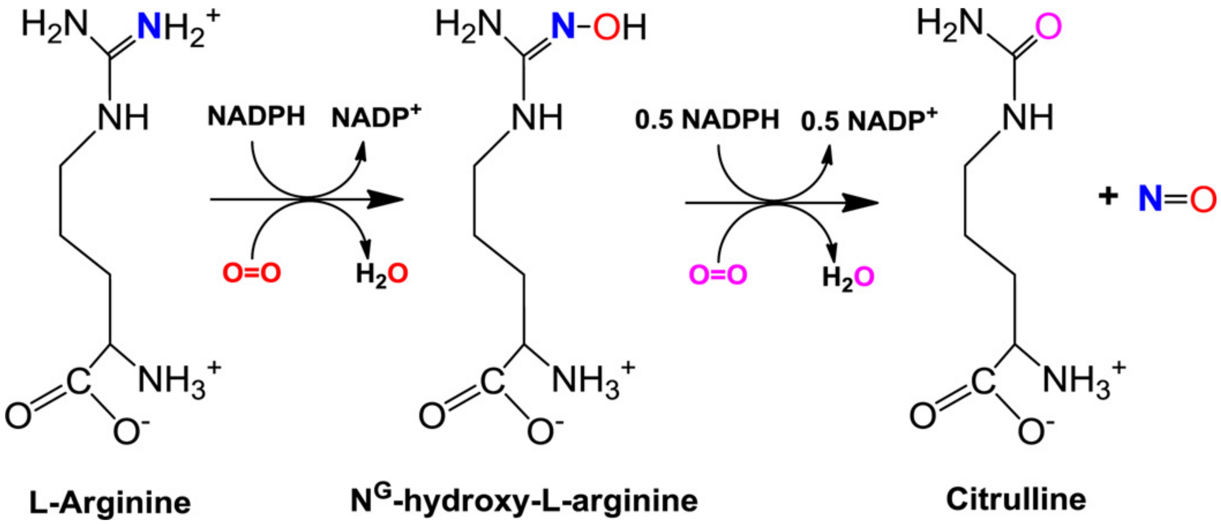

Figure 1-5 NOS two-step catalytic mechanism NOS utilizes a two-step conversion of L-arginine and molecular oxygen into L-citrulline and NO. This process goes through a N-hydroxyl-L-arginine intermediate (Feng, 2012)

Unregulated NOS electron transfer increases the number of reactive oxygen species (ROS) and causes aberrant damage to cells. Additionally, NOS has been shown to be upregulated in cancer and diabetes and increases the negative effects of ischemic shock (Förstermann and Sessa, 2012). The latter is caused by iNOS specifically and has been a target for inhibition for many years. However, developing selective inhibitors with isoform specificity has proven difficult (Poulos and Li, 2013). In the few inhibitors, presently available, there are many off target effects as they target NOS in all tissues. The pursuit of selective inhibitors has been hampered by a lack of full length structural information. This information can inform drug design schemes and improve our understanding of the NOS mechanism.

Electron Transfer cycle

Extensive mechanistic studies of NO production have elucidated the kinetic and biochemical properties of NOS isoforms (Marletta, 1994). Particular focus has been given to the study of the electron transfer path. Electron transfer starts with $NADP^+$, the highest redox potential co-factor bound in the Red domain. This electron rapidly transfers within the flavin core to FAD and then to FMN (Feng and Tollin, 2009). This cycle occurs with or without the binding of CaM, however FMN-heme transfer depends on CaM binding. As such, the FMN-heme transfer step is the rate limiting step during NO synthesis (Feng and Tollin, 2009). Structural predictions expect this rate limiting step to involve a large conformational change within the NOS dimer but this change has not been visualized (Figure 1-6). Additionally, this transfer step is known to occur in trans across the Oxy dimer. How NOS accommodates this transfer is likely through a distinct conformational change. Once the electron has successfully been transferred to the heme group, L-arginine is reduced and the process is repeated again for the second electron needed to form NO and the byproduct L-citrulline.

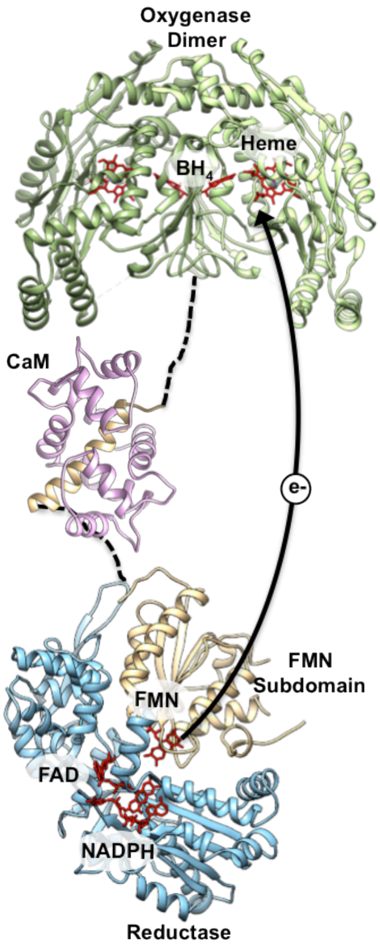

Figure 1-6 Proposed electron transfer path for NOS Domain structures of NOS (Oxy PDB=1RS9, Red PDB=1TLL, FMN:CaM=3HR4). Domain positions show the electron transfer path. Flexible linker regions flanking the CaM binding helix are shown as dotted line.

Structural elements of NOS isoforms

NOS contains three major domains; the N-terminus oxygenase (Oxy) domain, C-terminus reductase (Red) domain and a CaM binding helix (Figure 1-7). The Oxy domain binds the heme cofactor and serves as the binding site of Hsp90. Moreover, the Oxy domain contains binding sites for another co-factor, tetrahydrobiopterin and the ligand, L-arginine. The Red domain harbors the initial electron transfer steps in a flavin core, containing NADP, FMN and FAD co-factor binding sites. Lastly, a flexible linker between the Oxy and Red domains holds the CaM binding helix. This region is highly unstructured and is thought to contribute a large degree of conformational flexibility to NOS. nNOS and eNOS contain added regulatory domains such as the C-terminal (CT) and PDZ domains which are not present in iNOS (Figure 1-7). Both the Oxy and Red domains have been solved by x-ray crystallography but were crystallized outside the context of the full-length NOS dimer.

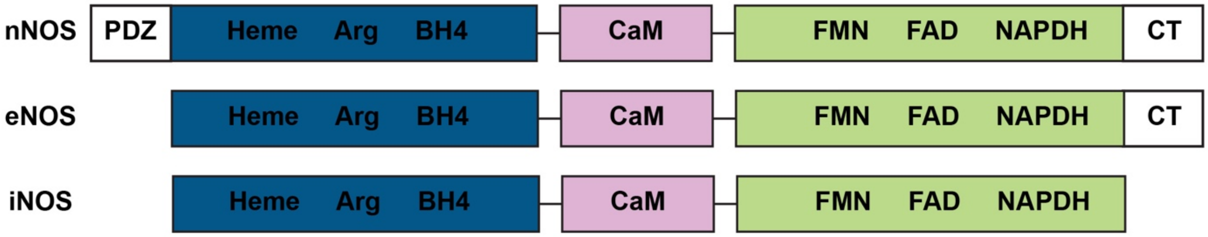

Figure 1-7 Domain cartoon of NOS isoforms

Since CaM binding is a critical regulator of NOS, many studies have focused on this interaction. Ca^{2+} release in the cell, fluctuating from 50 nM to >200 nM, is a main regulator of CaM binding (aside from the iNOS system which functions at basal concentrations). This release occurs through upstream cell signaling pathways. CaM binding begins with engagement of the C-lobe during lower Ca^{2+} concentration. This binding is of moderate affinity but allosterically increases binding of the N-lobe. As mentioned, CaM binding is thought to induce a large conformational change to facilitate FMN-heme electron transfer (Panda et al., 2006). It is proposed to require two types of protein interactions. First, the FMN domain, which is seen buried within the Red domain, needs to be dislodged and positioned in a ‘deshielded’ state (Figure 1-8). The flavin cofactors within NOS and p450s are known to form a tight core but rearrange for electron transfer, which is induced by CaM binding in NOS. Secondly, the position of the Red domain needs to come within proximity of the trans Oxy domains. The combination of these two movements opens the Red domain to engage the trans-Oxy domain and efficiently transfers electrons to the heme (Adak et al., 2001). This theory is supported by data that shows that CaM forms a docked state on the Oxy domain (Smith et al., 2013). Additionally, CaM binding may partially block the Hsp70 binding site, in turn maintaining the pool for functional NOS dimers (Peng et al., 2012).

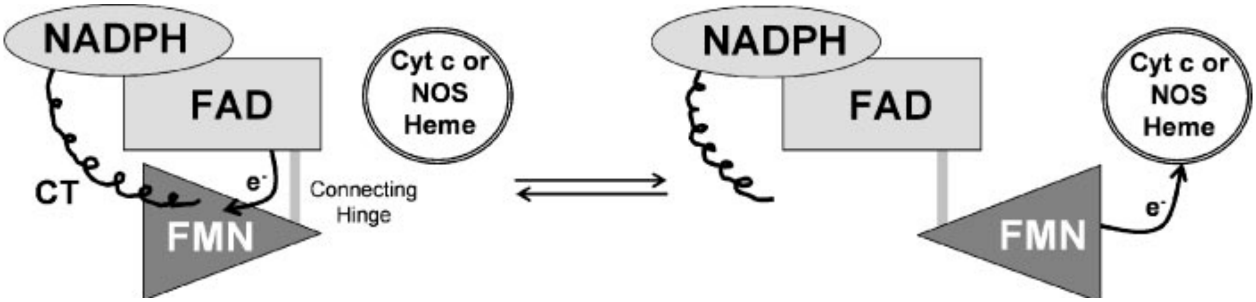

Figure 1-8 FMN release required for catalysis The flavin core of NOS and p450 is regulated by a deshielding mechanism. The cycle of FMN release is required for function and in NOS FM deshielding is regulated by CaM (Panda et al., 2006).

A full-length NOS structure had not been determined and makes understanding the wealth of kinetic, biochemical and structural information in the context of full-length NOS difficult. This missing information is likely due to the size of the NOS (~320 kDa per dimer) and the large degree of flexibility around the CaM binding helix (Figure 1-7). During my thesis work I sought to determine a full-length structure of NOS to better understand the overall conformational changes necessary for electron transfer.

1.4 Characterization of HSP100s

Structure determination of chaperones

As stated earlier, the HSP network is a vast protein network and contains a variety of chaperone proteins. For instance, small HSPs function as holdases, serving to sequester proteins during cell stress conditions to prevent aggregation formation. HSP100s function as unfoldases and disaggregases to pull apart formed protein aggregates and are constitutively expressed. Conformational changes are likely present throughout the HSP network but structural models have not yet been determined for all HSPs. Likely this lack of structural characterization is due to the fact that client-chaperone complexes form weak transient interactions as well as sample a variety of conformational changes. Tackling these challenges, structural targets will considerably advance our understanding of the HSP network.

Function of Hsp100 family

Of particular interest to my thesis research is the HSP100 family. HSP100 chaperones share a conserved ATPases Associated with diverse cellular Activities (AAA+) domain and function to protect against cellular stress and solubilize aggregates. These vital chaperones have proven challenging like many other HSPs and lack high-resolution information, making the interpretation of biochemical data more difficult. Hsp70/40 recruit HSP100s to target substrates and regulate disaggregation through a mechanism that is not fully understood. Two main branches of the Hsp100 family have been identified; unfoldases and disaggregases (Mogk et al., 2008; Saibil, 2013). An unfoldase, such as bacterial ClpA and ClpX, work in tandem with a proteolytic component, ClpP, to degrade toxic protein aggregates (Baker and Sauer, 2012; Gottesman et al., 1998). This mechanism is similar to the proteasome, in which proteins are degraded upon ubiquitin signaling (Olivares et al., 2015). Unlike the ubiquitin-proteasome system, these unfoldases have no signaling marker and rely on DnaK (bacterial homolog of Hsp70) for recruitment to target aggregates (Gottesman et al., 1998). Unfoldases contain one or two AAA+ rings, which form a hexameric oligomer complex containing a central channel and can sit atop the hexameric ClpP structure. Unfoldases feed polypeptide chains into the proteolytic channel of ClpP for degradation (Figure 1-9, top).

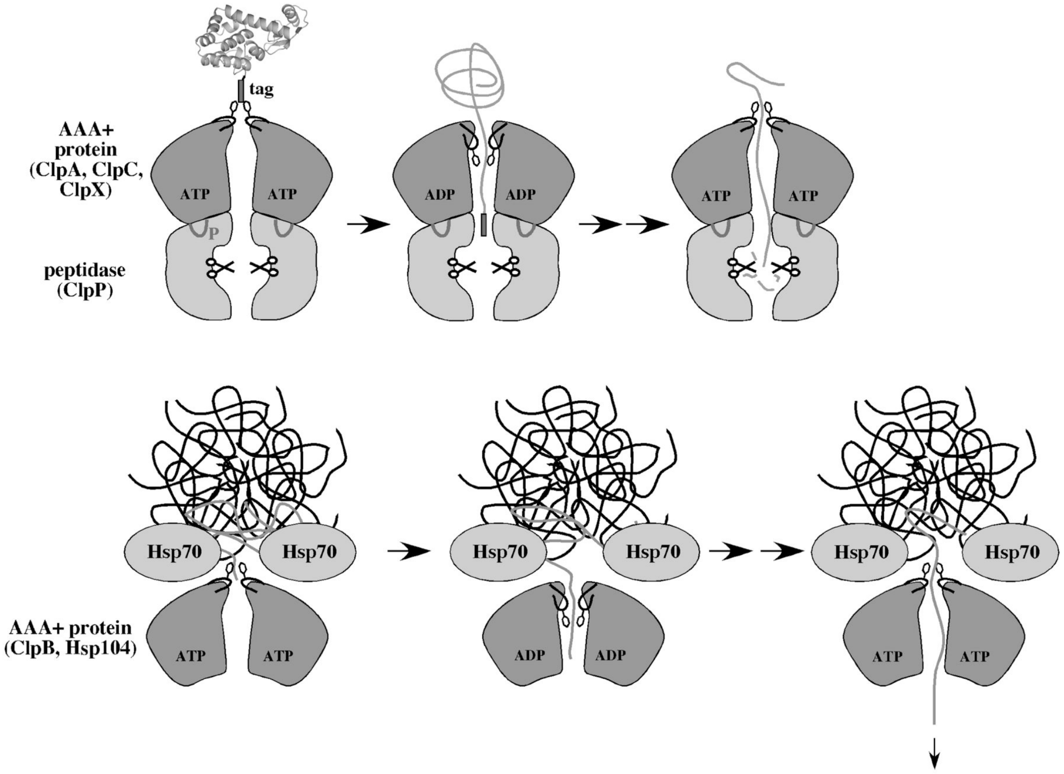

Figure 1-9 Functions of HSP100s in protein quality control (top) Unfoldases and proteolytic component interact to degrade toxic or misfolded proteins. (bottom) Disaggregases function without ClpP and hand unfolded proteins off to be refolded (Mogk et al., 2008)

HSP100 disaggregases are responsible for removing single unfolded polypeptide chains from larger aggregates. Disaggregases have two unique AAA+ domains, termed nucleotide binding domain 1 and 2 (NBD1 and NBD2) and function independently from a proteolytic component (Figure 1-9, bottom). Instead disaggregases hand unfolded proteins to downstream chaperone machinery such as Hsp70 for refolding. Bacterial ClpB, yeast Hsp104 and mitochondrial Hsp78 are all part of this HSP100 subfamily (Doyle and Wickner, 2009). All of these homologs have conserved AAA+ domains but there are critical regulatory differences within each protein. For example, Hsp78 lacks a full N-terminal domain, which is important for substrate recognition in ClpB and Hsp104 (Figure 1-10). However, even after extensive investigation of substrate recognition, hydrolysis cycle and structural motifs, the mechanism of polypeptide unfolding has remained a mystery. A lack of structural information of the full hexameric complex has limited our understanding of how HSP100s engage substrate, how translocation is regulated around the hexamer and how the energy from ATP hydrolysis is converted into mechanical force. Crystallization has been attempted to obtain the high resolution information which would answer these critical questions, but has yielded only a limited number of full length monomeric structures (Heuck et al., 2016; Lee et al., 2003, 2007). This is likely due to flexibility within the HSP100 hexamer and regulatory domains, size of the complex (~600kDa) and tendency to form helical crystal lattices.

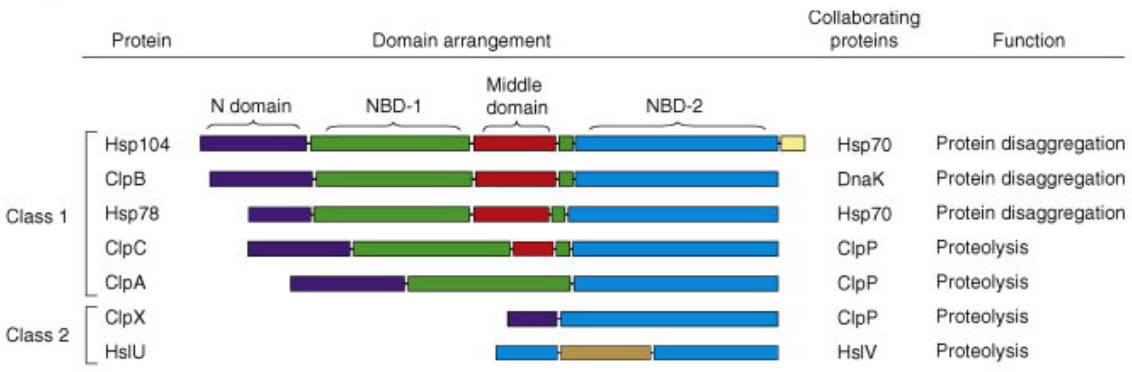

Figure 1-10 Domain alignment of HSP100s Domain alignment and function of HSP100 proteins. Class 1 spans both unfoldase and disaggregases. Class two is comprised of only unfoldases. Both classes are listed with function and collaborating chaperones (Doyle and Wickner, 2009).

AAA+ core of HSP100s

As stated HSP100s contain two AAA+ domains but how these domains convey disaggregase function is unknown. AAA+ proteins are part of a widely conserved protein family which encompasses both molecular chaperones (Hsp100s, Rvb1/2), DNA helicases (E1, MCM) and many more functions (Figure 1-11) (Ogura and Wilkinson, 2001; Snider et al., 2008). Many AAA+ domains use the energy stored within ATP to translocate substrate through a central channel similar to HSP100s. However, it is known that the translocation mechanism can accommodate a variety of substrates. Conserved pore loops form critical contacts between AAA+ and substrate that are required for translocation. The exact position of these contacts is unknown for many AAA+ domains. Pore loops contain conserved Tyr and Phe, which are critical for substrate binding. Not all AAA+ domains translocate, for example in cellular trafficking by the AAA+ machine, dynein (Cianfrocco et al., 2015; Schmidt et al., 2012). Dynein uses ATP hydrolysis to induce conformational changes which transport cargo around the cell. The importance of ATPase activity has led to many mechanistic studies of AAA+ domains. These studies have revealed a complicated ATP hydrolysis cycle which can be unique for each AAA+ complex. Additionally, structural studies of single ring AAA+ proteins have been successful in using x-ray crystallography to solve hexamer structures. Both the complex ATPase activity and difficulty of structure determination increases in the context of double AAA+ ring systems such as HSP100s. Structural studies of the larger and more dynamic two ring AAA+ proteins has yielded few structures (Blok et al., 2015; Huang et al., 2016; Ripstein et al., 2017; Zhao et al., 2015).

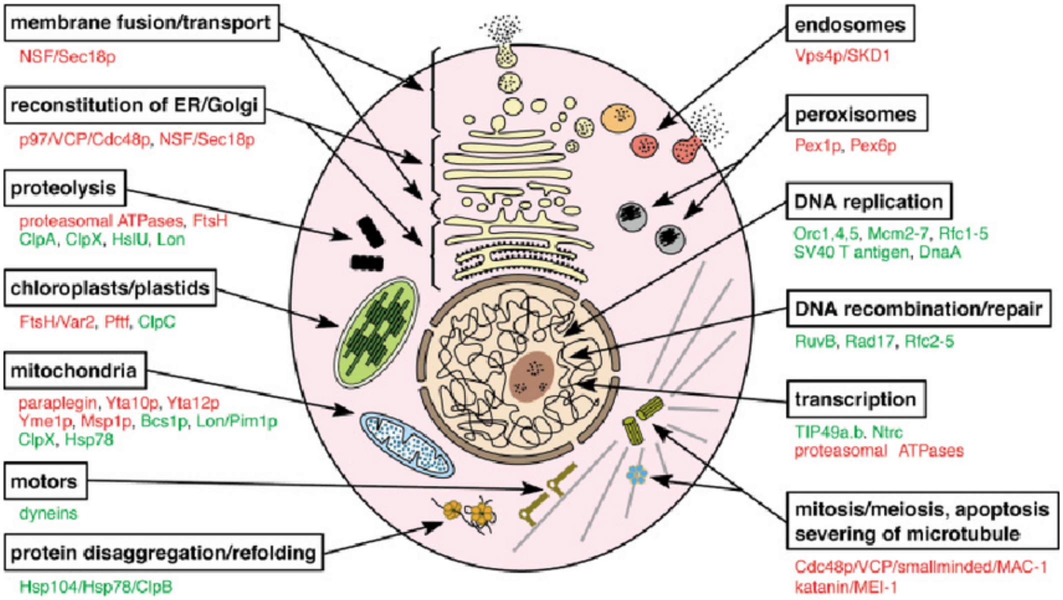

Figure 1-11 Diverse AAA+ domain functions Diagram of the vast functions performed by AAA+ proteins and their location within the cell (Ogura and Wilkinson, 2001).

AAA+ domain structural homology

AAA+ domains contain a signature α/β motif which forms two subdomains, termed large and small (Schmidt et al., 2012). Together these subdomains form the ATP binding pocket and the conserved core of all AAA+ structural motifs (Figure 1-12). The γ-phosphate of ATP is positioned for hydrolysis by canonical walker A/B and sensor residues (Miller and Enemark, 2016). Additionally, a trans activating arginine finger from the neighboring AAA+ domain supports the ATP binding pocket and is required for catalysis. The hexameric arrangement of AAA+ complexes ensure each pocket is supported for ATPase activity. AAA+ function is highly adaptable and can be augmented with additional regulatory domains. Often at the N-terminus of AAA+ domains there is a substrate recognition domain which confers specificity of AAA+ machines. Also, adaptable protein interaction domains can be found inserted at the C-terminal of the AAA+ domains. Further domain insertions occur within the AAA+ large and small subdomains and can convey a variety of functional effects. The ability to add additional regulatory domains without disrupting the overall function of the ATPase binding pocket allows for fine tuning of the AAA+ interaction network.

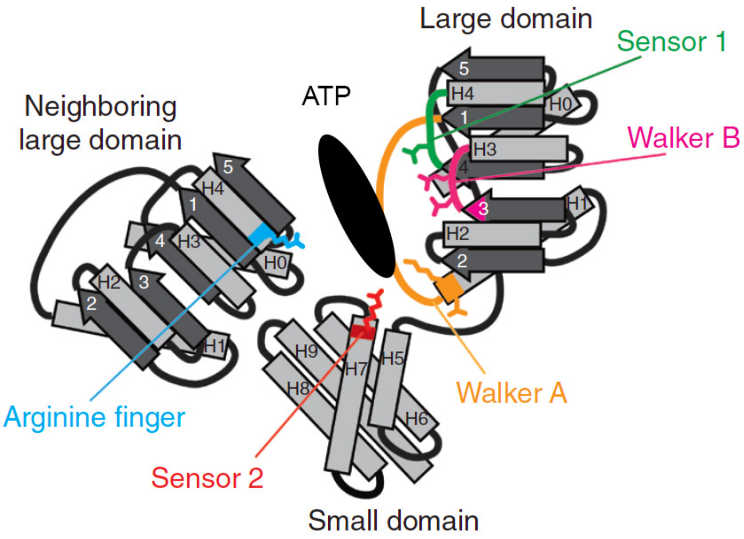

Figure 1-12 Structure of AAA+ binding pockets AAA+ binding pocket shows critical residues (sensor1,2 and walker A/B) present on the cis AAA+ domain. The catalytic Arg finger is on the trans monomer adjacent the ATP binding pocket (Schmidt et al., 2012).

AAA+ ATPase activity

The ATPase activity of the AAA+ domains remains a longstanding question for the AAA+ field. Even after decades worth of studies, the regulation and coordination of ATP hydrolysis activity within AAA+ hexamers remains highly debated. Models range from stochastic ATPase activity where monomers fire without any coordination to a highly coordinated firing of nucleotide pockets which can fire sequentially or non-sequentially (Martin et al., 2008; Sen et al., 2013). Furthermore, AAA+ complexes have varying extent of ATP turnover. For example, DNA clamp loaders hydrolyze one ATP molecule whereas ClpA is a highly active enzyme which turns over ATP rapidly (Miller and Lucius, 2014). Pore loops, within each AAA+ domain, are also thought to allosterically trigger ATP hydrolysis via an unknown mechanism. ATPase activity changes regulate the diverse function of AAA+ proteins but full mechanistic understanding is still lacking.

1.4 Yeast Hsp104 function and structural insights

Hsp104 thermotolerance in yeast

Yeast historically has served as a great model system for HSP chaperone networks (Verghese et al., 2012) due to the high conservation with human chaperones and the relative simplicity of the yeast genome. However, a eukaryotic HSP100, Hsp104 was discovered to be critical for the protein stress response and is lost through evolution, not found in in higher eukaryotes (Sanchez et al., 1992). The deletion of Hsp104 greatly reduces the survival of yeast and results in an increase in the amount of protein aggregates. Hsp104s protective effect is seen during thermal and oxidative stress but is not required for protection against cadmium or copper (Sanchez et al., 1992). Additionally, Hsp104 plays a critical role in prion inheritance helping to carry non-genomic traits from mother to daughter cells during fission (Shorter and Lindquist, 2006). This process is thought to happen though fragmentation of larger prions into intermediate species, which are more efficient at transfer, into the daughter cells. Hsp104 functions in many aspects of the yeast proteostasis network and is highly regulated by Hsp70/40 (Figure 1-13). Hsp70 regulation serves to direct Hsp104 to client aggregates however, a structure of the Hsp104 and Hsp70 complex has not been determined.

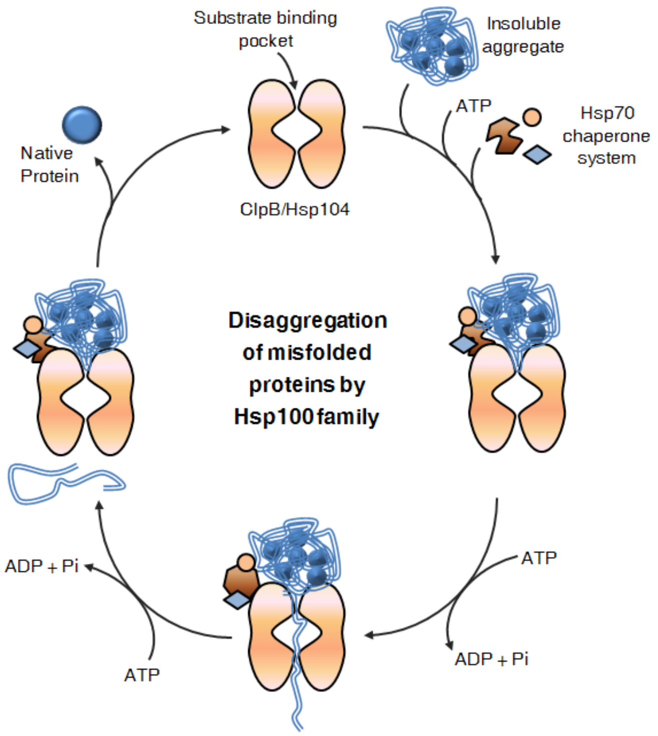

Figure 1-13 Hsp104 substrate binding cycle Hsp104 cycles through substrate free and bound states similar to other chaperones. Hsp70 coordinates Hsp104 targeting to insoluble aggregates and ATP hydrolysis is coupled with substrate translocation and unfolding (Adapted from HSPIR website).

Hsp104 as a protein therapeutic

Work from the Lindquist and Shorter labs has shown that the Hsp104 disaggregase function works on human amyloid proteins (DeSantis et al., 2012; Shorter and Lindquist, 2006). The ability to interact with human amyloids has placed great interest on the possibility of designing a protein therapeutic for neurodegenerative disease. A large number of point mutations have been shown to hyperactivate Hsp104 function (Jackrel and Shorter, 2014). These potentiated mutants greatly increase Hsp104s ability to disaggregate amyloids such as FUS and alpha-synuclein (DeSantis et al., 2012; Shorter and Lindquist, 2006). Additionally, these mutations remove the need for recruitment by Hsp70/40 allowing Hsp104 to function independently. Most of the mutations are focused on the middle domain of Hsp104, which serves as a vital regulator domain (Figure 1-14). Mutations are spread through the domain and may disrupt other interactions within the Hsp104 hexamer. However, the middle domain has not been resolved in current hexameric models for Hsp104 and understanding how these mutations confer potentiated function is not understood. Having more mechanistic information about these critical mutations will vastly improve the possibility of Hsp104 as a therapeutic.

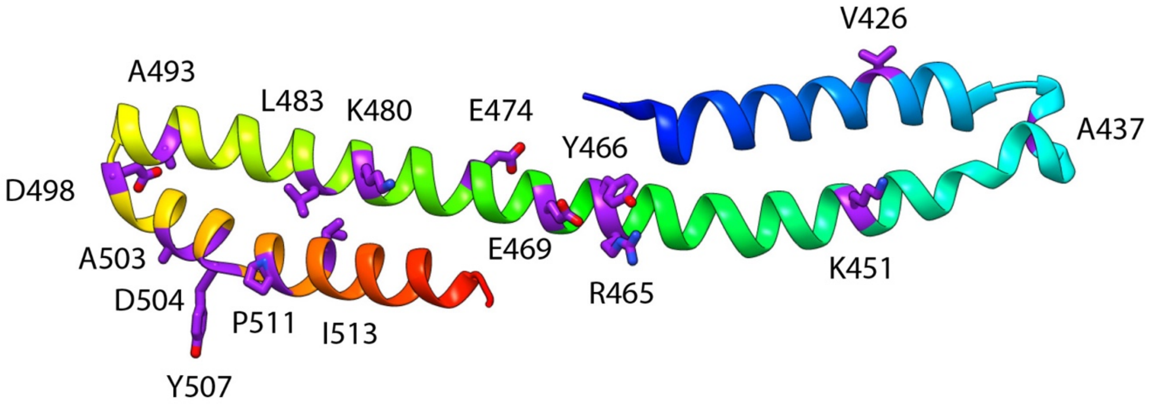

Figure 1-14 Hyperactive mutations within the MD of Hsp104 Hsp104 coiled-coil MD is colored by sequence and known hyperactive mutations are shown in purple with sidechains

1.5 References

Adak, S., Aulak, K.S., Stuehr, D.J., 2001. Chimeras of nitric-oxide synthase types I and III establish fundamental correlates between heme reduction, heme-NO complex formation, and catalytic activity. J. Biol. Chem. 276, 23246–23252. doi:10.1074/jbc.M102509200

Baker, T.A., Sauer, R.T., 2012. ClpXP, an ATP-powered unfolding and protein-degradation machine. Biochim. Biophys. Acta BBA - Mol. Cell Res., AAA ATPases: structure and function 1823, 15–28. doi:10.1016/j.bbamcr.2011.06.007

Blok, N.B., Tan, D., Wang, R.Y.-R., Penczek, P.A., Baker, D., DiMaio, F., Rapoport, T.A., Walz, T., 2015. Unique double-ring structure of the peroxisomal Pex1/Pex6 ATPase complex revealed by cryo-electron microscopy. Proc. Natl. Acad. Sci. 112, E4017–E4025. doi:10.1073/pnas.1500257112

Chen, Y., Panda, K., Stuehr, D.J., 2002. Control of nitric oxide synthase dimer assembly by a heme-NO-dependent mechanism. Biochemistry (Mosc.) 41, 4618–4625.

Cianfrocco, M.A., DeSantis, M.E., Leschziner, A.E., Reck-Peterson, S.L., 2015. Mechanism and regulation of cytoplasmic dynein. Annu. Rev. Cell Dev. Biol. 31, 83–108. doi:10.1146/annurev-cellbio-100814-125438

Correia, M.A., Sinclair, P.R., De Matteis, F., 2011. CYTOCHROME P450 REGULATION: THE INTERPLAY BETWEEN ITS HEME AND APOPROTEIN MOIETIES IN SYNTHESIS, ASSEMBLY, REPAIR AND DISPOSAL. Drug Metab. Rev. 43, 1–26. doi:10.3109/03602532.2010.515222

DeSantis, M.E., Leung, E.H., Sweeny, E.A., Jackrel, M.E., Cushman-Nick, M., Neuhaus-Follini, A., Vashist, S., Sochor, M.A., Knight, M.N., Shorter, J., 2012. Operational Plasticity Enables Hsp104 to Disaggregate Diverse Amyloid and Nonamyloid Clients. Cell 151, 778–793. doi:10.1016/j.cell.2012.09.038

Doyle, S.M., Wickner, S., 2009. Hsp104 and ClpB: protein disaggregating machines. Trends Biochem. Sci. 34, 40–48. doi:10.1016/j.tibs.2008.09.010

Feng, C., Tollin, G., 2009. Regulation of interdomain electron transfer in the NOS output state for NO production. Dalton Trans. Camb. Engl. 2003 6692–6700. doi:10.1039/b902884f

Förstermann, U., Sessa, W.C., 2012. Nitric oxide synthases: regulation and function. Eur. Heart J. 33, 829–837, 837a–837d. doi:10.1093/eurheartj/ehr304

Gottesman, S., Roche, E., Zhou, Y., Sauer, R.T., 1998. The ClpXP and ClpAP proteases degrade proteins with carboxy-terminal peptide tails added by the SsrA-tagging system. Genes Dev. 12, 1338–1347.

Grant, B.J., Gorfe, A.A., McCammon, J.A., 2010. Large conformational changes in proteins: signaling and other functions. Curr. Opin. Struct. Biol. 20, 142–147. doi:10.1016/j.sbi.2009.12.004

Gutteridge, A., Thornton, J., 2004. Conformational change in substrate binding, catalysis and product release: an open and shut case? FEBS Lett. 567, 67–73. doi:10.1016/j.febslet.2004.03.067

Hartl, F.U., Bracher, A., Hayer-Hartl, M., 2011. Molecular chaperones in protein folding and proteostasis. Nature 475, 324–332. doi:10.1038/nature10317

Henzler-Wildman, K., Kern, D., 2007. Dynamic personalities of proteins. Nature 450, 964–972. doi:10.1038/nature06522

Hessling, M., Richter, K., Buchner, J., 2009. Dissection of the ATP-induced conformational cycle of the molecular chaperone Hsp90. Nat. Struct. Mol. Biol. 16, 287–293. doi:10.1038/nsmb.1565

Heuck, A., Schitter-Sollner, S., Suskiewicz, M.J., Kurzbauer, R., Kley, J., Schleiffer, A., Rombaut, P., Herzog, F., Clausen, T., 2016. Structural basis for the disaggregase activity and regulation of Hsp104. eLife 5. doi:10.7554/eLife.21516

Huang, R., Ripstein, Z.A., Augustyniak, R., Lazniewski, M., Ginalski, K., Kay, L.E., Rubinstein, J.L., 2016. Unfolding the mechanism of the AAA+ unfoldase VAT by a combined cryo-EM, solution NMR study. Proc. Natl. Acad. Sci. U. S. A. 113, E4190-4199. doi:10.1073/pnas.1603980113

Jackrel, M.E., Shorter, J., 2014. Potentiated Hsp104 variants suppress toxicity of diverse neurodegenerative disease-linked proteins. Dis. Model. Mech. 7, 1175–1184. doi:10.1242/dmm.016113

Jeng, W., Lee, S., Sung, N., Lee, J., Tsai, F.T.F., 2015. Molecular chaperones: guardians of the proteome in normal and disease states. F1000Research 4. doi:10.12688/f1000research.7214.1

Krivoruchko, A., Storey, K.B., 2010. Forever Young: Mechanisms of Natural Anoxia Tolerance and Potential Links to Longevity. Oxid. Med. Cell. Longev. 3, 186–198. doi:10.4161/oxim.3.3.12356

Lee, S., Choi, J.-M., Tsai, F.T.F., 2007. Visualizing the ATPase Cycle in a Protein Disaggregating Machine: Structural Basis for Substrate Binding by ClpB. Mol. Cell 25, 261–271. doi:10.1016/j.molcel.2007.01.002

Lee, S., Sowa, M.E., Watanabe, Y., Sigler, P.B., Chiu, W., Yoshida, M., Tsai, F.T.F., 2003. The structure of ClpB: a molecular chaperone that rescues proteins from an aggregated state. Cell 115, 229–240.

Li, J., Buchner, J., 2013. Structure, function and regulation of the hsp90 machinery. Biomed. J. 36, 106–117. doi:10.4103/2319-4170.113230

Liu, X.-D., 1997. Conservation of a stress response: human heat shock transcription factors functionally substitute for yeast HSF. EMBO J. 16, 6466–6477. doi:10.1093/emboj/16.21.6466

Luo, W., Zhong, J., Chang, R., Hu, H., Pandey, A., Semenza, G.L., 2010. Hsp70 and CHIP Selectively Mediate Ubiquitination and Degradation of Hypoxia-inducible Factor (HIF)-1α but Not HIF-2α. J. Biol. Chem. 285, 3651–3663. doi:10.1074/jbc.M109.068577

Marletta, M.A., 1994. Nitric oxide synthase: aspects concerning structure and catalysis. Cell 78, 927–930.

Martin, A., Baker, T.A., Sauer, R.T., 2008. Protein unfolding by a AAA+ protease is dependent on ATP-hydrolysis rates and substrate energy landscapes. Nat. Struct. Mol. Biol. 15, 139–145. doi:10.1038/nsmb.1380

Miller, J.M., Enemark, E.J., 2016. Fundamental Characteristics of AAA+ Protein Family Structure and Function. Archaea 2016. doi:10.1155/2016/9294307

Miller, J.M., Lucius, A.L., 2014. ATPγS competes with ATP for binding at Domain 1 but not Domain 2 during ClpA catalyzed polypeptide translocation. Biophys. Chem. 185, 58–69. doi:10.1016/j.bpc.2013.11.002

Mogk, A., Haslberger, T., Tessarz, P., Bukau, B., 2008. Common and specific mechanisms of AAA+ proteins involved in protein quality control. Biochem. Soc. Trans. 36, 120–125. doi:10.1042/BST0360120

Munro, A.W., Leys, D.G., McLean, K.J., Marshall, K.R., Ost, T.W.B., Daff, S., Miles, C.S., Chapman, S.K., Lysek, D.A., Moser, C.C., Page, C.C., Dutton, P.L., 2002. P450 BM3: the very model of a modern flavocytochrome. Trends Biochem. Sci. 27, 250–257.

Nishida, N., Osawa, M., Takeuchi, K., Imai, S., Stampoulis, P., Kofuku, Y., Ueda, T., Shimada, I., 2014. Functional dynamics of cell surface membrane proteins. J. Magn. Reson. San Diego Calif 1997 241, 86–96. doi:10.1016/j.jmr.2013.11.007

Ogura, T., Wilkinson, A.J., 2001. AAA+ superfamily ATPases: common structure--diverse function. Genes Cells Devoted Mol. Cell. Mech. 6, 575–597.

Olivares, A.O., Baker, T.A., Sauer, R.T., 2015. Mechanistic insights into bacterial AAA+ proteases and protein-remodelling machines. Nat. Rev. Microbiol. 14, 33–44. doi:10.1038/nrmicro.2015.4

Panda, K., Haque, M.M., Garcin-Hosfield, E.D., Durra, D., Getzoff, E.D., Stuehr, D.J., 2006. Surface Charge Interactions of the FMN Module Govern Catalysis by Nitric-oxide Synthase. J. Biol. Chem. 281, 36819–36827. doi:10.1074/jbc.M606129200

Park, C.S., Krishna, G., Ahn, M.S., Kang, J.H., Chung, W.G., Kim, D.J., Hwang, H.K., Lee, J.N., Paik, S.G., Cha, Y.N., 2000. Differential and constitutive expression of neuronal, inducible, and endothelial nitric oxide synthase mRNAs and proteins in pathologically normal human tissues. Nitric Oxide Biol. Chem. 4, 459–471. doi:10.1006/niox.2000.0300

Peng, H.-M., Morishima, Y., Pratt, W.B., Osawa, Y., 2012. Modulation of heme/substrate binding cleft of neuronal nitric-oxide synthase (nNOS) regulates binding of Hsp90 and Hsp70 proteins and nNOS ubiquitination. J. Biol. Chem. 287, 1556–1565. doi:10.1074/jbc.M111.323295

Poulos, T.L., Li, H., 2013. Structural basis for isoform-selective inhibition in nitric oxide synthase. Acc. Chem. Res. 46, 390–398. doi:10.1021/ar300175n

Pratt, W.B., Morishima, Y., Peng, H.-M., Osawa, Y., 2010. Proposal for a role of the Hsp90/Hsp70-based chaperone machinery in making triage decisions when proteins undergo oxidative and toxic damage. Exp. Biol. Med. Maywood NJ 235, 278–289. doi:10.1258/ebm.2009.009250

Proctor, C.J., Lorimer, I.A.J., 2011. Modelling the Role of the Hsp70/Hsp90 System in the Maintenance of Protein Homeostasis. PLoS ONE 6, e22038. doi:10.1371/journal.pone.0022038

Ripstein, Z.A., Huang, R., Augustyniak, R., Kay, L.E., Rubinstein, J.L., 2017. Structure of a AAA+ unfoldase in the process of unfolding substrate. eLife 6. doi:10.7554/eLife.25754

Roberts, G.A., Grogan, G., Greter, A., Flitsch, S.L., Turner, N.J., 2002. Identification of a New Class of Cytochrome P450 from a Rhodococcus sp. J. Bacteriol. 184, 3898–3908. doi:10.1128/JB.184.14.3898-3908.2002

Saibil, H., 2013. Chaperone machines for protein folding, unfolding and disaggregation. Nat. Rev. Mol. Cell Biol. 14, 630–642. doi:10.1038/nrm3658

Sanchez, Y., Taulien, J., Borkovich, K.A., Lindquist, S., 1992. Hsp104 is required for tolerance to many forms of stress. EMBO J. 11, 2357–2364.

Schmidt, H., Gleave, E.S., Carter, A.P., 2012. Insights into dynein motor domain function from a 3.3-Å crystal structure. Nat. Struct. Mol. Biol. 19, 492–497. doi:10.1038/nsmb.2272

Sen, M., Maillard, R.A., Nyquist, K., Rodriguez-Aliaga, P., Pressé, S., Martin, A., Bustamante, C., 2013. The ClpXP protease unfolds substrates using a constant rate of pulling but different gears. Cell 155, 636–646. doi:10.1016/j.cell.2013.09.022

Shorter, J., Lindquist, S., 2006. Destruction or potentiation of different prions catalyzed by similar Hsp104 remodeling activities. Mol. Cell 23, 425–438. doi:10.1016/j.molcel.2006.05.042

Smith, B.C., Underbakke, E.S., Kulp, D.W., Schief, W.R., Marletta, M.A., 2013. Nitric oxide synthase domain interfaces regulate electron transfer and calmodulin activation. Proc. Natl. Acad. Sci. U. S. A. 110, E3577-3586. doi:10.1073/pnas.1313331110

Snider, J., Thibault, G., Houry, W.A., 2008. The AAA+ superfamily of functionally diverse proteins. Genome Biol. 9, 216. doi:10.1186/gb-2008-9-4-216

Southworth, D.R., Agard, D.A., 2008. Species-dependent ensembles of conserved conformational states define the Hsp90 chaperone ATPase cycle. Mol. Cell 32, 631–640. doi:10.1016/j.molcel.2008.10.024

Stephanou, A., Latchman, D.S., 2011. Transcriptional Modulation of Heat-Shock Protein Gene Expression. Biochem. Res. Int. 2011, 1–8. doi:10.1155/2011/238601

van den Bedem, H., Fraser, J.S., 2015. Integrative, dynamic structural biology at atomic resolution--it’s about time. Nat. Methods 12, 307–318. doi:10.1038/nmeth.3324

Verghese, J., Abrams, J., Wang, Y., Morano, K.A., 2012. Biology of the heat shock response and protein chaperones: budding yeast (Saccharomyces cerevisiae) as a model system. Microbiol. Mol. Biol. Rev. MMBR 76, 115–158. doi:10.1128/MMBR.05018-11

Wayne, N., Mishra, P., Bolon, D.N., 2011. Hsp90 and client protein maturation. Methods Mol. Biol. Clifton NJ 787, 33–44. doi:10.1007/978-1-61779-295-3_3

Zhao, M., Wu, S., Zhou, Q., Vivona, S., Cipriano, D.J., Cheng, Y., Brunger, A.T., 2015. Mechanistic insights into the recycling machine of the SNARE complex. Nature 518, 61–67. doi:10.1038/nature14148

Zhuravleva, A., Gierasch, L.M., 2015. Substrate-binding domain conformational dynamics mediate Hsp70 allostery. Proc. Natl. Acad. Sci. 112, E2865–E2873. doi:10.1073/pnas.1506692112

Chapter 2 – Transmission Electron Microscopy

2.1 Abstract

Structure determination is critical to defining and interpreting the function of macromolecules. Traditionally, most structure determination is focused on using X-ray crystallography or NMR. X-ray crystallography is a high-resolution technique and protein structure determination has been immensely successful for a long time. However, the formation of a stable crystal lattice proves to be an extremely difficult process for many flexible proteins or multi protein complexes. NMR is capable of studying the conformational states of proteins and forms ensemble structures. Structure determination via NMR is exceedingly limited by the size of the protein, ~50kDa. These drawbacks make X-ray crystallography and NMR non-ideal tools for studying protein structure of large and dynamic macromolecules. Recent advancements in electron microscopy (EM) techniques and technology have spurred a 'resolution revolution' that allows for the study of macromolecule interactions along with the capability of capturing conformational changes. Furthermore, EM studies in both 2D and 3D techniques aid in the understanding of macromolecular structure and function. This chapter contains an extended description of transmission EM techniques and the recent advancements in EM technology.

2.2 Electron Microscopy

Electron microscopy overview

Transmission electron microscopy (TEM) is the main technique used in the remaining chapters, therefore a detailed description of this technique follows. TEM can be utilized in a variety of structure determination techniques such as electron tomography, micro electron diffraction and single particle EM. Focus will be placed on the single particle techniques, which were used in the following studies. TEM allows the study of highly dynamic proteins to understand overall domain architecture at lower resolutions. Additionally, single particle TEM has become a major technique for high resolution imaging of protein complexes to near atomic resolution. Negative stain and cryo EM are commonly used imaging techniques which both rely on detecting scattered electrons after they are directed through a complex arrangement of electromagnetic lenses and the specimen of interest. With an assortment of recent technological advancements such as direct electron detectors, dose filtering and advanced alignments, TEM has rapidly become a prime structural tool to answer many biological questions.

Data Collection

TEM relies on a parallel beam of electrons being emitted from a source and passed through the sample, then manipulated by electromagnetic lenses to obtain an electron micrograph. Typical electron sources are made of tungsten or lanthanum hexaboride (Broers, 1967; Erdman and Zipf, 1982). These sources emit a stream of electrons when heated but can be damaged and have low signal to noise ratios. Higher end electron emitters, named field emission guns (FEG) (Swanson and Martin, 1975), are often made of tungsten coated with zirconium dioxide. The coating of the tungsten filament increases its lifetime and brightness at high currents, improving data collection. This coating is particularly important in Schottky FEG emitters which are used in the X-FEG module of high voltage microscopes such as Thermal Fisher FEI – Titian Krios or Talos Artica (200-300 kV). Additionally, the increased precision of FEGs allow for better spatial resolution and coherency, boosting the signal-to-noise during data collection.

The electron beam is passed through condenser lenses to parallelize the electron beam before interaction with the sample of interest (Figure 2-1, left). Electrons are scattered by the sample and have varying degrees of energy based on the type of collision (Frank, 2006). Elastic and inelastic collisions occur with some electrons being absorbed or back scattered (Figure 2-1, right). The bulk of electrons remain unscattered but some are diffracted and captured. These electrons pass through objective and projector lens, which have magnetic currents to form the final electron micrograph image. Electrons are recorded on a variety of detectors such as film, charge-coupled devices (CCD) and direct electron detectors. The latter has led to a significant advancement in TEM data collection and is described in detail below.

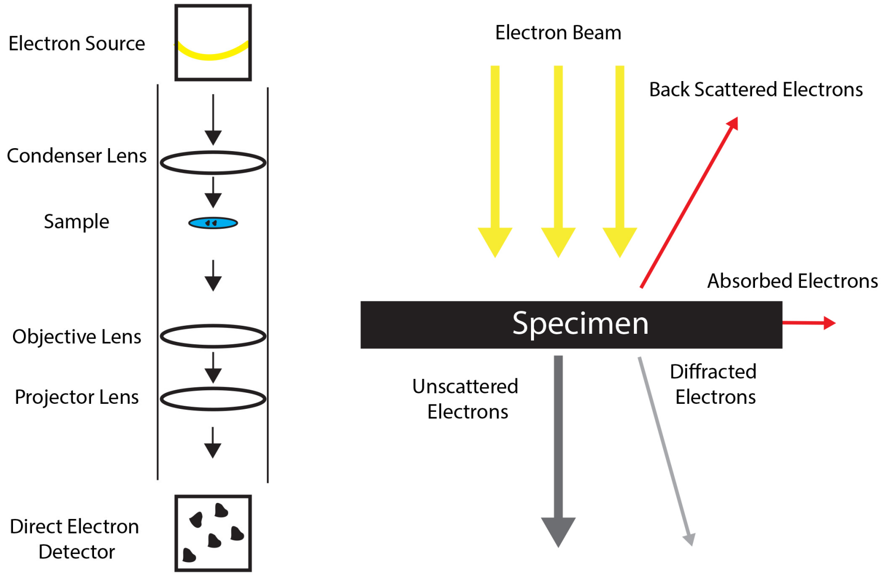

Figure 2-1 Transmission electron microscope and electron diffraction (left) Illustrator of an electron microscope column containing lens, sample and detector. (right) Collision diagram of electrons for TEM data collection.

Negative Stain Electron Microscopy

Negative stain EM (NSEM) uses heavy atom stain to generate an envelope around a sample for high contrast imaging. This technique begins with a thin carbon layer over a copper support grid. This serves as a platform for proteins and subsequent heavy atom stain, typically uranyl acetate or uranyl formate. Carbon grids are glow discharged or plasma cleaned to increase the hydrophilicity of the carbon through the bombardment of N_2 and O_2 molecules. Sample is applied and allowed to adhere to the hydrophilic surface before removing excess liquid and rinsing with H_2O, and lastly applying stain (Ohi et al., 2004). Once the stain is applied on top of the protein sample, it is dried, dehydrating biological samples and providing a stain envelope around the protein sample. This stain envelope can be imaged and the areas that contain less stain diffract fewer electrons. This produces an electron micrograph, which presents a high signal-to-noise image where the stain and protein boundaries can be identified.

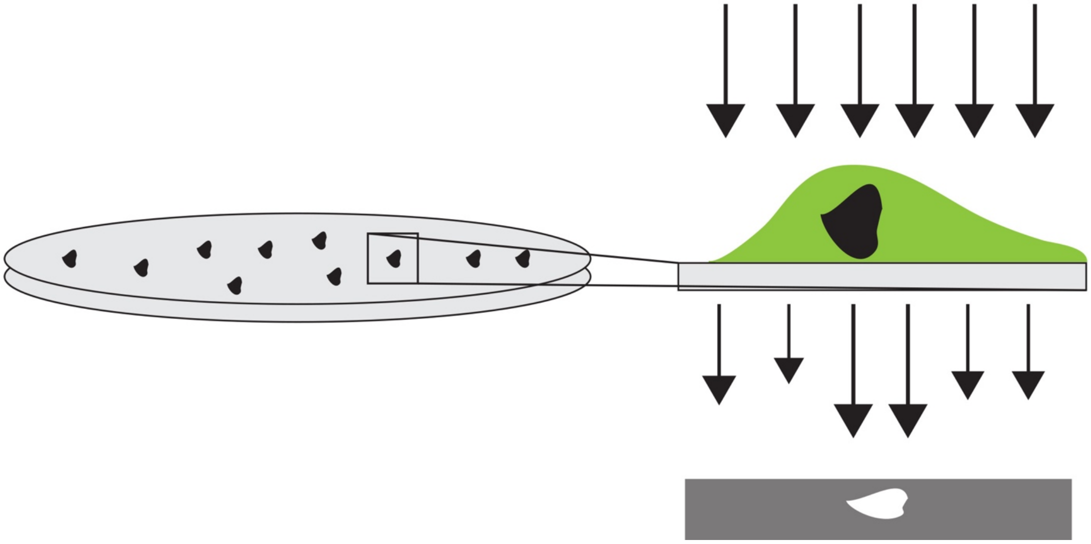

Figure 2-2 Negative stain sample preparation schematic Cartoon representative of negative stain EM samples. Protein sample is absorbed onto a carbon support and coated in heavy atom stain. Electrons are passed through the specimen and single particles are detected.

Negative stain can be limited in resolution via three major factors; protein collapse, preferred orientation and stain granule size. NSEM is centered on imaging the absence of stain within an electron dense background. Therefore, the stain envelope is limited by the size of the stain granules. Typically, stain granules are around ~15Å limiting high-resolution information (Peisley and Skiniotis, 2015). Protein collapse is a consequence of dehydrating biological samples and can partially flatten or distort structural information. Weakly binding protein interactions can also be disrupted and may fall apart during the staining process because protein must be diluted to ~100 nM (Skiniotis and Southworth, 2016). Lastly, NS samples suffer from preferred orientation of the sample. Proteins attach to the carbon surface through hydrophilic interactions and frequently align along similar orientations. This leads to a biased view of the sample and a lack of structural information for other orientations. This lack of views can greatly limit efforts for high-resolution 3D analysis but can be used in random conical and orthogonal tilt routines for initial structure determination (Leschziner and Nogales, 2006; Radermacher et al., 1987).

The limitations of NSEM have not prevented it from being a tremendously beneficial technique for structure determination, particularly when studying heterogeneous samples (Takizawa et al., 2017). In more dynamic protein complexes the high contrast images obtained from negative stain electron microscopy allow for the study of protein conformational states. Mobile domains and flexible protein complexes are significantly harder to study within low contrast cryo EM, and for this reason negative stain functions as an exceptional tool for studying dynamic systems. 2D classification and alignment are significantly easier for NS data and can be used to sort out small or flexible complexes (Peisley and Skiniotis, 2015). Additionally, NSEM is useful for initial 3D model generation and sample screening. Similarly, low-resolution models from negative stain greatly improve the reliability of cryo EM reconstructions. Starting 3D structure determination with a low-resolution model allows for more confident alignment of single particles from cryo EM. Lastly, outside of protein structure determination negative stain EM is a quick way to screen numerous conditions such as protein purifications and in vitro complex formation to better prepare samples for cryo EM studies.

Cryo Electron Microscopy

Cryo electron microscopy (cryo EM) is the preferred high-resolution imaging technique for single particle structure determination. Cryo EM maintains the specimen in a hydrated state. A small amount (2-4 μL) of protein sample is applied directly to glow discharged holey carbon grids. Manual or robotic blotting removes the bulk of the sample and leaves a thin layer of liquid suspended across the carbon hole (Figure 2-3, top) (Carroni and Saibil, 2016). The grid and sample are plunged into liquid ethane, propane or a mixture of both for rapid cooling (Umrath, 1974). Rapid cooling serves to cool a thin layer of sample to -180ºC fast enough as to not allow the arrangement of hydrogen bond networks, limiting the formation of crystalline ice. Crystalline ice greatly increases background and generates a diffraction pattern damaging any TEM information collected. The non-crystalline ice, termed vitreous ice, is an amorphous background and only weakly scatters electrons. Proteins within vitreous ice adapt random 3D orientations and when imaged, many 3D orientations can be resolved. Cryo EM images suffer from an extremely low signal-to-noise ratio, opposite of the high signal-to-noise for NSEM. Additionally, the low contrast makes assigning orientation parameters more difficult when processing data.

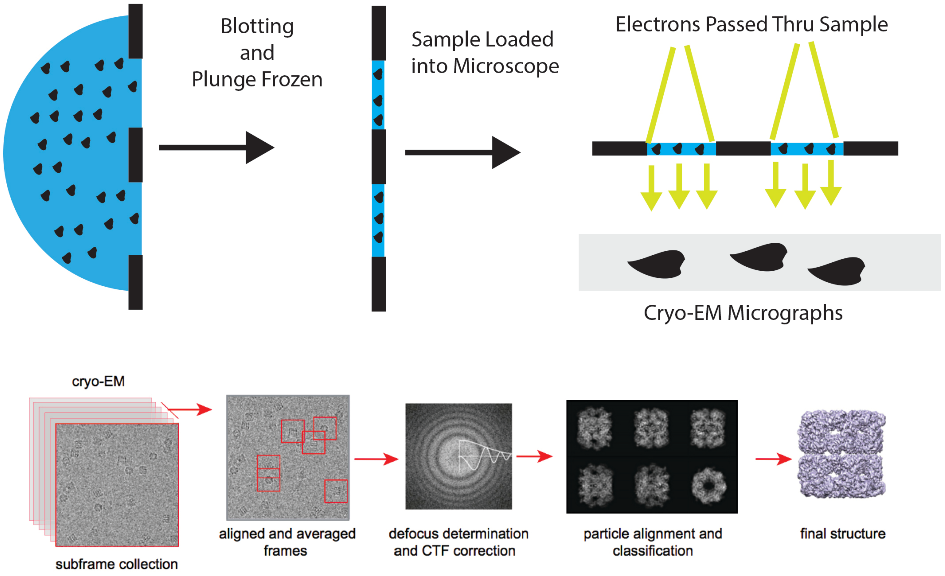

Figure 2-3 Cryo electron microscopy sample preparation and data processing (top) Aqueous sample is applied to a holey carbon grid. The bulk of the sample is removed via blotting. Frozen sample is then loaded into an electron microscopy and imaged through the vitreous ice sample. (bottom) Movie stack processing is used to boost signal to noise for integration. This micrograph is used for CTF determination and subsequent 2D and 3D analysis (Carroni and Saibil, 2016)

Cryo EM directly images protein atoms and removes the resolution limitation from stain granules seen in NSEM. Direct imaging of protein samples allows for atomic resolution information to be collected. This boost in resolution is noticeable in the thon rings within the 2D fast Fourier transform (FFT) (Figure 2-3, bottom). Frozen samples may suffer from radiation and are susceptible to electron charging effects (Baker and Rubinstein, 2010; Bammes et al., 2010). Nevertheless, recent technological advancements have made for reconstructions at near atomic resolution (~3Å) and as the electron microscopy field continues to expand more structures will be determined. The technical aspects of cryo EM the advancement of improved detectors, data collection methods and improving image formation algorithms have greatly improved the structural determination process of cryo EM and are detailed below.

Single particle Analysis

Single particle EM is a method of 3D structure determination using TEM in both negative stain and cryo EM techniques. 2D micrographs are collected which contain isolated macromolecules in different views. From these images, individual particles are selected regularly through automated selection software. The automated particle selection software packages include Relion, Appion and EMAN2 and use a variety of filtering or binning steps to detect a change in signal, with the idea that the signal change corresponds to a single particle (Lander et al., 2009; Scheres, 2012; Tang et al., 2007). Utilizing automated particle picking can greatly decrease the amount of time for single particle selection. However, this type of picking can contain ‘junk’ particles. Junk particles can be crystalline ice contamination, protein aggregates or the carbon edge of the hole. Luckily, 2D classification can be used to remove these erroneously selected particles.

After single particle selection, the initial processing of EM data is 2D classification. Single particles are compared to each other and based on K-means clustering are grouped into 2D class averages (Jung et al., 2014). This analysis requires no previous structural information. Furthermore, 2D classification has the capacity to sort out different conformations within a protein sample before any 3D information is determined (Peisley and Skiniotis, 2015). Recent advancement in 2D classification have led to new 2D classification methods, such as iterative stable alignment and clustering (ISAC) which validates 2D class averages each iteration and removes junk or unstable averages from the final classification (Yang et al., 2012). 2D class averages serve as a checkpoint for single particles before 3D structural determination and can greatly inform on the homogeneity and quality of a sample.

3D classification techniques, which generate multiple 3D reconstructions for a single set of particles, are proving to be a key component of capturing conformational changes. This routine uses maximum likelihood approaches (Sigworth et al., 2010), implemented by RELION and FREALIGN (Grigorieff, 2007; Scheres, 2012) to assign a probability factor for a single particle matching all of the reconstructions being iteratively refined. Initial comparison of the single particle with each model begins with a coarse angular sample (15º). This sampling is adjusted based on resolution of each model until only local adjustments (1-3º) are made. 3D classification is conventionally limited by the need for an initial model. Having a low resolution model from NSEM, previous studies or generating a sphere of density all work, but often the wrong initial model can hamper the ability for 3D classification methods to obtain the correct structural solutions. Luckily, software packages are emerging which are well suited in generating *ab initio* models from 2D class averages such as VIPER, IMAGIC and cryoSPARC software packages (Hohn et al., 2007; Punjani et al., 2017; Van Heel, 1987). These packages rely on traditional ‘common lines’ approaches to combine class average information into initial low-resolution 3D models. Additional data collection techniques such as random conical and orthogonal tilt can generate initial reconstructions (Leschziner and Nogales, 2006; Radermacher et al., 1987). Final 3D reconstructions are subjected to iterative rounds of gold standard processing (Penczek, 2010; Scheres and Chen, 2012). The particle data set is split into two halves and the orientation parameters are refined. From the two half maps a final reconstruction is generated and compared using a Fourier shell correlation

(FSC) to validate the reconstruction and ensure convergence (van Heel and Schatz, 2005).

Random conical tilt reconstruction

Random conical tilt (RCT) is a method for EM model determination that utilizes both untilted (0º) and tilted micrographs (30-60º) (Radermacher et al., 1987). This minimizes the impact of preferred orientation on the carbon surface and is advantageous for heterogeneous samples. Identical single particles are selected from both micrographs and the untilted data are processed normally. From these 2D class averages the orientation parameters of the titled data can be resolved. The tilted particles create a cone of single particle information. This cone of structural information can be used to accurately position the tilted particles and generate a 3D reconstruction from particle back projections. Using RCT, heterogeneous samples can be solved as independent classes and models can be generated for each conformation. Lower resolution is obtained but this can still add valuable structural insights. Additionally, this method does not require an initial 3D model and relies solely on the reference free class averages. Lastly, generation of low-resolution models can prove to be a critical step towards high-resolution structure determination, specifically in cryo EM which suffers from low signal to noise.

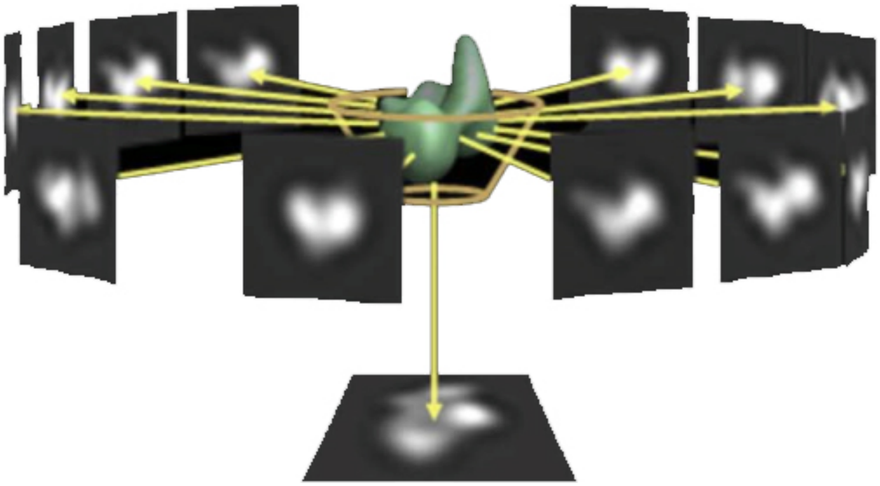

Figure 2-4 Random conical tilt 3D reconstruction schematic Untilted 2D data is used to generate orientation parameters of tilted data allowing for the creation of initial 3D reconstructions (Leschziner and Nogales, 2006)

Analysis of electron microscopy maps

The amount of structural information acquired from TEM is highly dependent on the final resolution of the 3D reconstruction. Most EM maps have a large range of anisotropic resolution changes, where flexible domains are blurred and show lower resolution and the core of complexes is resolved to higher resolution. This makes modeling challenging and multiple approaches can be needed to properly determine a structural model. Also, EM maps can cover a range of resolutions (2-40Å) much larger than other structural techniques making over interpretation a major concern. Maps on the lower end, between 15-40Å require previous structural information to model. Low resolution modeling is accomplished by rigid body docking of previous structural models such as the *fit_in_map* function within the Chimera software package. Frequently these models come from x-ray crystallography or NMR studies which solved portions of the full specimen or a homologous protein. Moderate resolution ranges 10-14Å all for the rearrangement of secondary structural motifs. Alpha helices can be moved thru real space refinement tools such as phenix.real_space_refine and others (Afonine et al., 2012). These tools maintain the known structural information but allow for adjustment of flexible loop regions. Sub-nano resolutions, 6-10Å, allow for polypeptide backbone atoms to be modeled. This is particularly true in the core of such 3D reconstructions which when tuned to the correct viewing threshold should show proper alpha helical handedness and contours.

The aim of structure determination is to achieve near atomic resolution maps, 3-5Å, should show bulky side chain residues and bound ligands. Modeling parameters should still be heavily biased towards known geometric constraints. The use of previously established modeling tools such as COOT or PHENIX are now applicable as well (Afonine et al., 2012; Emsley et al., 2010). However, *de novo* modeling of near atomic maps is still challenging and homology models serve as remarkably good starting points for structure determination. High resolution maps, <3Å, can be built *de novo*, occasionally, and modeling of side chain rotamers can be used (Song et al., 2013). Throughout all resolution ranges appropriate validation steps should be taken such as Molprobity and domain clash scores (Chen et al., 2010). Additionally, local resolution measurements are frequently taken using Resmap to display the range of resolutions within a EM map (Kucukelbir et al., 2013).

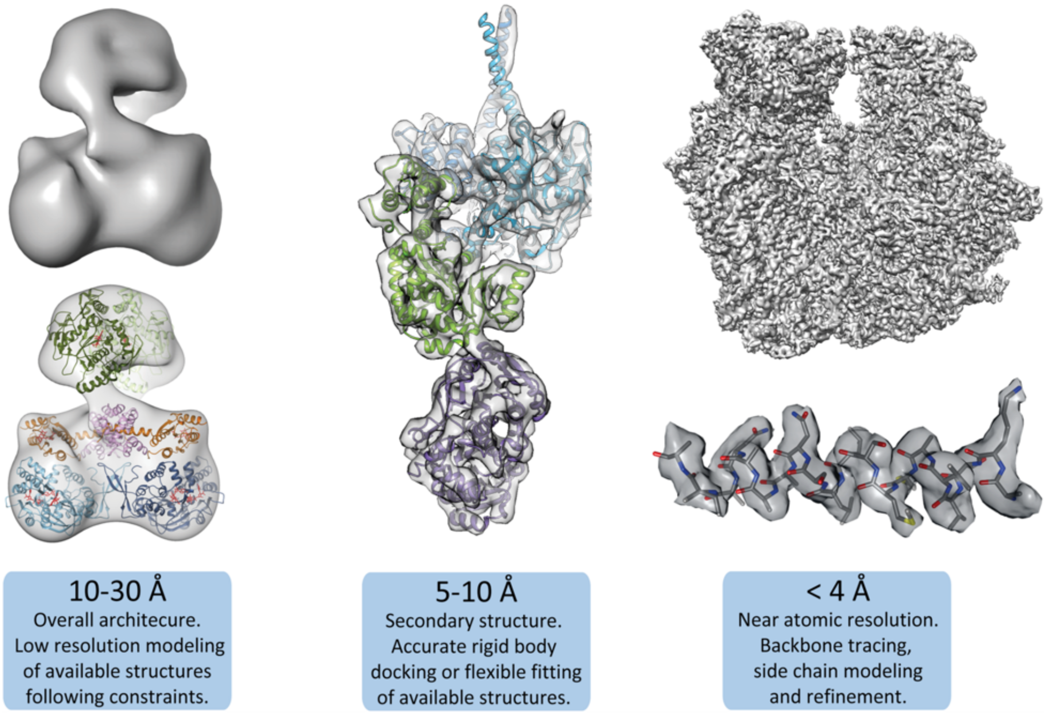

Figure 2-5 Range of TEM map resolutions and features observed Taken from Skiniotis and Southworth, 2016.

2.2 Recent Advancements of TEM technology

Direct Electron Detectors

Direct electron detectors (DED) allow for frame-by-frame data collection (<10msec/frame) and individual counting of electrons. One of the undesirable aspects of TEM is beam-induced motion. Motion can be induced by the electron beam used to image proteins samples and has long been a limiting factor in resolution of TEM reconstructions. This motion can manifest in X, Y, and Z direction and blurs the images, distorting high-resolution information. Frame by frame data collection allows for correction of the X and Y motion through drift correction software (Li et al., 2013; Scheres, 2014). The movie stack generated for a single electron micrograph can be processed before integration of the data into the final micrograph used for single particle selection. Individual frames which have drifted in the X and Y direction can be aligned using a cross correlation analysis. By correcting this drift, the contrast of electron micrographs increases, high-resolution information is restored and 3D structure determination is significantly improved. Additionally, the majority of beam-induced drift occurs during the initial imaging frames. These frames contain the least amount of radiation damage but can be removed during pre-processing steps to improve the accuracy of drift correction.

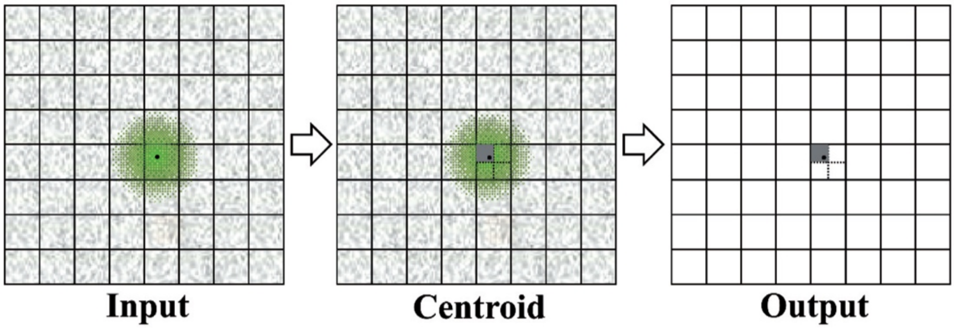

Figure 2-6 Counted mode direct electron detectors Centroid of electrons impact is tracked isolating the electron location to a quadrant of a pixel greatly improving electron accuracy (Xueming, 2016).

Another facet of DEDs improvement of EM, is the ability to accurately count individual electrons (Xueming, 2016). Previous electron detection methods for CCDs used error prone scintillation counters to indirectly collect electron scattering data. DEDs have removed this requirement and use an array of silicon circuits for detection. This large array of pixels determines the centroid of each electron and localizes this information to a single quadrant, resulting in accurate tracking of electron scattering data. This accuracy allows for the deconvolution of individual electron reads. DEDs also have a boosted detective quantum efficiency (DQE), which measures the amount of captured and usable data throughout a range of resolutions. Particularly a boost in DQE near Nyquist is important for high resolution information (McMullan et al., 2014). By increasing this range, data can be collected at lower dose rates (further improving accuracy of electron localization).

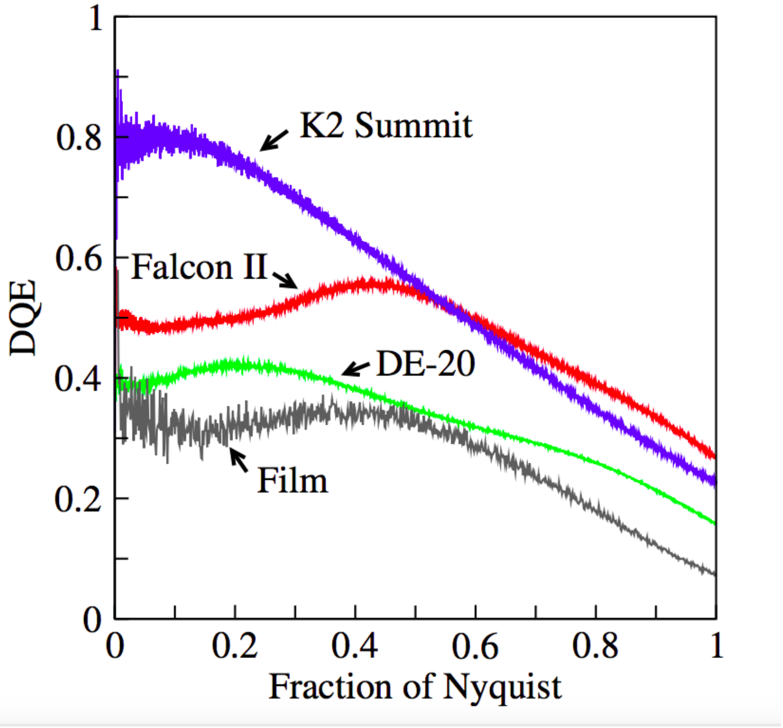

Figure 2-7 Dynamic quantum efficiency of direct electron detectors (McMullan et al., 2014)

The combination of frame-by-frame data collection and accurate electron counting has led to a method of dose filtering to alleviate radiation damage from the electron beam. As the electrons are passed through the biological sample, inelastic energy is built up and results in vibrations, which distort structural information similarly to beam induced drift but typically on a smaller scale. Studies have shown that at about a ~30 electron total dose is where most samples begin to show the effects of radiation damage and side chain information for amino acid residues is lost. This radiation damage decreases the amount of overall high-resolution information captured. Particularly, radiation damage affects polar residues, such as Gln and Asn , damaging them the most (Grant and Grigorieff, 2015). Therefore, the later frames of the electron micrograph movie only maintain low-resolution information. Dose filtering is based on the electron dose of the sample, where the impact of frames can be down weighted when radiation damage is thought to occur. Analysis methods can use a high dose of electrons (>100e-) during data collection to increase the signal-to-noise ratio of small protein samples. Since the lower resolution information is maintained, initial 2D and 3D processing steps can benefit from analyzing this data. During the last steps of refinement, dose filtered data can be used to emphasize the high-resolution information. Overall, the development and application of DEDs has proven to be a tremendous step towards improving EM methods and data (Kühlbrandt, 2014).

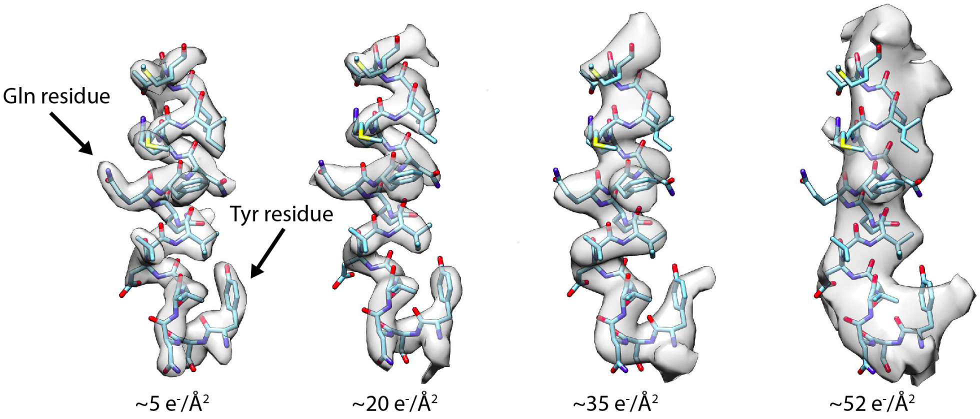

Figure 2-8 Radiation damage during cryo electron microscopy imaging
Sidechain radiation damage from 5-50 electrons/Å^2 (Grant and Grigorieff, 2015)

Atomic modeling

Near atomic density 3D reconstructions from CEM require new atomic modeling programs and present unique challenges. Knowing the phases within an electron microscopy image allows for direct modeling of the density, however density modification procedures used for X-ray crystallography are not easily applicable to density maps from EM. Currently, 3D modeling frequently occurs in real space where *de novo* atomic modeling can be performed. EM has a unique problem for structure modeling where reconstructions can vary widely in resolution. Higher end resolution information near 4Å can be adjacent a flexible domain at 8-10Å resolution. This wide range of resolutions often require a series of modeling packages which work together to best handle modeling within the 3D reconstruction. Accurately fitting all regions of a map has led to methods of iterative model building (Allen and Stokes, 2013; Song et al., 2013). Utilizing previous X-ray, NMR or other structural information is also a powerful tool in modeling EM maps. Atomic model building is continuously being refined and new methods will increase the accuracy of EM as a structure determination technique.

2.3 References

Afonine, P.V., Grosse-Kunstleve, R.W., Echols, N., Headd, J.J., Moriarty, N.W., Mustyakimov, M., Terwilliger, T.C., Urzhumtsev, A., Zwart, P.H., Adams, P.D., 2012. Towards automated crystallographic structure refinement with *phenix.refine*. Acta Crystallogr. D Biol. Crystallogr. 68, 352–367. doi:10.1107/S0907444912001308

Allen, G.S., Stokes, D.L., 2013. Modeling, Docking, and Fitting of Atomic Structures to 3D Maps from Cryo-electron Microscopy. Methods Mol. Biol. Clifton NJ 955, 229–241. doi:10.1007/978-1-62703-176-9_13

Baker, L.A., Rubinstein, J.L., 2010. Radiation damage in electron cryomicroscopy. Methods Enzymol. 481, 371–388. doi:10.1016/S0076-6879(10)81015-8

Bammes, B.E., Jakana, J., Schmid, M.F., Chiu, W., 2010. Radiation damage effects at four specimen temperatures from 4 to 100 K. J. Struct. Biol. 169, 331–341. doi:10.1016/j.jsb.2009.11.001

Broers, A.N., 1967. Electron Gun using Long-Life Lanthanum Hexaboride Cathode. J. Appl. Phys. 38, 1991–1992. doi:10.1063/1.1709807

Carroni, M., Saibil, H.R., 2016. Cryo electron microscopy to determine the structure of macromolecular complexes. Methods San Diego Calif 95, 78–85. doi:10.1016/j.ymeth.2015.11.023

Chen, V.B., Arendall, W.B., Headd, J.J., Keedy, D.A., Immormino, R.M., Kapral, G.J., Murray, L.W., Richardson, J.S., Richardson, D.C., 2010. MolProbity: all-atom structure validation for macromolecular crystallography. Acta Crystallogr. D Biol. Crystallogr. 66, 12–21. doi:10.1107/S0907444909042073

Emsley, P., Lohkamp, B., Scott, W.G., Cowtan, K., 2010. Features and development of *Coot*. Acta Crystallogr. D Biol. Crystallogr. 66, 486–501. doi:10.1107/S0907444910007493

Erdman, P.W., Zipf, E.C., 1982. Low-voltage, high-current electron gun. Rev. Sci. Instrum. 53, 225–227. doi:10.1063/1.1136932

Frank, J., 2006. Three-dimensional electron microscopy of macromolecular assemblies: visualization of biological molecules in their native state, 2nd ed. ed. Oxford University Press, Oxford ; New York.

Grant, T., Grigorieff, N., 2015. Measuring the optimal exposure for single particle cryo-EM using a 2.6 Å reconstruction of rotavirus VP6. eLife 4, e06980. doi:10.7554/eLife.06980

Grigorieff, N., 2007. FREALIGN: high-resolution refinement of single particle structures. J. Struct. Biol. 157, 117–125. doi:10.1016/j.jsb.2006.05.004

Hohn, M., Tang, G., Goodyear, G., Baldwin, P.R., Huang, Z., Penczek, P.A., Yang, C., Glaeser, R.M., Adams, P.D., Ludtke, S.J., 2007. SPARX, a new environment for Cryo-EM image processing. J. Struct. Biol. 157, 47–55. doi:10.1016/j.jsb.2006.07.003

Jung, Y.G., Kang, M.S., Heo, J., 2014. Clustering performance comparison using K-means and expectation maximization algorithms. Biotechnol. Biotechnol. Equip. 28, S44–S48. doi:10.1080/13102818.2014.949045

Kucukelbir, A., Sigworth, F.J., Tagare, H.D., 2013. Quantifying the local resolution of cryo-EM density maps. Nat. Methods 11, 63–65. doi:10.1038/nmeth.2727

Kühlbrandt, W., 2014. Biochemistry. The resolution revolution. Science 343, 1443–1444. doi:10.1126/science.1251652

Lander, G.C., Stagg, S.M., Voss, N.R., Cheng, A., Fellmann, D., Pulokas, J., Yoshioka, C., Irving, C., Mulder, A., Lau, P.-W., Lyumkis, D., Potter, C.S., Carragher, B., 2009. Appion: an integrated, database-driven pipeline to facilitate EM image processing. J. Struct. Biol. 166, 95–102.

Leschziner, A.E., Nogales, E., 2006. The orthogonal tilt reconstruction method: an approach to generating single-class volumes with no missing cone for ab initio reconstruction of asymmetric particles. J. Struct. Biol. 153, 284–299. doi:10.1016/j.jsb.2005.10.012

Li, X., Mooney, P., Zheng, S., Booth, C.R., Braunfeld, M.B., Gubbens, S., Agard, D.A., Cheng, Y., 2013. Electron counting and beam-induced motion correction enable near-atomic-resolution single-particle cryo-EM. Nat. Methods 10, 584–590. doi:10.1038/nmeth.2472

McMullan, G., Faruqi, A.R., Clare, D., Henderson, R., 2014. Comparison of optimal performance at 300 keV of three direct electron detectors for use in low dose electron microscopy. Ultramicroscopy 147, 156–163. doi:10.1016/j.ultramic.2014.08.002

Ohi, M., Li, Y., Cheng, Y., Walz, T., 2004. Negative staining and image classification — powerful tools in modern electron microscopy. Biol. Proced. Online 6, 23–34. doi:10.1251/bpo70

Peisley, A., Skiniotis, G., 2015. 2D Projection Analysis of GPCR Complexes by Negative Stain Electron Microscopy. Methods Mol. Biol. Clifton NJ 1335, 29–38. doi:10.1007/978-1-4939-2914-6_3

Penczek, P.A., 2010. Resolution measures in molecular electron microscopy. Methods Enzymol. 482, 73–100. doi:10.1016/S0076-6879(10)82003-8

Punjani, A., Rubinstein, J.L., Fleet, D.J., Brubaker, M.A., 2017. cryoSPARC: algorithms for rapid unsupervised cryo-EM structure determination. Nat. Methods 14, 290–296. doi:10.1038/nmeth.4169

Radermacher, M., Wagenknecht, T., Verschoor, A., Frank, J., 1987. Three-dimensional reconstruction from a single-exposure, random conical tilt series applied to the 50S ribosomal subunit of Escherichia coli. J. Microsc. 146, 113–136.

Scheres, S.H., 2014. Beam-induced motion correction for sub-megadalton cryo-EM particles. eLife 3, e03665.

Scheres, S.H.W., 2012. RELION: Implementation of a Bayesian approach to cryo-EM structure determination. J. Struct. Biol. 180, 519–530. doi:10.1016/j.jsb.2012.09.006

Scheres, S.H.W., Chen, S., 2012. Prevention of overfitting in cryo-EM structure determination. Nat. Methods 9, 853–854. doi:10.1038/nmeth.2115

Sigworth, F.J., Doerschuk, P.C., Carazo, J.-M., Scheres, S.H.W., 2010. An introduction to maximum-likelihood methods in cryo-EM. Methods Enzymol. 482, 263–294. doi:10.1016/S0076-6879(10)82011-7

Skiniotis, G., Southworth, D.R., 2016. Single-particle cryo-electron microscopy of macromolecular complexes. Microsc. Oxf. Engl. 65, 9–22. doi:10.1093/jmicro/dfv366

Song, Y., DiMaio, F., Wang, R.Y.-R., Kim, D., Miles, C., Brunette, T., Thompson, J., Baker, D., 2013. High-resolution comparative modeling with RosettaCM. Struct. Lond. Engl. 1993 21, 1735–1742. doi:10.1016/j.str.2013.08.005

Swanson, L.W., Martin, N.A., 1975. Field electron cathode stability studies: Zirconium/tungsten thermal-field cathode. J. Appl. Phys. 46, 2029–2050. doi:10.1063/1.321893

Takizawa, Y., Binshtein, E., Erwin, A.L., Pyburn, T.M., Mittendorf, K.F., Ohi, M.D., 2017. While the revolution will not be crystallized, biochemistry reigns supreme. Protein Sci. Publ. Protein Soc. 26, 69–81. doi:10.1002/pro.3054

Tang, G., Peng, L., Baldwin, P.R., Mann, D.S., Jiang, W., Rees, I., Ludtke, S.J., 2007. EMAN2: An extensible image processing suite for electron microscopy. J. Struct. Biol. 157, 38–46. doi:10.1016/j.jsb.2006.05.009

Umrath, W., 1974. Cooling bath for rapid freezing in electron microscopy. J. Microsc. 101, 103–105. doi:10.1111/j.1365-2818.1974.tb03871.x

Van Heel, M., 1987. Angular reconstitution: a posteriori assignment of projection directions for 3D reconstruction. Ultramicroscopy 21, 111–123.

van Heel, M., Schatz, M., 2005. Fourier shell correlation threshold criteria. J. Struct. Biol. 151, 250–262. doi:10.1016/j.jsb.2005.05.009

Xueming, L., 2016. Recent technical advancements enabled atomic resolution CryoEM [WWW Document]. URL http://cpb.iphy.ac.cn/article/2016/1806/cpb_25_1_018710.html#outline_anchor_14 (accessed 7.25.17).

Yang, Z., Fang, J., Chittuluru, J., Asturias, F.J., Penczek, P.A., 2012. Iterative stable alignment and clustering of 2D transmission electron microscope images. Struct. Lond. Engl. 1993 20, 237–247. doi:10.1016/j.str.2011.12.007

Chapter 3

Spiral architecture of the Hsp104 disaggregase reveals the basis for polypeptide translocation[1]

3.1 Abstract

Hsp104 is a conserved member of AAA+ protein disaggregases that promotes survival during cellular stress. Hsp104 remodels amyloids, supporting prion propagation, and disassembles toxic oligomers connected to neurodegenerative diseases. A definitive structural mechanism of its disaggregase activity, however, has remained elusive. We have determined the ATP-state cryo-EM structure of wildtype *Saccharomyces cerevisiae* Hsp104, revealing a near-helical hexamer architecture that coordinates the mechanical power of the twelve AAA+ domains for disaggregation. An unprecedented heteromeric AAA+ interaction defines an asymmetric seam in an apparent catalytic arrangement that aligns the domains in a two-turn spiral. N-terminal domains form a broad channel entrance for substrate engagement and Hsp70 interaction. Middle-domain helices bridge adjacent protomers across the nucleotide pocket, explaining roles in ATP hydrolysis and protein disaggregation. Remarkably, substrate-binding pore loops line the channel in a spiral arrangement likely optimized for

---

[1] Data included in this chapter were published in

Yokom, A.L., Gates, S.N., Jackrel, M.E., Mack, K.L., Su, M., Shorter, J., Southworth, D.R., 2016. Spiral architecture of the Hsp104 disaggregase reveals the basis for polypeptide translocation. Nat. Struct. Mol. Biol. 23, 830–837. doi:10.1038/nsmb.3277

Gates, S.N.*, **Yokom, A.L**.*, Lin, J., Jackrel, M.E., Rizo, A.N., Kendsersky, N.M., Buell, C.E., Sweeny, E.A., Mack, K.L., Chuang, E., Torrente, M.P., Su, M., Shorter, J., Southworth, D.R., 2017. Ratchet-like polypeptide translocation mechanism of the AAA+ disaggregase Hsp104. Science. doi:10.1126/science.aan1052 *Authors contributed equally substrate transfer across the AAA+ domains, establishing a continuous path for polypeptide translocation.

3.2 Introduction

Heat shock protein (Hsp) 104, found in yeast, is a member of the Hsp100 class of molecular chaperones that contain highly conserved AAA+ (ATPases Associated with diverse cellular Activities) domains and serve essential roles in thermotolerance and protein quality control (Mogk et al., 2015; Parsell et al., 1994b; Sanchez and Lindquist, 1990). Hsp104 and its bacterial homolog, ClpB, form large hexameric-ring structures that cooperate with the Hsp70 system to unfold and rescue aggregated protein states by active translocation of polypeptide substrates through a central channel (Glover and Lindquist, 1998; Lum et al., 2004; Weibezahn et al., 2004). In addition to solubilizing stress-induced disordered aggregates (Motohashi et al., 1999; Weibezahn et al., 2004). Hsp104 recognizes and remodels cross-β structures of amyloid fibrils, such as those found in Sup35 prions, which enables Hsp104 to control prion inheritance in yeast (Chernoff et al., 1995; Moriyama et al., 2000; Shorter, 2004). This function in prion disaggregation is enhanced in Hsp104 compared to ClpB, and studies have identified potentiated Hsp104 variants that reduce the toxicity of proteins linked to neurodegenerative diseases including TDP-43, FUS and α-synuclein (Cushman-Nick et al., 2013; Jackrel and Shorter, 2014; Lo Bianco et al., 2008). Despite fundamental roles in protein quality control and promising therapeutic activity in rescuing amyloidogenic states (Jackrel and Shorter, 2014) how Hsp104 and its family members function as powerful molecular motors to solubilize proteins is not fully understood.

Hsp104 and ClpB contain a mobile N-terminal domain (NTD), implicated in substrate engagement (Doyle et al., 2012; Rosenzweig et al., 2015) two evolutionarily distinct AAA+ nucleotide binding domains (NBD1 and NBD2) that bind substrates and power translocation, and a middle domain (MD) that is required for disaggregation and interaction with Hsp70 (Figure 3-1, top) (DeSantis et al., 2014; Kedzierska et al., 2003; Lee et al., 2013; Rosenzweig et al., 2013; Seyffer et al., 2012). Hsp104 also contains a C-terminal domain (CTD) not found in ClpB that is required for hexamerization (Mackay et al., 2008).The crystal structure of ClpB (Lee et al., 2003) from a thermophilic eubacterium (*Thermus thermophilus*) identified the conserved type II AAA+ domain architecture allowing the identification of major secondary structure and domain motifs (Figure 3-1, bottom). Helices are designated as they are for the ClpB structure throughout our studies.

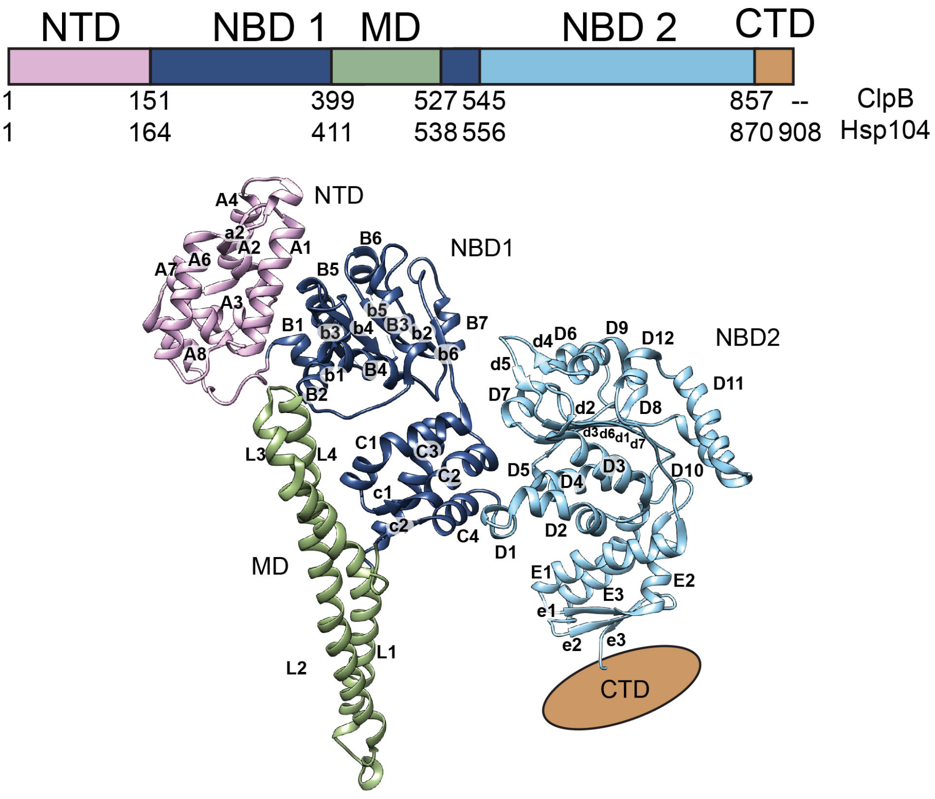

Figure 3-1 Schematic of Hsp104 sequence (top) Cartoon of the domain arrangement of Hsp104 and ClpB. (bottom) Labeled Hsp104 SWISSPROT homology model based on the ClpB crystal structure (pdb=1QVR).

Seen in the ClpB crystal structure, the NBDs are comprised of large and small subdomains that form the ATP binding pocket and contain the respective Walker A and B motifs and ‘sensor’ residues required for ATP hydrolysis. The MD, located within the small subdomain of NBD1, forms an ~85 Å-long flexible coiled-coil that is proposed to adopt a number of conformations in the hexamer during the hydrolysis cycle (Figure 3-1 , bottom) (Carroni et al., 2014; Lee et al., 2007; Sweeny et al., 2015; Wendler et al., 2007). The structural information was limited for this ClpB structure, since it formed a dimer of trimers within the crystal lattice (Lee et al., 2003), which is a common crystal packing arrangement for AAA+ proteins (CITE **). Therefore, high-resolution hexameric models still proved unobtainable by X-ray crystallography.

Polypeptide translocation between NBD1 and NBD2 is controlled via allosterically driven ATP hydrolysis events (Hattendorf, 2002; Wendler et al., 2009) and, for Hsp104; cooperativity between protomers is required for disaggregation of highly stable amyloids (DeSantis et al., 2012). Substrate binding is favored in the ATP-bound state (Bösl et al., 2005), and involves direct interaction with highly conserved tyrosine residues in flexible NBD “pore loops” (Lum et al., 2004; Tessarz et al., 2008; Weibezahn et al., 2004) that are proposed to line the axial channel and operate by hydrolysis-driven substrate hand-off cycles. How this occurs across the 100 Å-long channel and between the two distinct AAA+ domains remains unknown. Early studies to investigate the hexameric arrangement of Hsp104 and Clpb produced a number of cryo-EM models at modest resolutions between 11 and 20 Å of mutant Hsp104 (Tessarz et al., 2008; Wendler et al., 2009, 2007) and ClpB (Lee et al., 2007, 2003). Generally, these models show a symmetric hexamer with three distinct rings comprised of the NTD, NBD1, and NBD2 (Figure 3-2). Structural studies have also identified different nucleotide states that involve changes in the pore diameter and conformation of the domains (Lee et al., 2007; Sweeny et al., 2015; Wendler et al., 2009). The oligomeric state, however, is dynamic, requiring presence of nucleotide for stability (Parsell et al., 1994a) and the protomers exchange rapidly during the hydrolysis cycle (Aguado et al., 2015; DeSantis et al., 2012; Werbeck et al., 2008); consequently, the high-resolution architecture of the hexameric, active complex has remained out of reach.

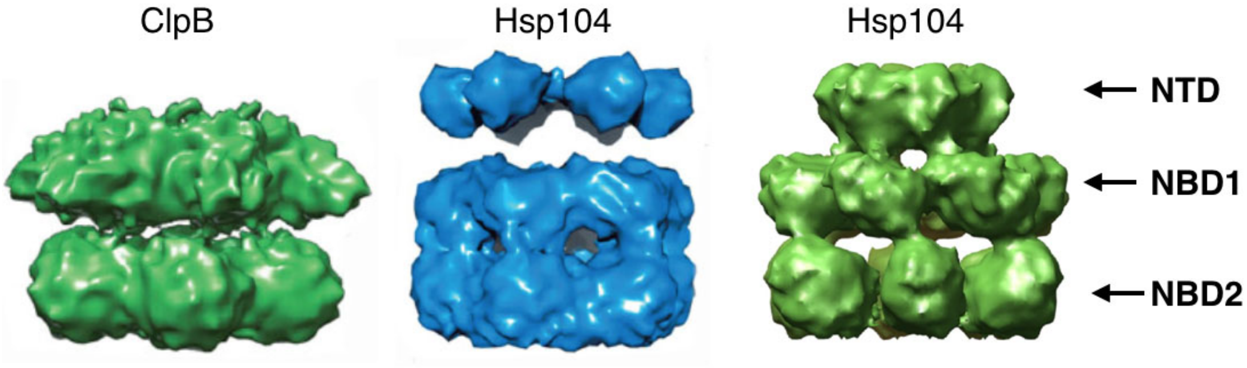

Figure 3-2 Previous studies of HSP100s reveal a three tier structural arrangement. Symmetry imposed EM reconstructions of Hsp104 and ClpB.

We sought to elucidate the underlying structural mechanism of the Hsp104 disaggregase. We determined the cryo-EM structure of wild-type Hsp104 from yeast (*Saccharomyces cerevisiae*) bound to AMP-PNP (a nonhydrolyzable ATP analog) at 5.6 Å resolution. The structure reveals a helical-like arrangement involving a 10-Å rise between protomers that results in a seam where the first protomer is offset by more than 40 Å from the sixth. This offset brings NBD1 from one protomer into contact with NBD2 in the adjacent protomer, forming a heteromeric AAA+ interaction at the seam. Well-defined density corresponding to the conserved Tyr pore loops presents a spiral of substrate-binding surfaces along the axial channel. Remarkably, the protomer offset optimally positions the NBD1 and NBD2 pore loops at the seam for coordinated transfer of substrates across the AAA+ domains.

3.3 Results

Hsp104 hexamer adopts asymmetric spiral architecture

We determined the cryo-EM structure of the intact, wild-type Hsp104 complex in the presence of AMP-PNP to mimic the substrate-binding ATP state (Shorter, 2004). Purified Hsp104 was functionally active in ATPase and disaggregase assays (Figure 3-3, top left and middle). Cryo-EM images of Hsp104-AMP-PNP show homogeneous oligomeric complexes (Figure 3-3, top right). Initially, extensive cryo-EM condition screening of an Apo-Hsp104 complex showed broken hexamers or monomeric Hsp104. This confirmed that the presence of nucleotide was needed for stable hexamer formation, which has previously been proposed. Single particle analysis of ~200,000 single particles yielded variety of distinct views with well-resolved structural features via reference-free 2D classification. These 2D averages reveal clear top-view ring shapes and side-view projections with three layers that show a striking asymmetry and unique protomer arrangement that is different from what has been described previously (Figure 3-3, bottom) (Wendler et al., 2009, 2007).

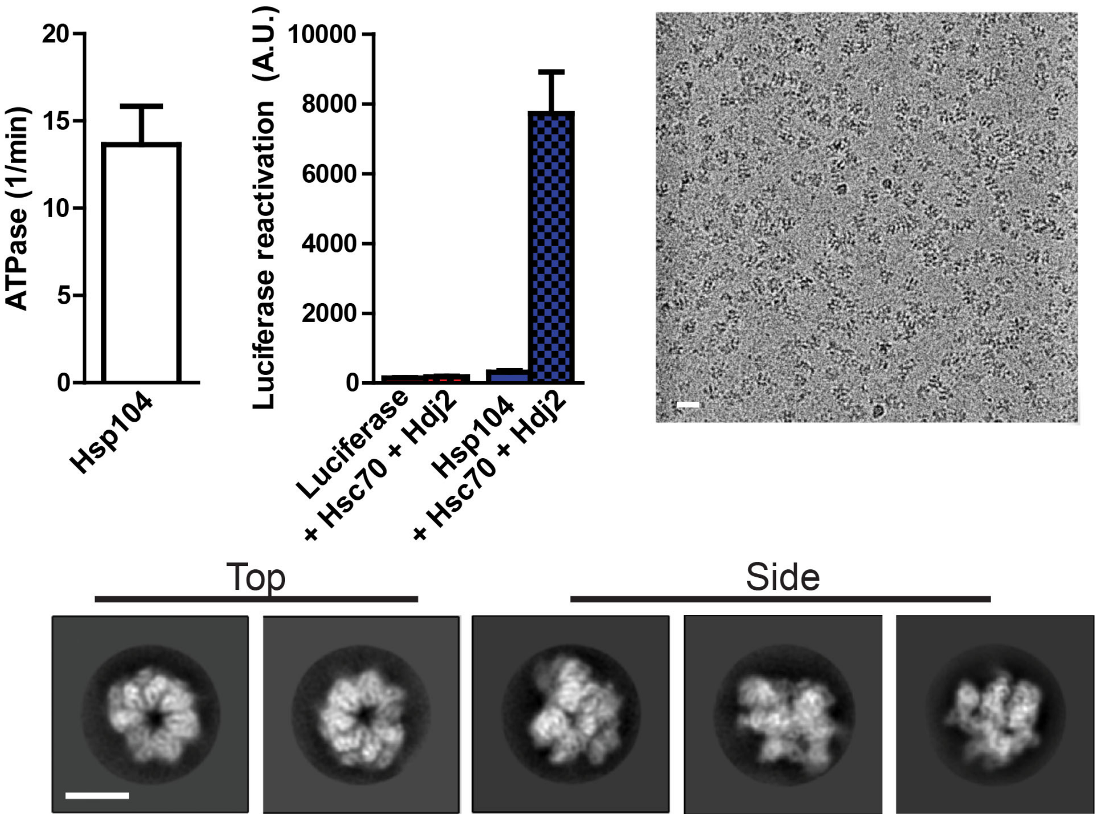

Figure 3-3 Functional analysis and 2D classification of Hsp104-AMPPNP
(top, left) Purified Hsp104 is active in both ATPase and luciferase refolding assays. (top, right) Representative cryo-EM micrograph of Hsp104-AMPPNP hexamers. Scale bar equals 200 Å. (bottom) Reference free 2D class averages of Hsp104-AMPPNP shown in top and side views. Scale bar= 100Å. Assays were performed by Meredith Jackrel

The final cryo-EM reconstruction following 3D refinement with no imposed symmetry was achieved at indicated resolutions of 6.5 Å and 5.6 Å for the un-masked and masked maps, respectively (Figure 3-4, right). The final map comprised of ~160,000 (85%) of the single particle data. To ensure no additional conformations or oligomeric states were present, 3D classification was tested dividing the data into four separate 3D reconstructions. All four classes showed identical hexameric states and were combining for 3D reconstruction refinement. The angular distribution of the particles showed several preferred orientations but these hot spots did not prevent 3D reconstruction to high resolution (Figure 3-4, left). To confirm the accuracy of our 3D model to the reference free data, 2D projections of the 3D map were matched to the 2D class averages and indeed they corresponded extremely well.

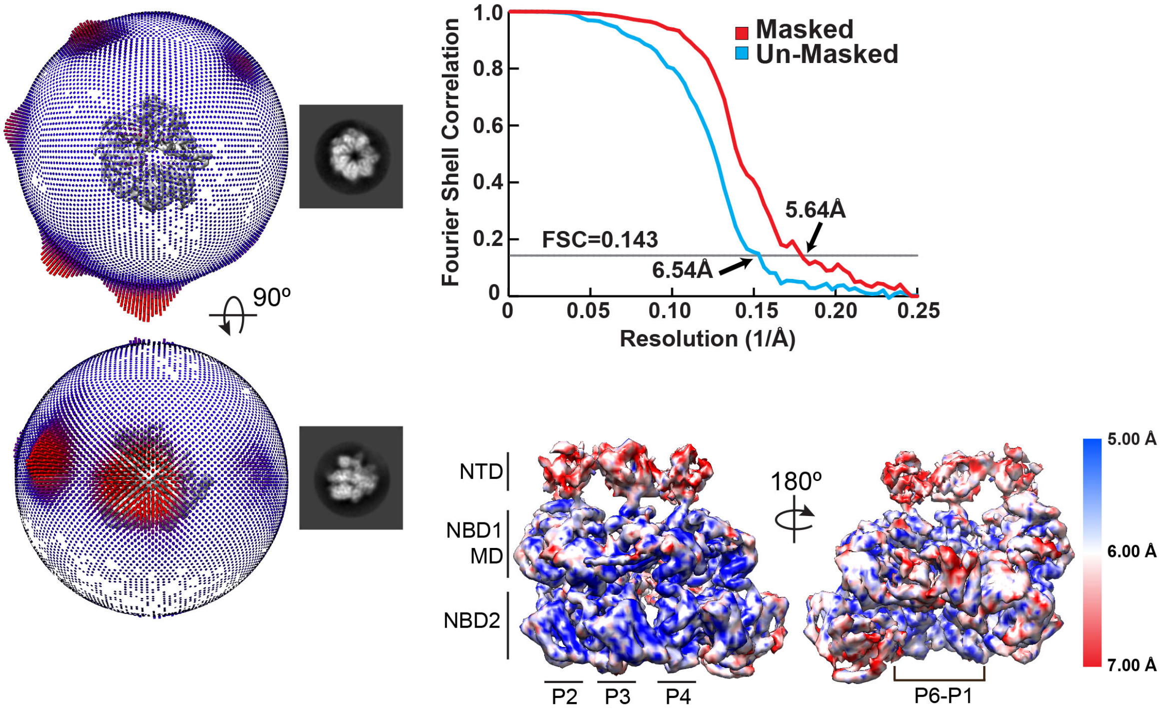

Figure 3-4 Cryo-EM analysis of Hsp104-AMPPNP (left) 3D plot of the angular distribution of the single particles in the final reconstruction. Red represents a high quantity and blue represents a low quantity of particles. (top, right) Gold standard FSC curve for the un-masked and masked reconstructions of the final model estimated from the FSC=0.143 criterion to be 6.54 Å and 5.64 Å, respectively. (bottom, left) Local resolution of the 3D reconstruction determined by ResMap[1] and shown from 5 Å (blue) to 7 Å (red).

The final 3D reconstruction reveals Hsp104-AMP-PNP is a ring-shaped hexamer with three distinct domain-layers that correspond to the NTD, NBD1-MD and NBD2, consistent with other studies (Figure 3-5) (Lee et al., 2010; Wendler et al., 2009, 2007). However, in striking contrast to previous models, the protomers are arranged in a helical spiral and the NBD rings connect together to form a distinct asymmetric seam. The

NBD1 and NBD2 show the highest resolution density, at approximately 5 Å, while the NTDs as well as regions at the hexamer seam are more flexible and at ~6-7 Å resolution. Density for the MD coiled-coil is partly resolved on one face of the hexamer where it wraps around the outside of the hexamer adjacent to the NBD1s (Figure 3-5). The central channel is approximately 25-30 Å in diameter, but opens to form a wide cleft at the hexamer seam due to the spiral offset of the adjacent protomers.

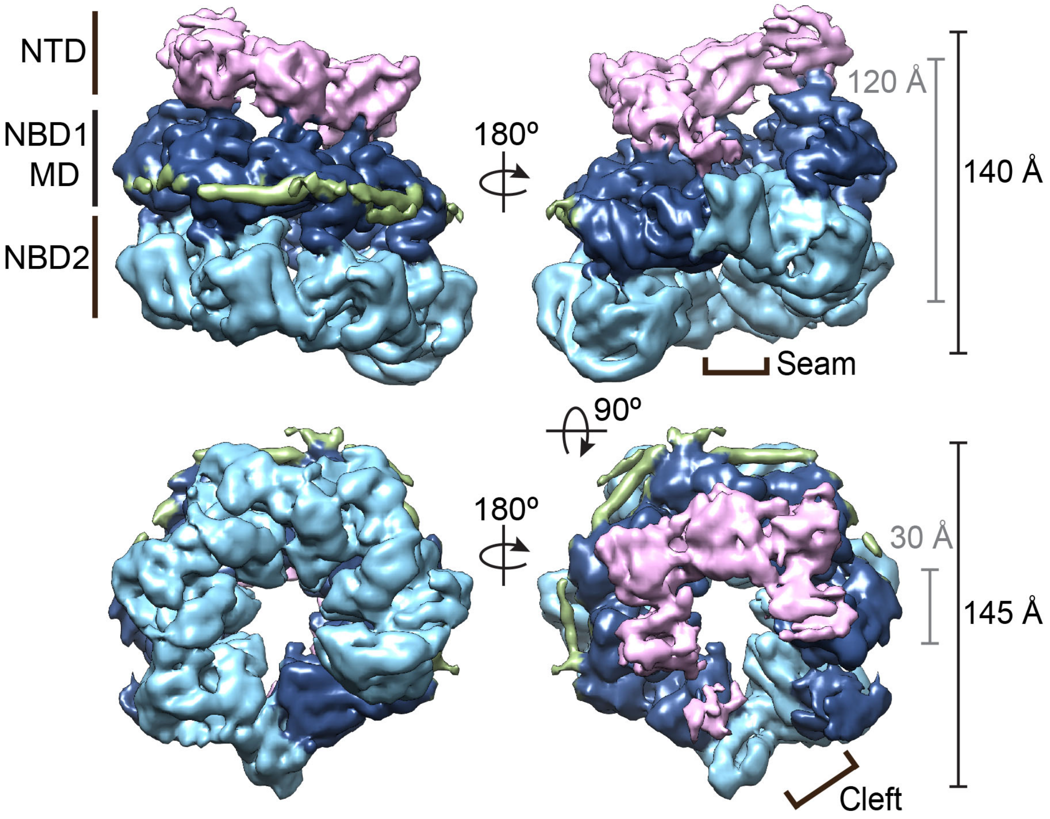

Figure 3-5 Cryo EM reconstruction of Hsp104-AMPPNP. Views of the final sharpened 3D density map (4σ) of Hsp104, showing a spiral three-tier architecture. The domains are colored as in **a**, on the basis of the atomic model. Approximate dimensions of the channel (gray) and exterior (black) are shown, and the hexamer seam and channel cleft are indicated.

The crystal structure from *Thermus thermophilus* ClpB (Lee et al., 2003) (PDB: 1QVR), which has ~45% sequence identity with Hsp104, was used for initial fitting and to determine a homology model for Hsp104. The reconstruction was docked by rigid body fitting of the domains followed by flexible fitting to achieve an atomic model with the highest correlation to the map, at 0.92. The protomers are designated 1 through 6, with protomer 1 (P1) in the highest position in the side-view orientation, and proceeding counterclockwise when viewed from the NTD-face (Figure 3-6). The NBDs fit well, with a cross-correlation value of 0.94, and identify the conserved AAA+ subdomain architecture with α-helical and β-sheet regions that are well resolved for each of the protomers (Figure 3-7). Difference map analysis between the final map and a nucleotide free model indicate nucleotide is present in the majority NBDs, with clear density observed in 9 sites, reduced density in two sites, indicating partial occupancy or flexibility, and no density at one site.

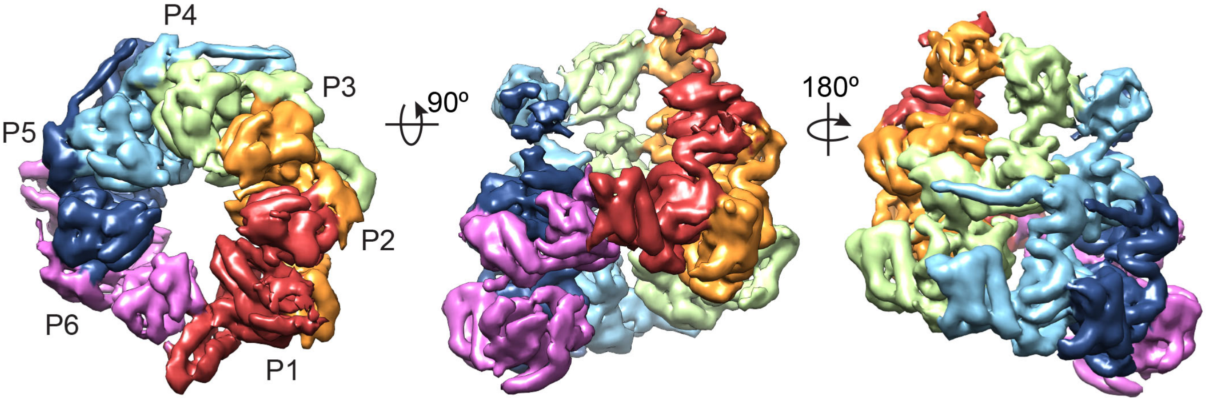

Figure 3-6 Protomer arrangement of Hsp104 Top view, showing NBD1 density and protomer labels, and side views of the sharpened map (5σ). Each protomer is colored according to the molecular model.

When inspecting the NBDs, the 5Å resolution in these regions allowed accurate carbon backbone positioning of all critical residues. NBD1s show a canonical AAA+ arrangement, including expected positions for the Walker A (K218), Walker B (E285), and sensor-1 (T317) residues. Putative arginine finger residues R334 and R333

(Wendler et al., 2007) are within 7 and 10 Å, respectively, of the nucleotide pocket of the adjacent protomer, indicating a catalytically active arrangement. The NBD2s are similarly well defined showing conserved interprotomer interactions and positions for the Walker A (K620), Walker B (E687), sensor-1 (N728) and sensor-2 (R826) residues, and the proposed arginine finger (R765) (Mogk et al., 2003) is near the nucleotide pocket, at less than 10 Å, based on our model (Figure 3-7). Protomers P1 and P6 that make up the unusual hexamer seam are in a different conformation and are discussed in further detail below.

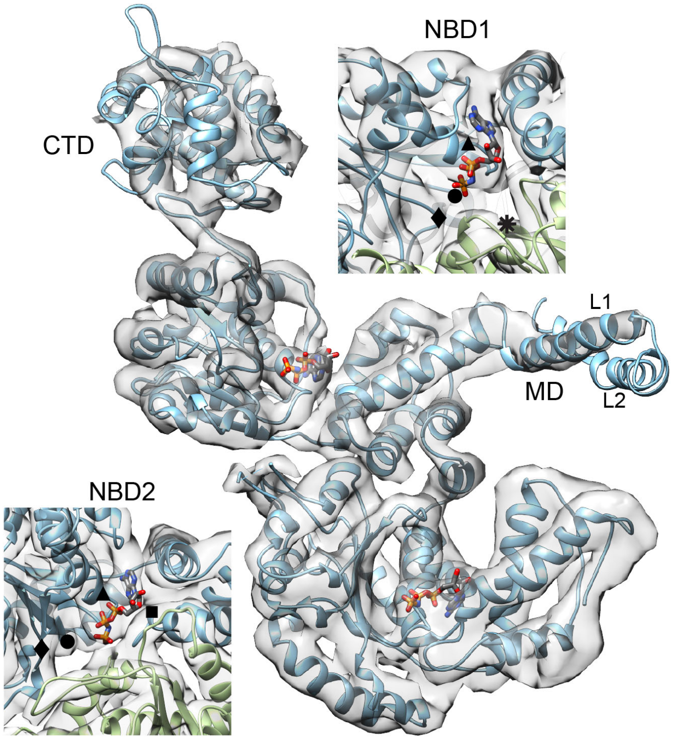

Figure 3-7 Single protomer shows secondary structure and nucleotide density Molecular model of a segmented protomer (P4), showing bound nucleotides and well-resolved density for the NBD1 and NBD2 AAA+ domains. Enlarged views of the nucleotide pockets are shown with indicated positions for Walker A (triangle), Walker B (diamond), sensor 1 (circle), sensor 2 (square) and arginine-finger (asterisk) residues

Heteromeric NBD1-NBD2 interaction defines the hexamer seam

The most striking structural feature of the Hsp104 hexamer is the helical-like arrangement of the protomers. While canonical AAA+ interactions are generally maintained around the hexamer, each protomer is tilted slightly, resulting in an approximate 7-fold helical symmetry. Going from P1 to P6, the protomers each rise nearly 10 Å and rotate 53°, on average (Figure 3-8). The individual protomers vary in conformation and position around the hexamer, indicating the complex is indeed asymmetric. When the NBD1s are superimposed, continuous conformational changes are observed from P1-P6, while the greatest protomer differences are between P1 and P6 at the hexamer seam. The conformational changes primarily involve rotations of the NBD1 and NBD2 small subdomains, which move inward relative to the channel axis by approximately 10° and 20°, respectively, resulting in a more compact P1 protomer compared to P6.

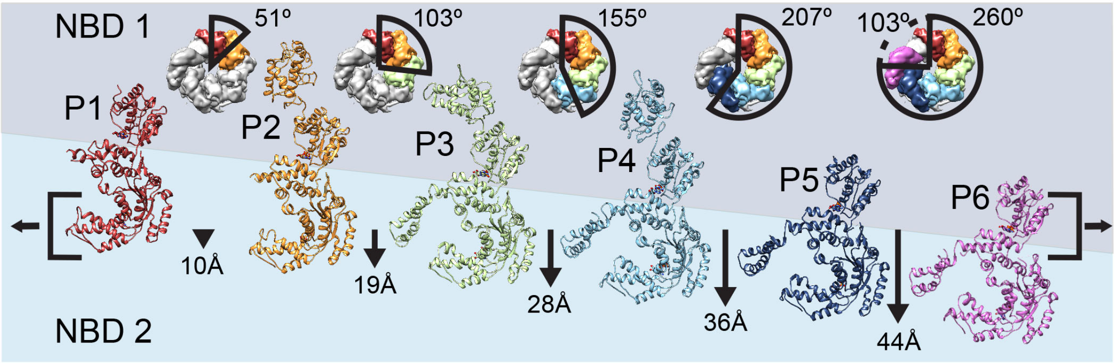

Figure 3-8 Basis for the protomer spiral arrangement Protomer positions shown in top views and individually unrolled from the hexamer, with the indicated rotation and translation shift relative to P1. Brackets indicate alignment of NBD1 and NBD2 AAA+ domains for P6 and P1, respectively**.**

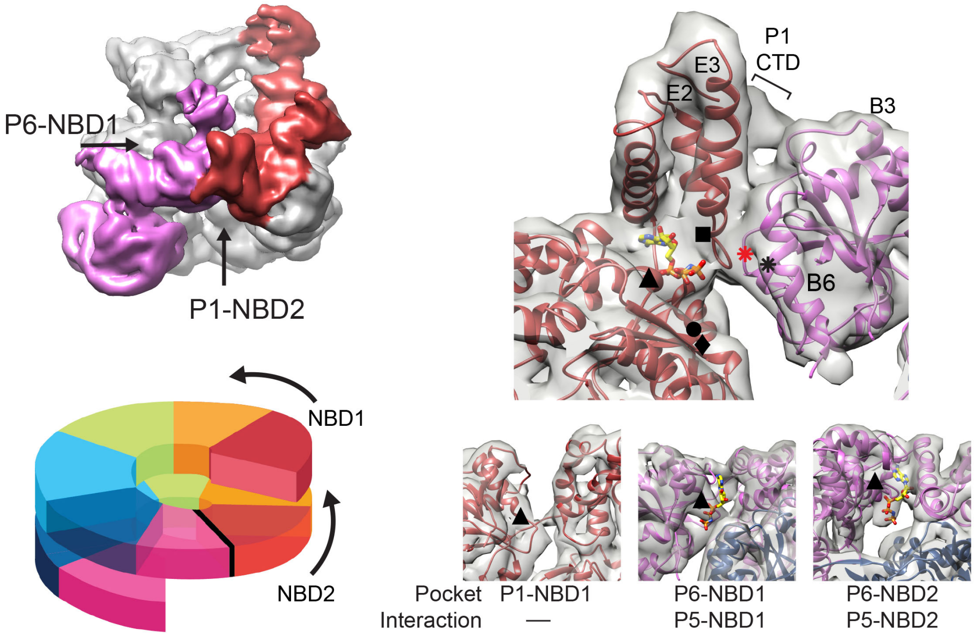

Figure 3-9 NBD1-NBD2 AAA+ interaction at the hexamer seam (top, left) Low-pass-filtered map colored for P1 (red) and P6 (magenta), highlighting the P6 NBD1–P1 NBD2 interaction. (bottom, left) Cartoon model showing that the NBD1 and NBD2 AAA+ domains connect and form a two-turn spiral. (right) Expanded view of the model and map showing the NBD1-NBD2 interaction from inside the channel. Interface regions are indicated: B3 and B6 helices (NBD1 large subdomain), E2 and E3 helices (NBD2 small subdomain) and the P1 CTD. Positions for the Walker A (triangle), Walker B (diamond), sensor 1 (circle), sensor 2 (square) and putative arginine-finger residues R333 and R334 (asterisk) and R307 (red asterisk) are indicated. Nucleotide pockets for the P1 NBD1, P6 NBD1 and P6 NBD2 are shown with Walker A residues (triangle) indicated. Nucleotide is shown for sites with density observed in the pocket.

The helical shift of the protomers results in a 44 Å-offset between P1 and P6, yet these protomers interact together, covering a 100° rotation around the channel axis to complete the hexamer ring (Figure 3-9, top left). Remarkably, this large offset positions the P6-NBD1 adjacent the P1-NBD2, resulting in an in an NBD1-NBD2 interaction that connects the AAA+ domains in a two-turn spiral (Figure 3-9. bottom left). Although at a slightly lower resolution compared to other protomers, density is well defined in this region and reveals interactions that are mediated by the B3 and B6 connecting loops from the P6-NBD1 and helices E2 and E3 from the P1-NBD2 (Figure 3-9, right). Density corresponding to the P1-CTD also contacts the P6 NBD1, towards the outside of the channel, potentially stabilizing the interaction.

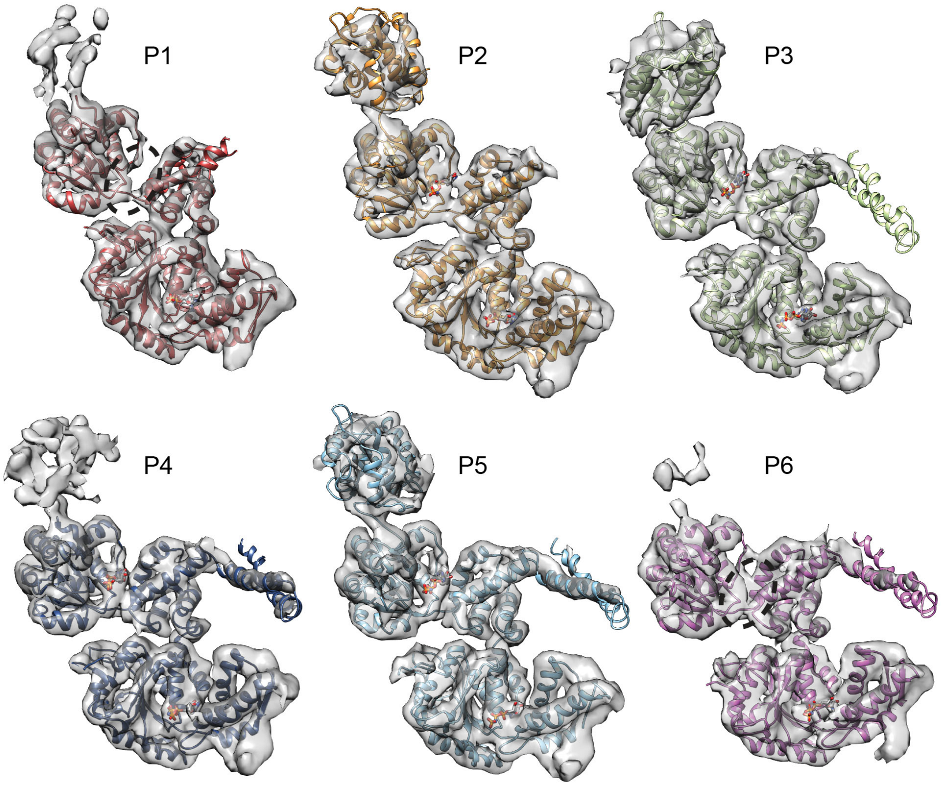

Figure 3-10 Molecular models of the Hsp104 protomers Hsp104 molecular models for each protomer in the asymmetric hexamer with the segmented density shown at 5σ. AMPPNP is shown as sticks where density is observed in the pocket for the difference maps.

Despite the unusual NBD1-NBD2 interaction, density is present that corresponds to bound nucleotide for the P1-NBD2, indicating a potentially active, catalytic site. This site looks similar to the other protomer and when the density for each is isolated this can be seen (Figure 3-10). While the inter-protomer AAA+ interaction is different compared to the more canonical interfaces at the other sites, putative arginine finger residues R334 and R333 in the P6-NBD1 are localized approximately 10-12 Å away from the P1-NBD2 nucleotide pocket. Interestingly, another highly conserved arginine residue, R307 in P6, is within 5 Å of the P1-NBD2 pocket. Thus, either a small conformational change that repositions R334 or R333 or activation by R307 could support ATP hydrolysis. In contrast, density is not observed in the P1-NBD1 pocket, indicating nucleotide is not present (Figure 3-9, right). However, because of the protomer offset, P1-NBD1 is not supported by an adjacent AAA+ domain from P6, thus the nucleotide pocket is likely destabilized and inactive. Despite the adjacent P5-NBD1 in an apparent canonical orientation, density in the P6-NBD1 pocket appears weak relative to the other protomers, indicating partial occupancy or flexibility. Finally, density for nucleotide is observed for the P6-NBD2; this site is supported by the adjacent P5-NBD2, which is in a similar arrangement to the other protomers. Overall, comparison of the AAA+ domains for protomers 1 and 6 reveals a mix of nucleotide states and an asymmetric structural organization with distinct interactions relative to the rest of the hexamer that potentially support unique functions during disaggregation.

Arrangement of the MD and NTD highlight critical functions

The conserved NTDs bind hydrophobic regions of substrates and are proposed to direct polypeptides to the NBD pore loops as well as enhance cooperative substrate binding required for amyloid disaggregation (Rosenzweig et al., 2015; Sweeny et al., 2015). In our Hsp104 map the P1-P5 NTDs surround the axial channel, forming a C-shaped entrance that is approximately 35 Å in diameter (Figure 3-11, left). The opening widens substantially to approximately 50 Å moving towards the P6 NTD at the hexamer seam, creating a large cleft that opens along the side of the hexamer. Although the P6-NTD is more flexible and less well resolved, interactions between the adjacent P5-NTD as well as an unusual interaction with P1-NBD2 are identified when viewed at a reduced threshold for the density. Because of the NTD separation, the P1-NBD1 largely defines an equatorial channel entrance. Based on the arrangement in the other protomers, the P1-MD would extend across the cleft towards the P6-NTD, however density was not sufficiently resolved for localization. Based on modeling the P2-P4 NTDs, only the P3 NTD appears to be positioned with its hydrophobic substrate-binding cleft (Rosenzweig et al., 2015) facing towards the channel, while the P2 and P4 NTDs each adopt different orientations (Figure 3-11, right). Thus, while the NTDs interact to form a defined ring at the channel entrance, the interfaces are variable and multiple conformations are adopted around the hexamer, which could enable binding to heterogeneous protein aggregate surfaces.

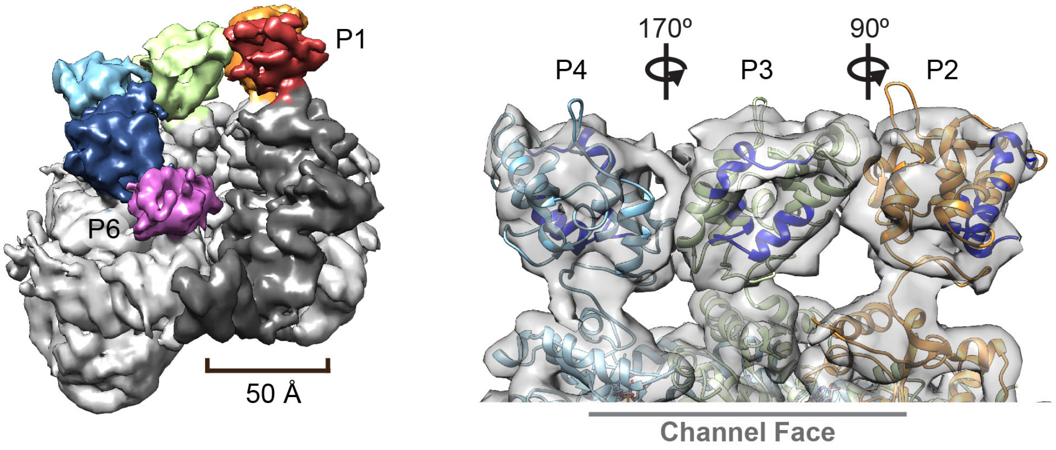

Figure 3-11 NTD conformational states (left) 3D map in a tilted orientation showing the NTDs, colored by protomer, interacting around the channel entrance and the 50-Å-wide cleft defined by the P1 and P6 NTDs and P1 AAA+ (dark gray). (right) Enlarged view of the modeled P2–P4 NTDs, showing different orientations around the NBD1 connecting linker. Rotations are relative to P3, and hydrophobic substrate–binding sites are indicated (blue).

Conversely, the channel exit on the opposite face of the hexamer is largely defined by the NBD2, however an additional lobe of density is observed in all protomers, which we predict corresponds to the 38-residue CTD (Figure 3-12, left). The density emerges from the NBD2 C-terminal site identified based on ClpB and extends to form a defined bridge connection to the adjacent protomer by contacting helix D11 in NBD2 (Figure 3-12, right). The interaction likely stabilizes the hexamer, supporting previous studies (Mackay et al., 2008) and the CTD position around the channel exit also rationalizes previously proposed functions in cochaperone binding (Abbas-Terki et al., 2001), and thus could serve as a docking point for substrate hand-off to downstream chaperone systems.

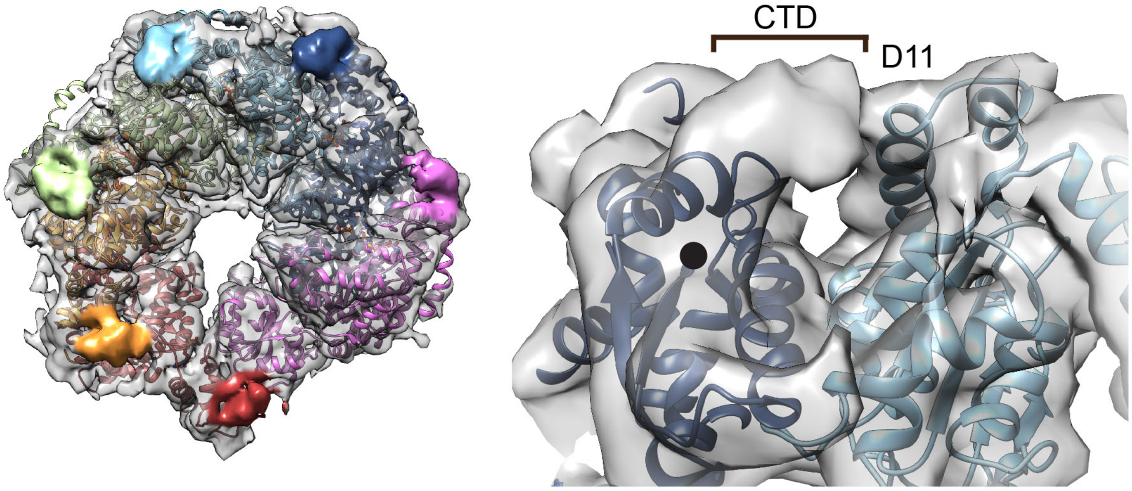

Figure 3-12 CTD bridging around the hexamer ring (left) View of the NBD2 channel exit face of the hexamer with the density corresponding to the CTDs colored by protomer. (right) Enlarged view of the P5 CTD density extending from the NBD2 C terminus (circle) and interacting with P4 NBD2, at adjacent helix D11.

Density corresponding to the MD coiled-coil that is partly resolved for P3-P6 was docked with residues 409-467 that correspond to helix L1 and part of helix L2 that connect to the NBD1 large subdomain (Figure 3-13, top left). Density for the C-terminal-half of the extended, 85 Å helix L2 as well as helix L3 and helix L4, which includes Hsp70 interaction sites (Rosenzweig et al., 2013) could not be clearly identified, indicating this portion of the MD remains flexible. Based on the fit of the MD L1-L2 helices for P3-P6, the MD is rotated 47° rotation compared to the crystal structure and directly contacts NBD1 of the adjacent protomer (Figure 3-13, top left). L1 and L2 are positioned alongside the clockwise neighbor, and together with helix C3, form a 60 Å-long strap across the small and large AAA+ subdomains (Figure 3-13, top right). The interaction is with the opposite protomer that makes up the canonical AAA+ interface, such that each NBD1 is supported by the MD of one neighbor and the large AAA+ subdomain of the other neighbor. Density in this region is well defined for helix L1, which contacts helix C1, the C1-C2 connecting loop and part of helix B3 in the neighboring protomer. The interaction appears to involve conserved residues R419, E427, and D434, which have been previously identified to be critical for function (Dulle et al., 2014; Oguchi et al., 2012; Wendler et al., 2007). We identify that these residues are positioned to interact with E190, R353 and R366, respectively, in the adjacent NBD1, making stabilizing salt-bridge interactions (Figure 3-13, bottom).

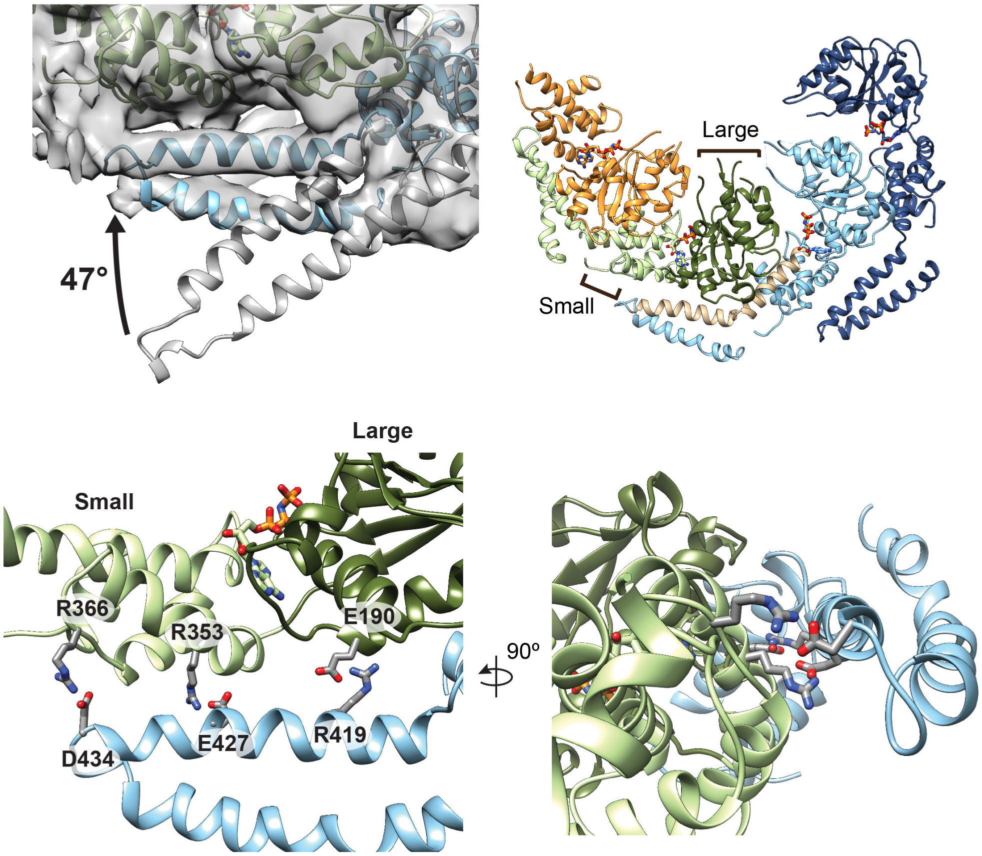

Figure 3-13 MD conformational state forms a unique NBD1-MD interaction
(top, right) Comparison between the MD L1 and L2 orientation based on the docked ClpB structure (gray) and Hsp104 model showing 47° rotation around C3–L1 connecting residues (409–410) to fit the density. (top, right) View of the NBD1 MD interactions for P2–P5, showing helices C3–L1 (brown) bridging across the large (dark green) and small (light green) subdomains of the adjacent protomer (bottom) Views showing model with proposed salt bridge interactions between MD-L1 and adjacent NBD1 that bridge the large and small AAA+ subdomains across nucleotide-binding pocket.

Mutagenesis of MD-NBD1 Contacts

The AMPPNP-specific MD L1-NBD1 interaction has not been characterized. Therefore, single charge-reversal mutations were introduced to disrupt three putative L1-NBD1 salt bridges: E412-R194, E427-R353, and D434-R366. These mutants exhibit robust ATPase activity (Figure 3-14, top right). Particularly in the case of R366E which is above wild type levels. This suggests there may be a regulator function of this interaction and may explain some of the previous MD allosteric effects. To further investigate the functional consequences of this interaction we turned to established refolding luciferase assays and thermotolerance assays to monitor *in vivo* functions. Under normal conditions Hsp104 is recruited to luciferase aggregates and can refold nearly 100% into functional monomers (Figure 3-14, top left). However, any single point mutations within these three salt bridges abolished function. I can hypothesize that this dysfunction is due to increased flexibility and thus lower affinity for Hsp70, but this has not been proven. A similar result is seen in yeast survival assays, where Hsp104 loses the ability to confer thermotolerance *in vivo* (Figure 3-14, bottom). These functional assays show the importance of this MD-NBD1 interaction but the mechanism allosteric effects are still a mystery.

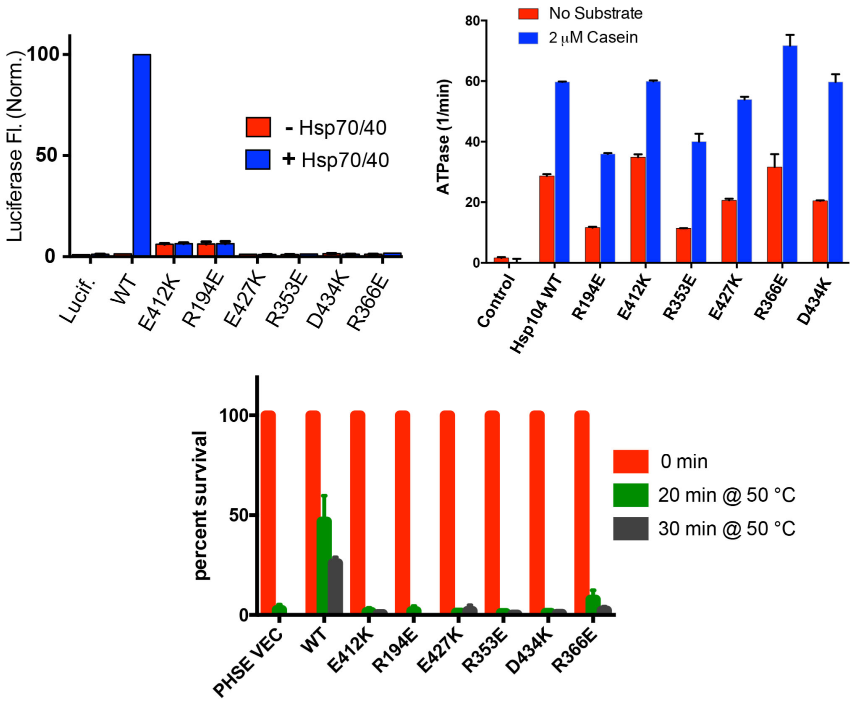

Figure 3-14 Assays to evaluate MD-NBD1 interaction (top, left) Luciferase reactivation measured by fluorescence after incubation with Hsp104 wild type (wt) or indicated mutants in the absence (red) or presence (blue) of anHsp70/40 system. Values are normalized to wt + Hsp70/40 and represent the mean ± SD (*n* = 4). (top, right) ATPase activity of wildtype Hsp104 and L1-NBD1 variants identified in the Hsp104-AMPPNP structure in the absence (red) and presence (blue) of casein (2 μM). Values represent mean±SD (n=2). (bottom) Δhsp104 yeast cells harboring empty pHSEgc vector or the indicated pHSEgc-Hsp104 variant (WT, E412K, R194E, E427K, R535E, D434K, or R366E) were grown to mid-log phase in SD-his. Prior to the 50°C heat treatment, matched cultures were preincubated at 37°C for 30 min. Following treatment at 50°C for 0 min (red bars), 20 min (green bars), or 30 min (black bars) cells were transferred to ice and plated on SD-his. After 2 days at 30°C, survival (%) was quantified. Values represent mean±SD (n=3).

Spiral staircase of pore loops defines the substrate path

Each NBD contains flexible loop regions that harbor the conserved Tyr residues (Tyr 257 for NBD1 and Tyr 662 in NBD2) that bind polypeptide substrates and are required for disaggregation (Lum et al., 2004; Schlieker et al., 2004; Tessarz et al., 2008; Weibezahn et al., 2004). These pore loops, however, are not resolved in the ClpB structure (Lee et al., 2003) and how polypeptides could be actively transferred from protomer to protomer and across the two AAA+ domains has been unclear. By flexible fitting we were able to model pore loop residues for NBD1 (excluding residues 253-258) and NBD2 (excluding residues 660-666) within large lobes of density identified in the channel (Figure 3-15, left). The NBD1 and NBD2 pore loops are separated by 35-40 Å, depending on the protomer, and project toward the channel axis in a staggered, counter clockwise arrangement looking down the N-terminal channel entrance (Figure 3-15, right).

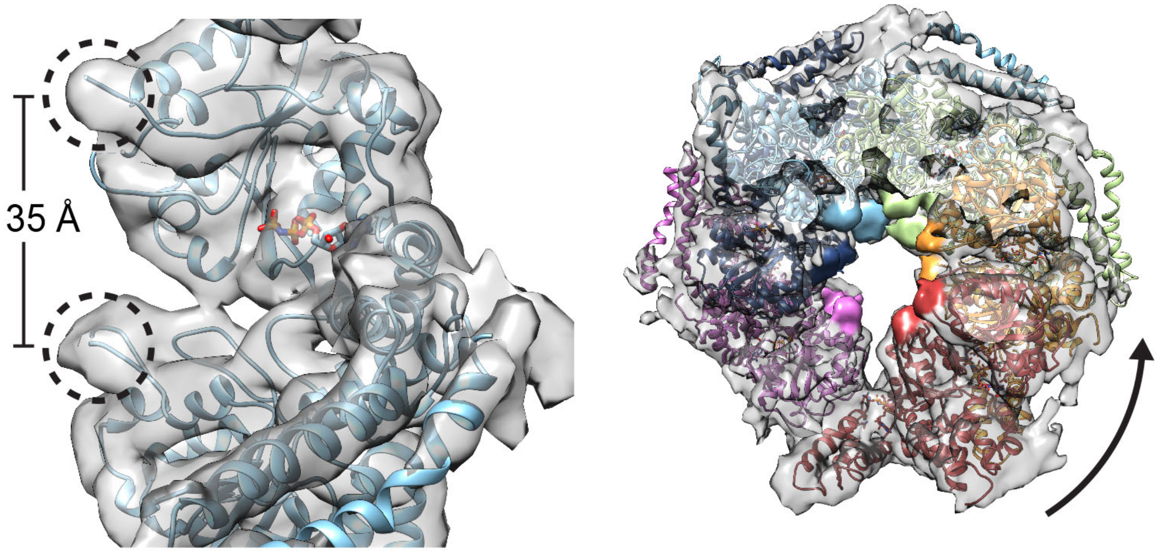

Figure 3-15 Tyrosine pore loops line the central channel (left) Density corresponding to the tyrosine pore loops (circled) for NBD1 and NBD2 is shown for P4. (right) View down the channel from the NBD1 face. The pore-loop densities are colored according to protomer. The arrow indicates a counterclockwise shift between adjacent protomers moving down the channel.

Seen from inside the channel, the NBD1 and NBD2 pore loops form a two-turn spiral staircase (Figure 3-16). The P1-NBD1 pore loop is nearest to the NTD channel cleft and each subsequent loop is 15-20 Å away, moving further into the channel towards the P6-NBD2. The distances between the pore loops vary, with greater separation near the hexamer seam, particularly between P5 and P6, which are separated by 20 Å, reflecting conformational differences in the protomers. Notably, we observe additional lobes of density located beneath the NBD1 pore loops, corresponding to residues 288-298, which could serve as additional substrate binding surfaces via electrostatic interactions.

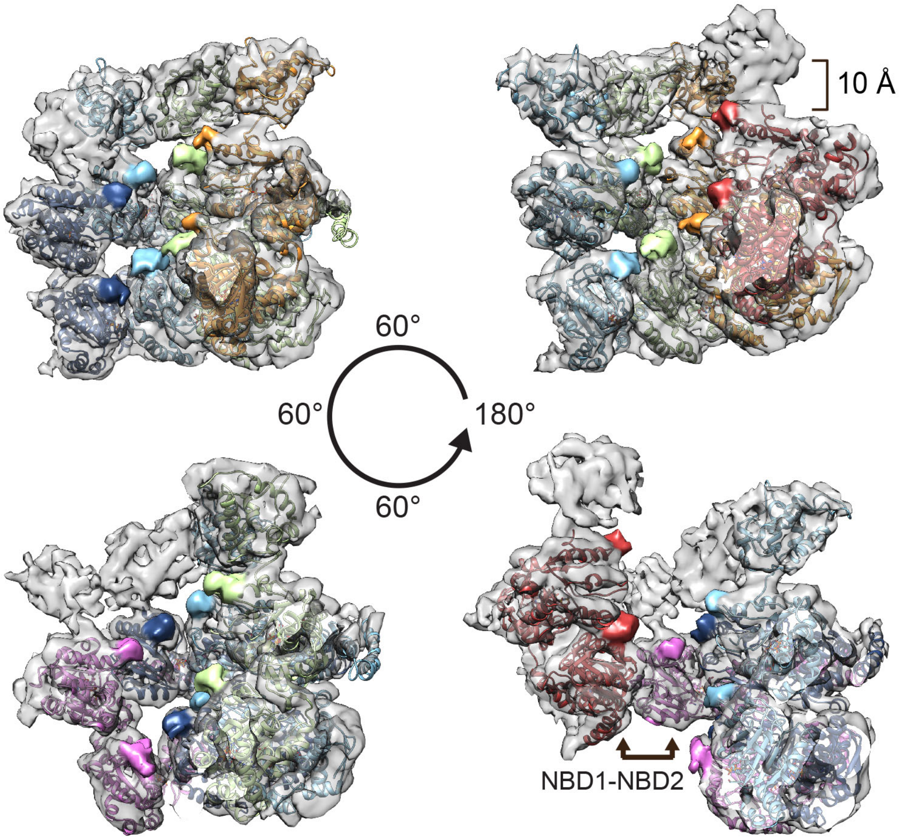

Figure 3-16 Two-turn spiral arrangement of pore loops in the central channel Rotated views from inside channel, showing the two-turn spiral organization of the pore loops and putative P6 NBD1 to P1 NBD2 substrate-transfer site.

Indeed, this corresponding region in ClpA has been shown to interact directly with substrate (Hinnerwisch et al., 2005). The position of NBD1 loops are approximately 10 Å away from the respective NTDs for each protomer, thus substrates could be transferred to the NBD at multiple sites around the channel. Remarkably, the heteromeric NBD1-NBD2 interaction at the hexamer seam positions the respective pore loops 17 Å apart, similar to the other distances, revealing a contiguous substrate transfer pathway between the AAA+ domains.

3.4 Discussion

Achieving a definitive structure of the active Hsp104 hexamer has been a bottleneck to understanding how these conserved AAA+ complexes function as disaggregase machines. Previous cryo-EM structures were critical in revealing the overall hexameric three-tier architecture (Lee et al., 2010, 2007, Wendler et al., 2009, 2007) but were limited in resolution, likely due to available cryo-EM technology, heterogeneity, and imposed symmetry. By utilizing the latest cryo-EM technical advances and acquiring a substantial single particle dataset for exhaustive classification and alignment, we have achieved a structure of Hsp104 that reveals, for the first time, that the hexamer adopts an asymmetric, near-helical architecture that connects the AAA+ domains around the channel. This unprecedented spiral arrangement provides a structural mechanism that explains how cooperative interactions between the protomers and across the AAA+ domains by Hsp104 might drive processive polypeptide translocation (DeSantis et al., 2012; Hattendorf, 2002; Sweeny et al., 2015).

The left-handed helical organization establishes a substrate-binding path that appears optimally organized for transfer from protomer to protomer counter clockwise around the channel thereby achieving directional polypeptide movement from the NTD entrance to the NBD2 exit (Figure 3-16). The NBD1-NBD2 interaction aligns the pore loops, facilitating substrate transfer across the AAA+ domains, and enabling two or more cycles of interaction per protomer. This mechanism is likely necessary for substrates such as structured amyloids that are dependent on high protomer cooperativity and action from both AAA+ domains (DeSantis et al., 2012). Polypeptide threading could occur more stochastically or involve a subset of protomers, such as for disordered, unstructured aggregates, as proposed in previous studies (DeSantis et al., 2012; Doyle et al., 2012). Nonetheless, the staircase arrangement of binding surfaces explains how Hsp104 can cooperatively utilize both AAA+ domains for more powerful unfolding. This is a remarkable extension of unidirectional threading models based on the asymmetric architecture of ClpX (Glynn et al., 2009; Mogk et al., 2015), which exhibits a staggered arrangement of pore loops around its single AAA+ ring. While the translocation step size is unknown for Hsp104, it is expected to be less than 30 Å based on measurements of ClpB (Li et al., 2015), ClpX (Aubin-Tam et al., 2011; Maillard et al., 2011) and ClpA (Olivares et al., 2014). The 15-20 Å distance between pore loops we identify is in agreement, indicating polypeptide translocation occurs by short, stepwise transfer events. Given the homology, we expect related ClpB and other type II Hsp100 family members could adopt a similar spiral architecture as Hsp104. Indeed, the ClpA(Guo et al., 2002) and ClpB (Lee et al., 2003) protomers each form unique right-handed spirals in the crystal. However, both display mechanistic differences: ClpA functions in conjunction with a bound ClpP protease (Alexopoulos et al., 2012), while ClpB is proposed to operate via non-processive translocation events (DeSantis et al., 2012; Li et al., 2015), thus these complexes may adopt different hexamer arrangements in solution.

The asymmetric seam and protomer offset presents a unique architecture that is likely functionally significant. The P1 NTD and NBD1 substrate binding surfaces are at the topmost axial position and accessible due to the 50 Å-wide cleft formed by separation of P1 and P6 NTDs (Figure 3-11, left). Thus, initial substrate engagement could involve preferential interactions with this protomer. The cleft at the hexamer seam opens directly to the P1-NTD and MD, thereby presenting an optimal site for Hsp70 to interact and transfer substrates to the channel (Figure 3-17, left). The interface at the hexamer seam may also play critical roles in the functional plasticity of Hsp104 (Sweeny et al., 2015), facilitating recognition and engagement of different aggregate structures. Finally, given known nucleotide-dependent dynamics of the hexamer (Werbeck et al., 2008), a compelling mechanism is that reorganization of the protomer offset is triggered by substrate binding, Hsp70 interaction or ATP hydrolysis to facilitate translocation (Figure 3-17, right).

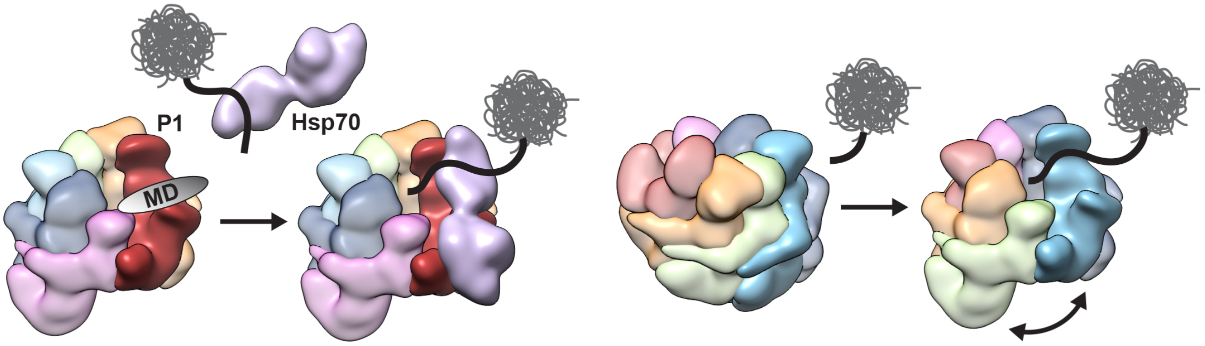

Figure 3-17 Models for cooperative disaggregation and substrate engagement by Hsp104 (left) The hexamer seam and cleft between P1 and P6 presents a channel entrance and an optimal configuration for substrate binding and Hsp70 interaction via the P1 MD. (right) Depiction of protomer rearrangements, triggered by substrate binding, that could result in formation of the hexamer seam at the site of engagement and facilitate polypeptide translocation into the channel.

A number of different MD arrangements have been proposed based on previous low-resolution models (Carroni et al., 2014; Lee et al., 2010, 2007, 2003; Wendler et al., 2007). Our structure reveals a MD conformation in the ATP state and identifies bridging interactions between L1 and L2 and the small and large subdomains of the adjacent protomer, potentially stabilizing the nucleotide pocket for hydrolysis. Identification of potential salt bridge interactions involving R419, E427, and D434 (Figure 4f and Supplementary Fig 4) supports fluorescence resonance energy transfer experiments with ClpB that identify contact between L1 and the adjacent NBD1 (Oguchi et al., 2012) and mutagenesis studies showing Hsp104-R419M is functionally deficient (Wendler et al., 2007). DnaK/Hsp70 binds the opposite end of the MD coil-coil at helices L2 and L3 to deliver substrates and promote disaggregation (Haslberger et al., 2007; Lee et al., 2013; Rosenzweig et al., 2013). The MD L1-L2 interactions may serve as control elements for allosteric activation by DnaK/Hsp70 during substrate delivery (Oguchi et al., 2012; Seyffer et al., 2012). Indeed, mutations in L1 eliminate collaboration with Hsp70 (DeSantis et al., 2014) and enable disaggregation to occur independently of Hsp70 and Hsp40 (Jackrel and Shorter, 2014).

In addition to our results here, a number of recent cryo-EM structures of AAA+ complexes, including, in particular, the Pex1-Pex6 (Blok et al., 2015) and NSF (Zhao et al., 2015). double AAA+ ring complexes, have identified asymmetric states. Together this work is beginning to reveal that AAA+ proteins in general operate via large asymmetries in the protomer organization and hydrolysis mechanisms (Glynn et al., 2009). The Hsp104-AMPPNP structure determined is in a unique conformation which has both AAA+ domains arranged in a two-turn spiral involving interaction between the different AAA+ (NBD1-NBD2) domains. VAT is the only other structure which has shown a similar (although opposite handedness) spiral arrangement (CITE **). Both Pex1-Pex6 and NSF complexes exhibit a planar, symmetric NBD1 ring that is flexibly connected to an asymmetric NBD2 ring. In Hsp104, the orientation between the two AAA+ domains within a protomer is relatively consistent around the ring except for the hexamer seam. At this position, conformational differences between P6 and P1, including a 20° rotation of NBD2 relative to NBD1, enable the NBD1-NBD2 interaction that maintains a closed hexamer ring despite the substantial, 100° rotation around the channel axis (compared to ~50° for the other protomers) (Figure 3a). In addition we identified density corresponding to a bound nucleotide for 9 out of 12 ATP binding sites, while two sites show partial occupancy and one site is empty. This finding is consistent with previous estimates for nucleotide occupancy of 8-12 nucleotides for ClpB hexamers (Carroni et al., 2014; Lin and Lucius, 2016), and supports an asymmetric hydrolysis mechanism. Intriguingly, the NBD1s overall have reduced nucleotide occupancy compared to the NBD2s, which are completely bound. Similarly, kinetic studies determined that the NBD1 has a reduced ATP affinity but much higher catalytic activity compared to the NBD2 (Hattendorf, 2002), supporting distinct functions during disaggregation. Nonetheless, with this overall high nucleotide occupancy together with the spiral architecture, the power of the two AAA+ domains appears to be uniquely coupled for Hsp104 compared to other AAA+ complexes and is perhaps reflective of the mechanical force required for disaggregation. Additional studies will be critical in elucidating conformational changes associated with ATP hydrolysis-dependent translocation events to understand the mechanical changes that drive disaggregation.

3.5 Methods

Protein Purification, ATPase and Luciferase Reactivation Assay

Wild type Hsp104 was purified as described (Jackrel and Shorter, 2014). Hexameric Hsp104 (0.042 μM) was incubated with ATP (1 mM) at 25°C before monitoring the release of inorganic phosphate over 5 minutes using a malachite green kit (Innova). ATPase turnover was measured at a maximum rate of ~11min, which corresponded to a functional, ATPase-active complex. Disaggregase function was measured by a luciferase reactivation assay as previously described (DeSantis et al. 2012). Aggregated luciferase (50nM) was incubated with Hsp104 (0.167μM hexamer) in the presence of equimolar Hsc70 and Hdj2 (Enzo Life Sciences) plus ATP (5.1 mM) and an ATP regeneration system (1 mM creatine phosphate, 0.25μM creatine kinase) for 90 min at 25°C.

Cryo Sample Preparation and Data Collection

WT Hsp104 (8.5 mg/mL) was incubated with AMP-PNP (5 mM) for 20 minutes at 25°C. Samples were diluted to 0.7 mg/ml in 40 mM HEPES pH=7.5, 40 mM NaCl, 10 mM $MgCl_2$, 1 mM DTT, 5mM AMP-PNP and 3.5 μl was applied to plasma cleaned C-Flat 2/2 holey carbon grids (Protochips). Vitrification was performed using a Vitrobot (FEI Company) and samples were blotted for 1.5-2 seconds prior to plunge freezing in liquid ethane. Of note, during initial attempts at imaging Hsp104 routinely dissociated into monomers and substantial optimization of buffer conditions, sample concentration and freezing conditions was required to achieve proper ice thickness and a homogeneous spread of hexameric particles. Furthermore, the presence of DDM detergent was tested to increase the angular distribution but resulted in dissociation of the hexamer at a variety of concentrations (data not shown).

Samples were imaged using a Titan Krios TEM (FEI Inc.) operated at 300 kV. Images were recorded on a Gatan K2 Summit direct electron detector operated in counted mode at 50,000X nominal magnification corresponding to a calibrated to 1.00

Å/pixel. Dose fractionated imaging was performed by semi-automated collection methods using UCSF Image 4 (Li et al. 2015) with a defocus range of 1.5-3 um. Total exposure time was 8 seconds with 0.2 second frames with a cumulative dose of ~45 e^- per $Å^2$ for 40 frames. Motion corrected frames were summed with the first two frames excluded, and the FFT was visually inspected for sufficient Thon rings prior to additional processing (Li et al. 2013).

Image Processing and 3D Refinement

All micrographs were CTF corrected using CTFFIND4 (Rohou and Grigorieff, 2015) and poorly corrected micrographs were removed following visual inspection of the FFT and CTF estimation. An initial single particle dataset was achieved by manual particle picking using e2boxer (EMAN2) (Tang et al., 2007), which yielded ~50,000 particles from 1731 micrographs. Well-populated reference-free 2D class averages, determined with Relion (Scheres, 2012), were used for templated automated particle picking with the Template Picker in Appion (Lander et al., 2009) to achieve a ~200,000 single particles dataset from 1930 micrographs. The total dataset of ~250,000 particles was initially sorted following 2D classification by removing particles images from poorly resolved class averages, resulting in a total dataset of ~190,000 particles. All subsequent 3D processing was performed using Relion[7] with no symmetry imposed based on the asymmetric arrangement identified in the 2D class averages (Figure 1b). A previously determined cryo-EM 3D reconstruction of ATP–Hsp104 (EMDB: 1600) (Wendler et al., 2009), low pass filtered to 50Å, served as an initial model for 3D classification and refinement. The 8 models generated from 3D classification appeared homogenous (data not shown), therefore, the full dataset was used for initial gold-standard 3D refinement. The resulting 3D model refined to an estimated resolution of 7.5 Å (data not shown). Z-score parameters based on this refinement, defined in Relion, were written for the data set and the dataset was trimmed to the highest Z-score for 160,000 particles. Additional 3D refinement was performed with this trimmed data set and resulted in a final model with an estimated resolution of 6.54 Å using the FSC = 0.143 FSC criterion (Supplementary Fig 1e). Additional trimming based on the Z-score showed no improvement and extensive 3D classification and refinement of individual classes as well as local refinement using 3D masking was tested and did not yield improvements in the map. Thus, the resolution is likely limited by flexibility of multiple regions in the complex (Supplementary 1h) and moderate preferred orientation (Supplementary Fig. 1f). For the final sharpened map, the “Post-processing” procedure was used to generate a soft mask for the two half maps prior to FSC estimation, which was determined to be 5.64 Å (Supplementary Fig 1e). Automated B-factor sharpening was carried on the combined map with an estimated -188 B-factor. The local resolution was estimated using ResMap on the unsharpened map (Kucukelbir et al., 2013).

Domain Modeling

This final sharpened map was used for all rigid body docking and flexible fitting of atomic structures. Rigid body fitting was performed with UCSF Chimera (Petterson et al. 2004). Initial comparisons were performed by fitting individual protomers with the protomers in *T. thermophilus* ClpB crystal structure (PBD_ID=1qvr), but resulted in a low cross correlation value and clear conformational differences were apparent.

Individual subdomains (NTD, NBD1 large, NBD1 small, MD (residues 409-467), NBD2 large, NBD2 small) from the crystal structure were then docked as rigid bodies and resulted in an improved fit, however a number of AAA+ domain helices did not align with the density. Therefore, to more accurately interrupt the map, a homology model of Hsp104 (residues 6-857) was determined from the ClpB structure (residues 4-850) using SWISS_MODEL (Biasini et al., 2014) followed by rigid body docking the subdomains. Flexible fitting of the protomer sub volumes and the entire hexamer map was then performed using phenix.real_space_refine (Afonine et al., 2012) using backbone carbons of our homology model. The real space refinement was implemented at 6σ, resolution 6Å and the cross correlation improved from 0.72 to 0.9 for the complete map after refinement. To visualize whether density is present in the nucleotide pockets difference maps were generated by subtracting a simulated density map of the Hsp104 homology model without AMPPNP from the final refined map and shown at 5σ (Supplemental Fig. 2b). Based on the difference map, clear density was observed at 9 sites and partial density at two sites, therefore AMPPNP was included in the model at these sites and docked based on the ClpB structure. Modeling the P2-P4 NTDs was facilitated by localization of the well-defined NTD-NBD1 connecting density as well as regions that could be attributed to the larger A1 and A6 helices that make up the hydrophobic substrate-binding cleft (Rosenzweig et al., 2015). Manual modeling of the tyrosine loop regions was performed in COOT (Emsley et al., 2010). Loop regions within the NBD1 domain (248-260,287-300) were modeled by backbone positioning within the density; residues 251-259, 292-297 could not be modeled in the density. Of note, a major shift was required to model the NBD2 tyrosine loop (656-669), which showed a distinct curve away from the flanking helices. Similarly, the most central portion of the loop lacked density and was not modeled (659-666). All 3D reconstruction figures were generated using UCSF Chimera (Pettersen et al., 2004).

ATPase Assay of MD-NBD1 Mutants

Hsp104 (0.25μM monomer) WT or mutant was equilibrated in Luciferase Refolding Buffer (LRB: 25 mM HEPES-KOH, pH 7.4, 150 mM KAOc, 10 mM MgAOc, 10 mM DTT) for 15 min on ice and then incubated for 5 min at 25°C in the presence of ATP (1 mM) plus or minus casein (2μM). ATPase activity was assessed by the release of inorganic phosphate, which was determined using a malachite green phosphate detection kit (Innova) (Fig. S8E)

Luciferase Reactivation Assay

To generate aggregated luciferase, firefly luciferase (50 μM) in LRB plus 8 M urea was incubated at 30°C for 30 min. The sample was then rapidly diluted 100-fold into LRB. Aliquots were snap frozen in liquid N_2 and stored at −80°C until use. Aggregated luciferase (50 nM) was incubated with Hsp104 (1 μM monomer), Hsc70 (0.167 μM) and Hdj2 (0.167 μM) plus ATP (5 mM) and an ATP regeneration system (10 mM creatine phosphate, 0.25μM creatine kinase) for 90 min at 25°C. At the end of the reaction, luciferase activity was assessed with a luciferase assay system (Promega). Recovered luminescence was monitored using a Tecan Infinite M1000 plate reader (Fig. 5D).

Induced Thermotolerance Assay

W303aΔ*hsp104* (MATa, can1–100, his3–11,15, leu2–3,112, trp1–1, ura3–1, ade2–1, hsp104:kanMX4) yeast cells were transformed with a centromeric plasmid, pHSEgc, encoding Hsp104 or indicated variant under the control of the HSP104 promoter. The empty pHSEgc vector served as a negative control. Transformed yeast were grown at 30°C in S-Dextrose-His (SD-His) media to an optical density of OD_{600}=0.6. Cells were incubated at 37°C for 30 min to induce the expression of Hsp104 or the indicated variant and then transferred to 50°C for 0, 20 min or 30 min heat shock. Cells were then transferred to ice for 2 min. To evaluate viability, cells were then diluted 1,000-fold in ice-cold SD-His and plated on SD-His. Colonies were counted using an aCOLyte automated colony counter (Synbiosis) after growth at 30°C for 2 days (Fig. S8F). Immunoblot analysis showed that each Hsp104 variant was expressed at a similar level under equivalent conditions.

3.6 Acknowledgements

Majority of the data from this chapter was published in “Spiral architecture of the Hsp104 disaggregase reveals the basis for polypeptide translocation” which was printed in *Nature Structure and Molecular Biology*, August 2016. Data from ‘Mutagenesis of MD-NBD1 Contacts’ section was printed as part of “Ratchet-like polypeptide translocation mechanism of the AAA+ disaggregase Hsp104” in *Science*, June 2017. This highly collaborative project would not have been successful without the contributions which follow. Adam Yokom performed cryo-EM data collection, processing, atomic modeling and wrote the manuscript. Stephanie Gates performed

cryo-EM data collection and analysis; Meredith Jackrel purified proteins, performed biochemical analysis and edited the manuscript; Korrie Mack performed biochemical analysis; Min Su supervised cryo-EM data collection; James Shorter and Daniel Southworth aided in the design experiments and edited the manuscript

3.7 Accession Codes

The cryo-EM density map (EMD-8267) has been deposited in the Electron Microscopy Data Bank, and the molecular model (PDB 5KNE) has been deposited in the Protein Data Bank.

3.8 References

Abbas-Terki, T., Donze, O., Briand, P.-A., Picard, D., 2001. Hsp104 Interacts with Hsp90 Cochaperones in Respiring Yeast. Mol. Cell. Biol. 21, 7569–7575. doi:10.1128/MCB.21.22.7569-7575.2001

Afonine, P.V., Grosse-Kunstleve, R.W., Echols, N., Headd, J.J., Moriarty, N.W., Mustyakimov, M., Terwilliger, T.C., Urzhumtsev, A., Zwart, P.H., Adams, P.D., 2012. Towards automated crystallographic structure refinement with *phenix.refine*. Acta Crystallogr. D Biol. Crystallogr. 68, 352–367. doi:10.1107/S0907444912001308

Aguado, A., Fernández-Higuero, J.A., Cabrera, Y., Moro, F., Muga, A., 2015. ClpB dynamics is driven by its ATPase cycle and regulated by the DnaK system and substrate proteins. Biochem. J. 466, 561–570. doi:10.1042/BJ20141390

Alexopoulos, J.A., Guarné, A., Ortega, J., 2012. ClpP: A structurally dynamic protease regulated by AAA+ proteins. J. Struct. Biol. 179, 202–210. doi:10.1016/j.jsb.2012.05.003

Aubin-Tam, M.-E., Olivares, A.O., Sauer, R.T., Baker, T.A., Lang, M.J., 2011. Single-Molecule Protein Unfolding and Translocation by an ATP-Fueled Proteolytic Machine. Cell 145, 257–267. doi:10.1016/j.cell.2011.03.036

Biasini, M., Bienert, S., Waterhouse, A., Arnold, K., Studer, G., Schmidt, T., Kiefer, F., Cassarino, T.G., Bertoni, M., Bordoli, L., Schwede, T., 2014. SWISS-MODEL:

modelling protein tertiary and quaternary structure using evolutionary information. Nucleic Acids Res. 42, W252–W258. doi:10.1093/nar/gku340

Blok, N.B., Tan, D., Wang, R.Y.-R., Penczek, P.A., Baker, D., DiMaio, F., Rapoport, T.A., Walz, T., 2015. Unique double-ring structure of the peroxisomal Pex1/Pex6 ATPase complex revealed by cryo-electron microscopy. Proc. Natl. Acad. Sci. 112, E4017–E4025. doi:10.1073/pnas.1500257112

Bösl, B., Grimminger, V., Walter, S., 2005. Substrate Binding to the Molecular Chaperone Hsp104 and Its Regulation by Nucleotides. J. Biol. Chem. 280, 38170–38176. doi:10.1074/jbc.M506149200

Carroni, M., Kummer, E., Oguchi, Y., Wendler, P., Clare, D.K., Sinning, I., Kopp, J., Mogk, A., Bukau, B., Saibil, H.R., 2014. Head-to-tail interactions of the coiled-coil domains regulate ClpB activity and cooperation with Hsp70 in protein disaggregation. eLife 3. doi:10.7554/eLife.02481

Chernoff, Y.O., Lindquist, S.L., Ono, B., Inge-Vechtomov, S.G., Liebman, S.W., 1995. Role of the chaperone protein Hsp104 in propagation of the yeast prion-like factor [psi+]. Science 268, 880–884.

Cushman-Nick, M., Bonini, N.M., Shorter, J., 2013. Hsp104 Suppresses Polyglutamine-Induced Degeneration Post Onset in a Drosophila MJD/SCA3 Model. PLoS Genet. 9, e1003781. doi:10.1371/journal.pgen.1003781

DeSantis, M.E., Leung, E.H., Sweeny, E.A., Jackrel, M.E., Cushman-Nick, M., Neuhaus-Follini, A., Vashist, S., Sochor, M.A., Knight, M.N., Shorter, J., 2012. Operational Plasticity Enables Hsp104 to Disaggregate Diverse Amyloid and Nonamyloid Clients. Cell 151, 778–793. doi:10.1016/j.cell.2012.09.038

DeSantis, M.E., Sweeny, E.A., Snead, D., Leung, E.H., Go, M.S., Gupta, K., Wendler, P., Shorter, J., 2014. Conserved Distal Loop Residues in the Hsp104 and ClpB Middle Domain Contact Nucleotide-binding Domain 2 and Enable Hsp70-dependent Protein Disaggregation. J. Biol. Chem. 289, 848–867. doi:10.1074/jbc.M113.520759

Doyle, S.M., Hoskins, J.R., Wickner, S., 2012. DnaK Chaperone-dependent Disaggregation by Caseinolytic Peptidase B (ClpB) Mutants Reveals Functional Overlap in the N-terminal Domain and Nucleotide-binding Domain-1 Pore Tyrosine. J. Biol. Chem. 287, 28470–28479. doi:10.1074/jbc.M112.383091

Dulle, J.E., Stein, K.C., True, H.L., 2014. Regulation of the Hsp104 Middle Domain Activity Is Critical for Yeast Prion Propagation. PLoS ONE 9, e87521. doi:10.1371/journal.pone.0087521

Emsley, P., Lohkamp, B., Scott, W.G., Cowtan, K., 2010. Features and development of *Coot*. Acta Crystallogr. D Biol. Crystallogr. 66, 486–501. doi:10.1107/S0907444910007493

Glover, J.R., Lindquist, S., 1998. Hsp104, Hsp70, and Hsp40: a novel chaperone system that rescues previously aggregated proteins. Cell 94, 73–82.

Glynn, S.E., Martin, A., Nager, A.R., Baker, T.A., Sauer, R.T., 2009. Structures of Asymmetric ClpX Hexamers Reveal Nucleotide-Dependent Motions in a AAA+ Protein-Unfolding Machine. Cell 139, 744–756. doi:10.1016/j.cell.2009.09.034

Guo, F., Maurizi, M.R., Esser, L., Xia, D., 2002. Crystal Structure of ClpA, an Hsp100 Chaperone and Regulator of ClpAP Protease. J. Biol. Chem. 277, 46743–46752. doi:10.1074/jbc.M207796200

Haslberger, T., Weibezahn, J., Zahn, R., Lee, S., Tsai, F.T.F., Bukau, B., Mogk, A., 2007. M Domains Couple the ClpB Threading Motor with the DnaK Chaperone Activity. Mol. Cell 25, 247–260. doi:10.1016/j.molcel.2006.11.008

Hattendorf, D.A., 2002. Cooperative kinetics of both Hsp104 ATPase domains and interdomain communication revealed by AAA sensor-1 mutants. EMBO J. 21, 12–21. doi:10.1093/emboj/21.1.12

Hinnerwisch, J., Fenton, W.A., Furtak, K.J., Farr, G.W., Horwich, A.L., 2005. Loops in the Central Channel of ClpA Chaperone Mediate Protein Binding, Unfolding, and Translocation. Cell 121, 1029–1041. doi:10.1016/j.cell.2005.04.012

Jackrel, M.E., Shorter, J., 2014. Potentiated Hsp104 variants suppress toxicity of diverse neurodegenerative disease-linked proteins. Dis. Model. Mech. 7, 1175–1184. doi:10.1242/dmm.016113

Kedzierska, S., Akoev, V., Barnett, M.E., Zolkiewski, M., 2003. Structure and Function of the Middle Domain of ClpB from *Escherichia coli* †. Biochemistry (Mosc.) 42, 14242–14248. doi:10.1021/bi035573d

Kucukelbir, A., Sigworth, F.J., Tagare, H.D., 2013. Quantifying the local resolution of cryo-EM density maps. Nat. Methods 11, 63–65. doi:10.1038/nmeth.2727

Lander, G.C., Stagg, S.M., Voss, N.R., Cheng, A., Fellmann, D., Pulokas, J., Yoshioka, C., Irving, C., Mulder, A., Lau, P.-W., Lyumkis, D., Potter, C.S., Carragher, B., 2009. Appion: an integrated, database-driven pipeline to facilitate EM image processing. J. Struct. Biol. 166, 95–102.

Lee, J., Kim, J.-H., Biter, A.B., Sielaff, B., Lee, S., Tsai, F.T.F., 2013. Heat shock protein (Hsp) 70 is an activator of the Hsp104 motor. Proc. Natl. Acad. Sci. 110, 8513–8518. doi:10.1073/pnas.1217988110

Lee, S., Choi, J.-M., Tsai, F.T.F., 2007. Visualizing the ATPase Cycle in a Protein Disaggregating Machine: Structural Basis for Substrate Binding by ClpB. Mol. Cell 25, 261–271. doi:10.1016/j.molcel.2007.01.002

Lee, S., Sielaff, B., Lee, J., Tsai, F.T.F., 2010. CryoEM structure of Hsp104 and its mechanistic implication for protein disaggregation. Proc. Natl. Acad. Sci. 107, 8135–8140. doi:10.1073/pnas.1003572107

Lee, S., Sowa, M.E., Watanabe, Y., Sigler, P.B., Chiu, W., Yoshida, M., Tsai, F.T.F., 2003. The structure of ClpB: a molecular chaperone that rescues proteins from an aggregated state. Cell 115, 229–240.

Li, T., Weaver, C.L., Lin, J., Duran, E.C., Miller, J.M., Lucius, A.L., 2015. *Escherichia coli* ClpB is a non-processive polypeptide translocase. Biochem. J. 470, 39–52. doi:10.1042/BJ20141457

Lin, J., Lucius, A.L., 2016. Examination of ClpB Quaternary Structure and Linkage to Nucleotide Binding. Biochemistry (Mosc.) 55, 1758–1771. doi:10.1021/acs.biochem.6b00122

Lo Bianco, C., Shorter, J., Régulier, E., Lashuel, H., Iwatsubo, T., Lindquist, S., Aebischer, P., 2008. Hsp104 antagonizes α-synuclein aggregation and reduces dopaminergic degeneration in a rat model of Parkinson disease. J. Clin. Invest. 118, 3087–3097. doi:10.1172/JCI35781

Lum, R., Tkach, J.M., Vierling, E., Glover, J.R., 2004. Evidence for an Unfolding/Threading Mechanism for Protein Disaggregation by *Saccharomyces cerevisiae* Hsp104. J. Biol. Chem. 279, 29139–29146. doi:10.1074/jbc.M403777200

Mackay, R.G., Helsen, C.W., Tkach, J.M., Glover, J.R., 2008. The C-terminal Extension of *Saccharomyces cerevisiae* Hsp104 Plays a Role in Oligomer Assembly †. Biochemistry (Mosc.) 47, 1918–1927. doi:10.1021/bi701714s

Maillard, R.A., Chistol, G., Sen, M., Righini, M., Tan, J., Kaiser, C.M., Hodges, C., Martin, A., Bustamante, C., 2011. ClpX(P) Generates Mechanical Force to Unfold and Translocate Its Protein Substrates. Cell 145, 459–469. doi:10.1016/j.cell.2011.04.010

Mogk, A., Kummer, E., Bukau, B., 2015. Cooperation of Hsp70 and Hsp100 chaperone machines in protein disaggregation. Front. Mol. Biosci. 2, 22. doi:10.3389/fmolb.2015.00022

Mogk, A., Schlieker, C., Strub, C., Rist, W., Weibezahn, J., Bukau, B., 2003. Roles of Individual Domains and Conserved Motifs of the AAA+ Chaperone ClpB in

Oligomerization, ATP Hydrolysis, and Chaperone Activity. J. Biol. Chem. 278, 17615–17624. doi:10.1074/jbc.M209686200

Moriyama, H., Edskes, H.K., Wickner, R.B., 2000. [URE3] prion propagation in Saccharomyces cerevisiae: requirement for chaperone Hsp104 and curing by overexpressed chaperone Ydj1p. Mol. Cell. Biol. 20, 8916–8922.

Motohashi, K., Watanabe, Y., Yohda, M., Yoshida, M., 1999. Heat-inactivated proteins are rescued by the DnaK.J-GrpE set and ClpB chaperones. Proc. Natl. Acad. Sci. U. S. A. 96, 7184–7189.

Oguchi, Y., Kummer, E., Seyffer, F., Berynskyy, M., Anstett, B., Zahn, R., Wade, R.C., Mogk, A., Bukau, B., 2012. A tightly regulated molecular toggle controls AAA+ disaggregase. Nat. Struct. Mol. Biol. 19, 1338–1346. doi:10.1038/nsmb.2441

Olivares, A.O., Nager, A.R., Iosefson, O., Sauer, R.T., Baker, T.A., 2014. Mechanochemical basis of protein degradation by a double-ring AAA+ machine. Nat. Struct. Mol. Biol. 21, 871–875. doi:10.1038/nsmb.2885

Parsell, D.A., Kowal, A.S., Lindquist, S., 1994a. Saccharomyces cerevisiae Hsp104 protein. Purification and characterization of ATP-induced structural changes. J. Biol. Chem. 269, 4480–4487.

Parsell, D.A., Kowal, A.S., Singer, M.A., Lindquist, S., 1994b. Protein disaggregation mediated by heat-shock protein Hsp104. Nature 372, 475–478. doi:10.1038/372475a0

Pettersen, E.F., Goddard, T.D., Huang, C.C., Couch, G.S., Greenblatt, D.M., Meng, E.C., Ferrin, T.E., 2004. UCSF Chimera?A visualization system for exploratory research and analysis. J. Comput. Chem. 25, 1605–1612. doi:10.1002/jcc.20084

Rohou, A., Grigorieff, N., 2015. CTFFIND4: Fast and accurate defocus estimation from electron micrographs. J. Struct. Biol. 192, 216–221. doi:10.1016/j.jsb.2015.08.008

Rosenzweig, R., Farber, P., Velyvis, A., Rennella, E., Latham, M.P., Kay, L.E., 2015. ClpB N-terminal domain plays a regulatory role in protein disaggregation. Proc. Natl. Acad. Sci. 112, E6872–E6881. doi:10.1073/pnas.1512783112

Rosenzweig, R., Moradi, S., Zarrine-Afsar, A., Glover, J.R., Kay, L.E., 2013. Unraveling the Mechanism of Protein Disaggregation Through a ClpB-DnaK Interaction. Science 339, 1080–1083. doi:10.1126/science.1233066

Sanchez, Y., Lindquist, S.L., 1990. HSP104 required for induced thermotolerance. Science 248, 1112–1115.

Scheres, S.H.W., 2012. RELION: Implementation of a Bayesian approach to cryo-EM structure determination. J. Struct. Biol. 180, 519–530. doi:10.1016/j.jsb.2012.09.006

Schlieker, C., Weibezahn, J., Patzelt, H., Tessarz, P., Strub, C., Zeth, K., Erbse, A., Schneider-Mergener, J., Chin, J.W., Schultz, P.G., Bukau, B., Mogk, A., 2004. Substrate recognition by the AAA+ chaperone ClpB. Nat. Struct. Mol. Biol. 11, 607–615. doi:10.1038/nsmb787

Seyffer, F., Kummer, E., Oguchi, Y., Winkler, J., Kumar, M., Zahn, R., Sourjik, V., Bukau, B., Mogk, A., 2012. Hsp70 proteins bind Hsp100 regulatory M domains to activate AAA+ disaggregase at aggregate surfaces. Nat. Struct. Mol. Biol. 19, 1347–1355. doi:10.1038/nsmb.2442

Shorter, J., 2004. Hsp104 Catalyzes Formation and Elimination of Self-Replicating Sup35 Prion Conformers. Science 304, 1793–1797. doi:10.1126/science.1098007

Sweeny, E.A., Jackrel, M.E., Go, M.S., Sochor, M.A., Razzo, B.M., DeSantis, M.E., Gupta, K., Shorter, J., 2015. The Hsp104 N-Terminal Domain Enables Disaggregase Plasticity and Potentiation. Mol. Cell 57, 836–849. doi:10.1016/j.molcel.2014.12.021

Tang, G., Peng, L., Baldwin, P.R., Mann, D.S., Jiang, W., Rees, I., Ludtke, S.J., 2007. EMAN2: An extensible image processing suite for electron microscopy. J. Struct. Biol. 157, 38–46. doi:10.1016/j.jsb.2006.05.009

Tessarz, P., Mogk, A., Bukau, B., 2008. Substrate threading through the central pore of the Hsp104 chaperone as a common mechanism for protein disaggregation and prion propagation. Mol. Microbiol. 68, 87–97. doi:10.1111/j.1365-2958.2008.06135.x

Weibezahn, J., Tessarz, P., Schlieker, C., Zahn, R., Maglica, Z., Lee, S., Zentgraf, H., Weber-Ban, E.U., Dougan, D.A., Tsai, F.T.F., Mogk, A., Bukau, B., 2004. Thermotolerance Requires Refolding of Aggregated Proteins by Substrate Translocation through the Central Pore of ClpB. Cell 119, 653–665. doi:10.1016/j.cell.2004.11.027

Wendler, P., Shorter, J., Plisson, C., Cashikar, A.G., Lindquist, S., Saibil, H.R., 2007. Atypical AAA+ Subunit Packing Creates an Expanded Cavity for Disaggregation by the Protein-Remodeling Factor Hsp104. Cell 131, 1366–1377. doi:10.1016/j.cell.2007.10.047

Wendler, P., Shorter, J., Snead, D., Plisson, C., Clare, D.K., Lindquist, S., Saibil, H.R., 2009. Motor Mechanism for Protein Threading through Hsp104. Mol. Cell 34, 81–92. doi:10.1016/j.molcel.2009.02.026

Werbeck, N.D., Schlee, S., Reinstein, J., 2008. Coupling and Dynamics of Subunits in the Hexameric AAA+ Chaperone ClpB. J. Mol. Biol. 378, 178–190. doi:10.1016/j.jmb.2008.02.026

Zhao, M., Wu, S., Zhou, Q., Vivona, S., Cipriano, D.J., Cheng, Y., Brunger, A.T., 2015. Mechanistic insights into the recycling machine of the SNARE complex. Nature 518, 61–67. doi:10.1038/nature14148

Chapter 4

Ratchet-like polypeptide translocation mechanism of the AAA+ disaggregase Hsp104[1]

4.1 Abstract:

Hsp100 polypeptide translocases are conserved AAA+ machines that maintain proteostasis by unfolding aberrant and toxic proteins for refolding or proteolytic degradation. The Hsp104 disaggregase from *S. cerevisiae* solubilizes stress-induced amorphous aggregates and amyloid. The structural basis for substrate recognition and translocation is unknown. Using a model substrate (casein), we report cryo-EM structures at near-atomic resolution of Hsp104 in different translocation states. Substrate interactions are mediated by conserved, pore-loop tyrosines that contact an 80 Å-long unfolded polypeptide along the axial channel. Two protomers undergo a ratchet-like conformational change that advances pore-loop-substrate interactions by two-amino acids. These changes are coupled to activation of specific ATPase sites and, when transmitted around the hexamer, reveal a processive rotary translocation mechanism and a remarkable structural plasticity of Hsp104-catalyzed disaggregation.

---

[1] Data included in this chapter were published in

Gates, S.N.*, **Yokom, A.L.***, Lin, J., Jackrel, M.E., Rizo, A.N., Kendsersky, N.M., Buell, C.E., Sweeny, E.A., Mack, K.L., Chuang, E., Torrente, M.P., Su, M., Shorter, J., Southworth, D.R., 2017. Ratchet-like polypeptide translocation mechanism of the AAA+ disaggregase Hsp104. Science. doi:10.1126/science.aan1052 *Authors contributed equally

4.2 Introduction

Hsp100 disaggregases are highly conserved stress responders that unfold and solubilize protein aggregates (Olivares et al., 2014; Sweeny and Shorter, 2016) . They are AAA+ (ATPases Associated with diverse cellular Activities) proteins that form hexameric rings, which couple ATP hydrolysis to polypeptide translocation through a central channel(Olivares et al., 2014; Sweeny and Shorter, 2016). *S. cerevisiae* Hsp104 is powered by two distinct AAA+ domains per protomer and collaborates with the Hsp70 system to disaggregate and refold amorphous aggregates and amyloids such as Sup35 prions, thereby promoting stress tolerance and prion propagation(Sweeny and Shorter, 2016).

Cooperative ATP hydrolysis by nucleotide-binding domains (NBD1 and NBD2) of Hsp104 requires conserved Walker A and B motifs, ‘sensor’ residues, and an Arg finger from the adjacent protomer (Erzberger and Berger, 2006; Sweeny and Shorter, 2016)s. The coiled-coil middle domain (MD) of Hsp104 mediates Hsp70 interactions and allosteric functions during hydrolysis and disaggregation (Jackrel and Shorter, 2014; Lee et al., 2013; Oguchi et al., 2012). Conserved substrate-binding “pore loops” in the NBDs line the axial channel and contain essential Tyr residues that mechanically couple hydrolysis to translocation (Lum et al., 2004; Tessarz et al., 2008). A recent structure of Hsp104 bound to the nonhydrolysable ATP analog, AMPPNP, identifies an “open”, spiral conformation with a ~30 Å-wide channel and an unusual heteromeric NBD1-NBD2 interaction that forms a flexible seam (Yokom et al., 2016). High-resolution structures of the active hexamer have remained elusive and it is unknown how hydrolysis and conformational changes power disaggregation.

Here, we establish how Hsp104 binds and mechanically translocates substrates. Using the slowly hydrolysable ATP analog, ATPγS (Doyle et al., 2007) and the substrate casein we determined Hsp104 structures to ~4.0 Å by cryo-EM. We identify pore-loop-substrate contacts and a rotary translocation mechanism involving a ratchet-like change that advances interactions along the substrate polypeptide by two amino acids. NBD1-ATP hydrolysis and substrate binding triggers a massive open to closed conformational change in the hexamer, thereby coupling substrate engagement and release to processive disaggregation.

4.3 Results

Substrate-Bound Architecture of Hsp104

To capture the substrate-bound state of Hsp104, binding was assessed via fluorescence polarization (FP) using FITC-labeled casein, a model substrate that is actively translocated (Jackrel et al., 2014; Tessarz et al., 2008). High-affinity interactions (K_d ~ 20nM) between Hsp104 and casein were identified in the presence of ATPγS but not ATP, AMPPNP, or ADP (Figure 4-1, top left). Stable complex was formed and analyzed via size exclusion chromatography (Figure 3-1, top right). This confirmed the substrate binding FP assay where only ATPγS showed a shift in elution volume. Furthermore, the absorbance of the FITC label shifted with the protein peak corroborating the presence of casein (Figure 4-1, top right). This sample was taken and applied to holey carbon grids and vitrified before electron micrograph data collection and single particle selection.

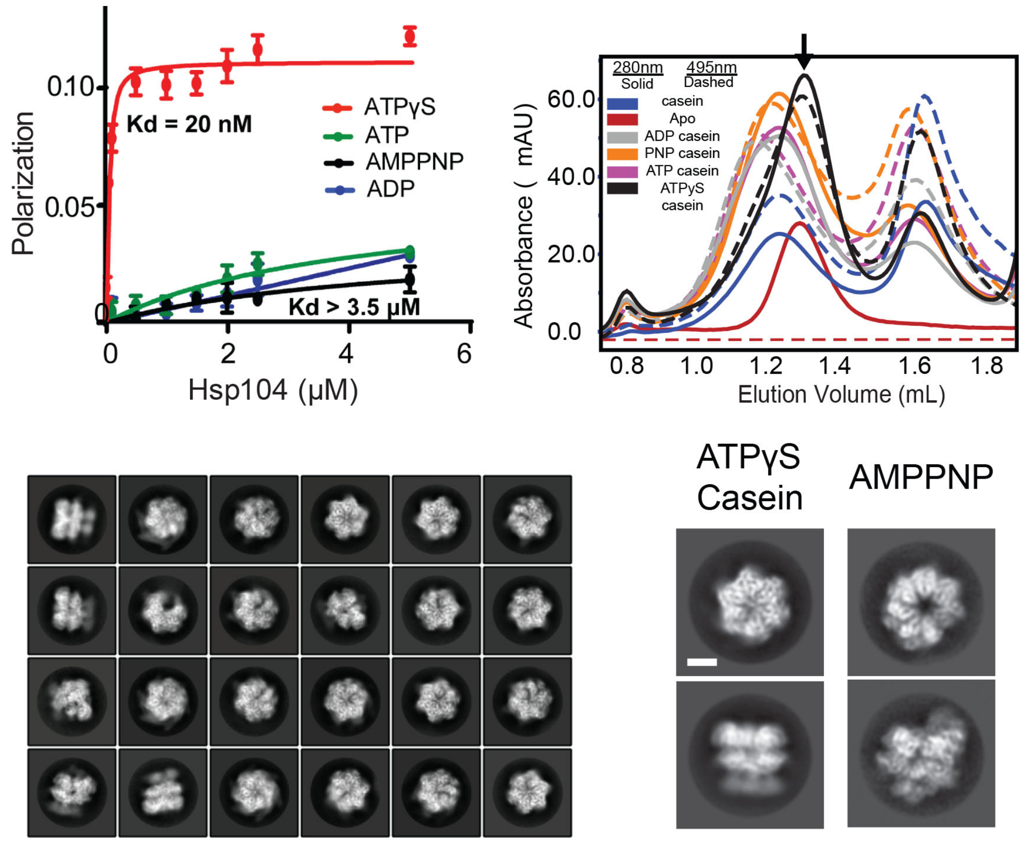

Figure 4-1 Substrate-bound Hsp104:casein and 2D classification (top, right) FITC-casein binding analysis, measured by fluorescence polarization in the presence of: ATP-γ-S (red), ATP (green), AMP-PNP (black), and ADP (blue) (values = mean ± SD, *n* = 3). (top, right) Hsp104 and casein incubated with the indicated nucleotides, showing a shift in peak elution and alignment of the absorbance curves for protein, 280 (solid), and FITC, 495 (dash) occurs specifically in the presence of ATPγS. Fraction collected for cryo-EM characterization of Hsp104:casein is indicated (arrow). (bottom, left) Representative reference-free 2D class averages of the purified Hsp104:casein complex incubated with ATPγS. (bottom, right) Representative top- and side-view 2D class averages comparing the Hsp104–ATP-γ-S:casein closed state and Hsp104–AMP-PNP open state. Fluorescence polarization was performed by members of the Shorter lab

Two-dimensional (2D) reference-free classification of purified Hsp104:casein-ATPγS complexes revealed stable and high resolution class averages (Figure 4-1, bottom left). Additionally, the Hsp104:casein-ATPγS complex a large rearrangement compared to the AMPPNP-bound open state (Yokom et al., 2016) (Figure 4-1, bottom right). An initial 3D structure refined to ~3.9 Å resolution. However, a two-protomer site was identified to be flexible so further data processing was pursued.

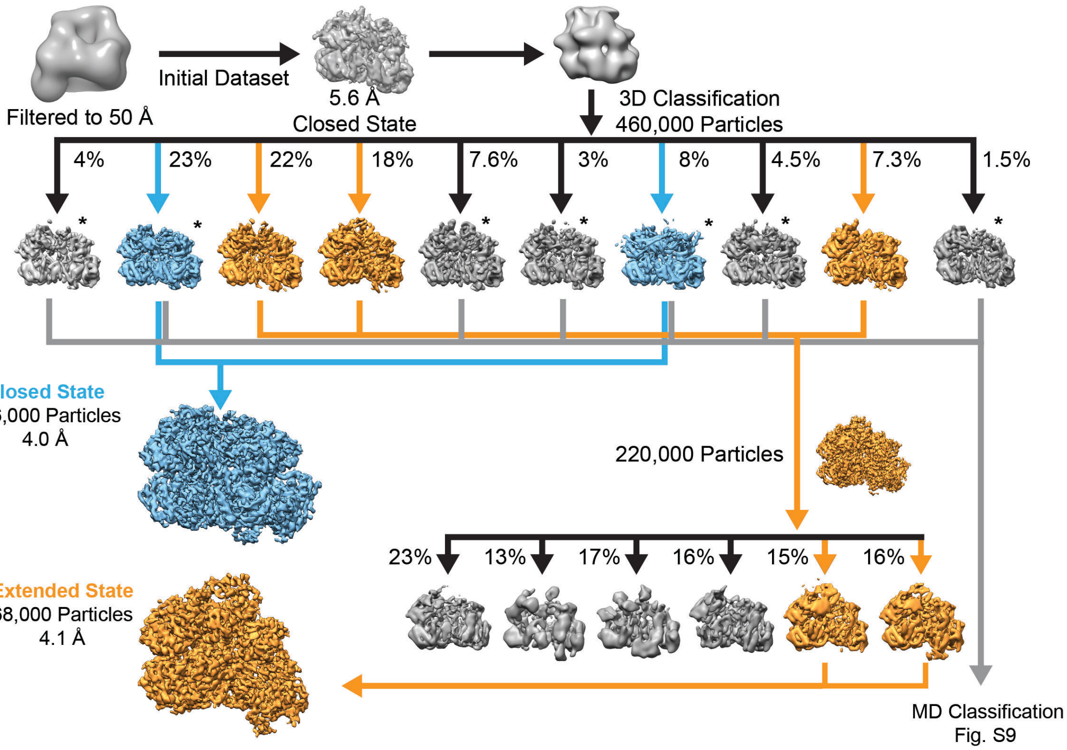

Figure 4-2 3D classification scheme for the Hsp104:casein dataset Indicated classes were used for closed (blue), extended (orange) and MD class (grey) refinements, with a 3D sub-classification of the extended-state single particles to achieve a better-resolved P6-P1 interface. Classes indicated with an (*) were confirmed to be in the closed state but resulted in no improvements in resolution and thus were excluded during the final refinements.

Extensive 3D classification resolved these protomers and revealed two hexamer conformations, denoted: “closed” and “extended” (Figure 4-2). This classification sorted the single particles into ten 3D reconstructions as lower resolution then when all particles were included. However, three classes accounting for 47% of the single particles showed differences and were separated from the rest of the data (Figure 4-2). This was the first indication that we may have multiple conformations within a single protein complex data set.

Refinement of the closed state yielded a 4.0 Å-resolution map with well-resolved protomers and axial channel. This reconstruction showed similar features as the total data set map however the flexible protomers were significantly enhanced. The AAA+ subdomains show side-chain features, enabling an atomic model to be built and refined using a homology model from the bacterial orthologue ClpB (Lee et al., 2003) (Figure 4-3).

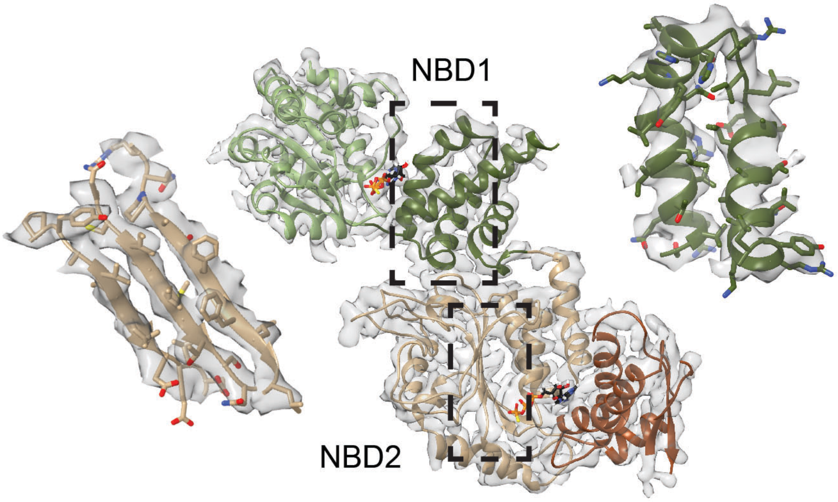

Figure 4-3 High resolution AAA+ domains Atomic model and segmented map of the AAA+ small (NBD1, green) and large (NBD2, brown) subdomains.

The AAA+ domains (protomers denoted P1-P6 same as the labeling of AMP-PNP model) form a near-symmetric closed double-ring (Figure 4-4). Protomers P2-P5 are identical (RMSD = 2 Å) while the two mobile protomers, P1 and P6, each adopt different conformations. The outside hexamer diameter is ~115 Å (compared to 125 Å for the open state), and density for the AAA+ domains surround a ~10 Å-wide axial channel. Remarkably, the channel is partially occluded by a continuous, 80 Å strand of density that, based on the molecular model, is an unfolded portion of the substrate, casein (Figure 4-4, yellow).

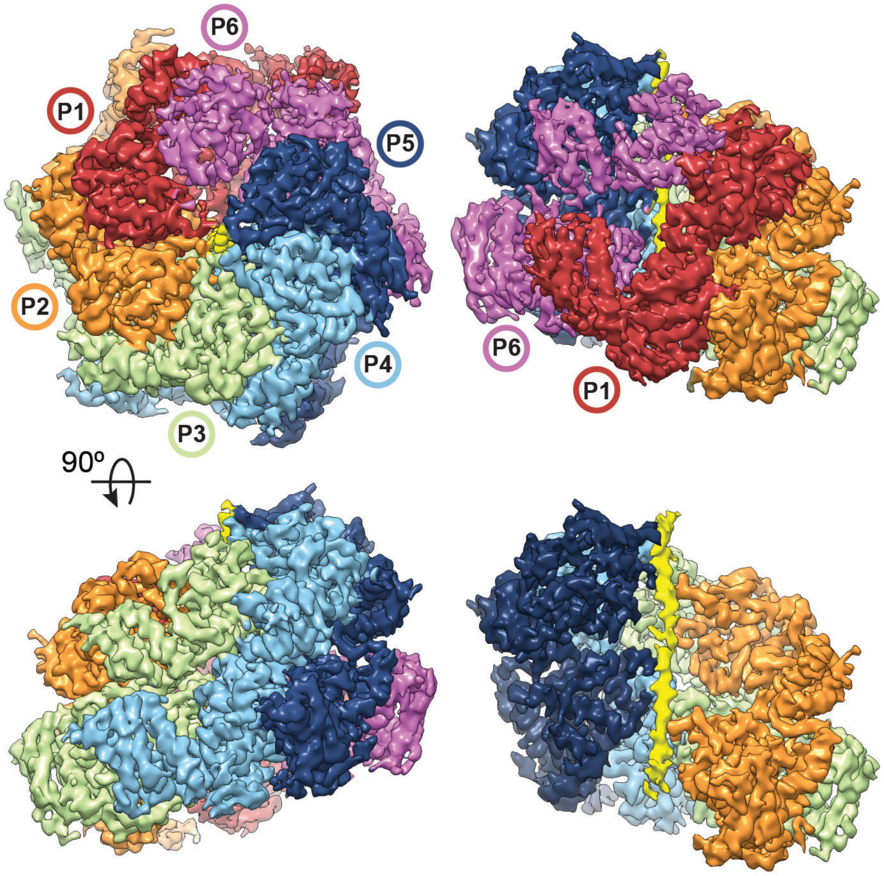

Figure 4-4 Substrate bound closed state of Hsp104: ATP-γ-S (left) Final reconstruction of Hsp104:casein segmented by protomers (P1 to P6) and substrate (yellow). (top, right) Side view of the mobile protomer face (P1 and P6). (bottom, right) Channel view showing substrate polypeptide density (yellow).

Tyr Pore-Loop Contacts Along Substrate

In the closed state, pore-loop strands from both AAA+ domains become ordered compared to Hsp104-AMPPNP (Yokom et al., 2016) and other structures (Carroni et al., 2014; Lee et al., 2003), and contact substrate in a right-handed spiral arrangement (Figure 4-5). These regions are among the most highly resolved (< 4.0 Å), indicating bona fide interactions critical for translocation. The casein sequence could not be determined from the density; therefore a strand of 26 Ala residues was modeled. This represents the backbone and alpha-carbons of the polypeptide chain. Hsp104 translocates unfolded polypeptides in the presence of ATPγS (Tessarz et al., 2008), therefore, the pore loop-substrate interactions likely adopt a fixed register during translocation. Alternatively, a specific region of casein may be uniformly trapped in the channel but this is unlikely. Substrate contacts are made by five protomers (P1-P5), while protomer P6 breaks the helical arrangement and makes no direct contact (Figure 4-5, dotted circle). Substrate density is not observed outside the channel, thus non-translocated portions of casein are likely disordered.

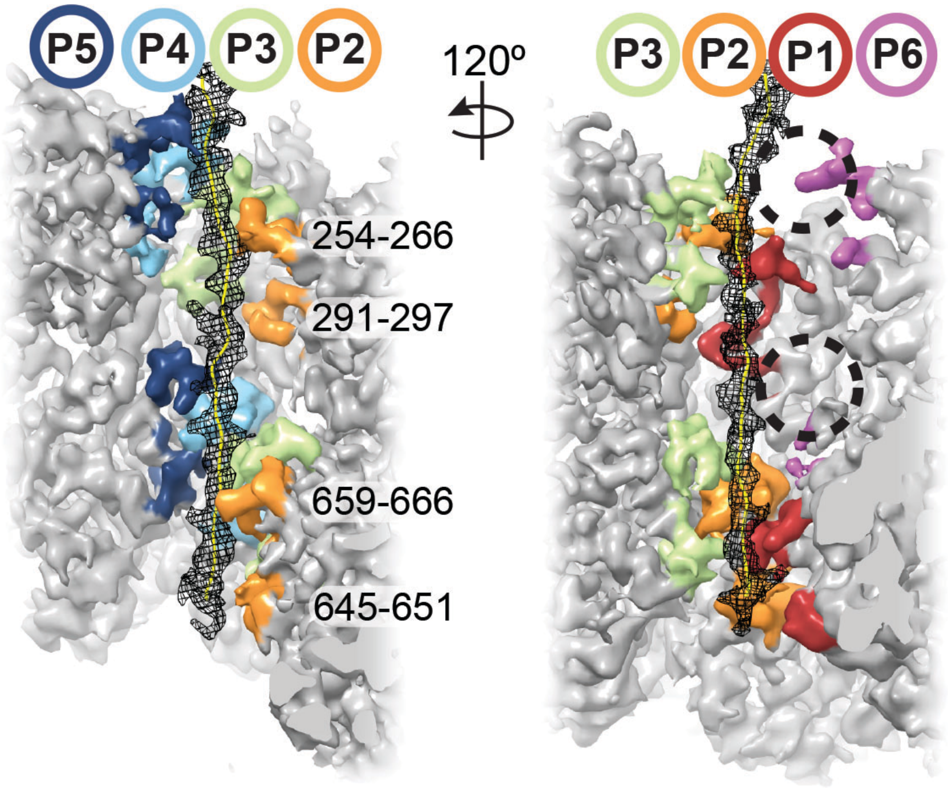

Figure 4-5 Structural basis for substrate binding in the axial channel Channel view of the map showing the extended poly-Ala strand modeled as the substrate (mesh) and pore loops with residues indicated. The P6 pore-loop regions not contacting substrate are indicated (circles)

Conserved pore-loop tyrosines 257 and 662 in protomers P1-P5 directly contact substrate, potentially via the aromatic rings, which are positioned ~4-5 Å away from the backbone (Figure 4-6). Together with conserved V663 in NBD2, these residues contribute the majority of substrate interactions in the channel. The lower loops (291-297 for NBD1 and 645-651 for NBD2) are also ordered and adjacent to the substrate, and K649 and Y650 for P2 and P4 appear to make contact.

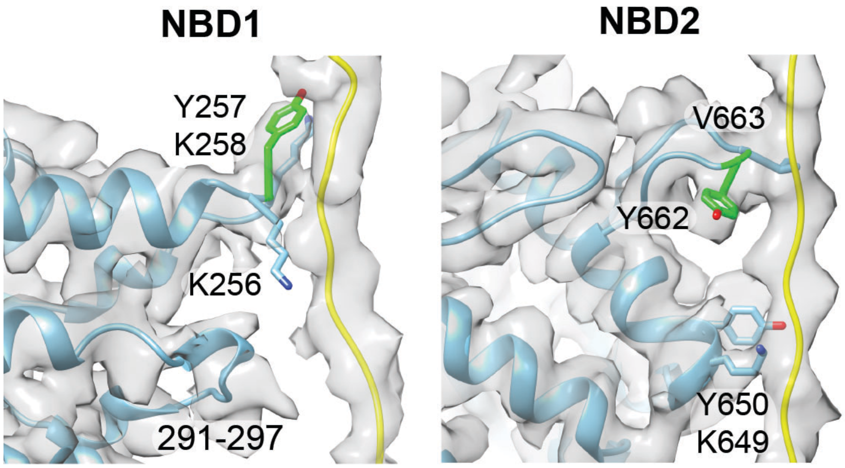

Figure 4-6 Direct contact of tyrosine pore loops Model and cryo-EM density showing P4 pore loop–substrate interactions mediated by Y257 (green) in the NBD1 and Y662 (green) and V663 in the NBD2, as well as additional, noncanonical pore loops that include residues K649 and Y650. Polypeptide change is shown in yellow.

The pore loops are separated by ~6-7 Å along the channel, making contact with approximately every second amino acid of the substrate. K256 and K258 in NBD1, which flank Y257, project towards neighboring loops, possibly stabilizing the spiral arrangement. Protomers P1 and P5 comprise the lowest and highest contact sites with the substrate and are separated by ~26 Å along the channel axis. Protomer P6 is between these sites, but disconnected from the substrate; its NBD1 pore loop is 13 Å away while its NBD2 pore loop was less resolved and unable to be modeled. Overall, this structure reveals that substrate interactions are mediated almost entirely by the conserved Tyr residues, establishing their direct role in coordinating substrate during translocation (Olivares et al., 2014; Sweeny and Shorter, 2016).

Ratchet-Like States of Protomers

In addition to the closed state, our 3D classification analysis identified an ‘extended’ conformation of Hsp104:casein (Figure 4-2). Further classification and refinement resulted in a 4.1 Å resolution map from which an atomic model was determined (Figure 4-2). The structure reveals a substrate-bound hexamer with a different arrangement of the mobile protomers P1 and P6, which show distinct flexibility in the NBD1 and NBD2, respectively (Figure 4-8, left).

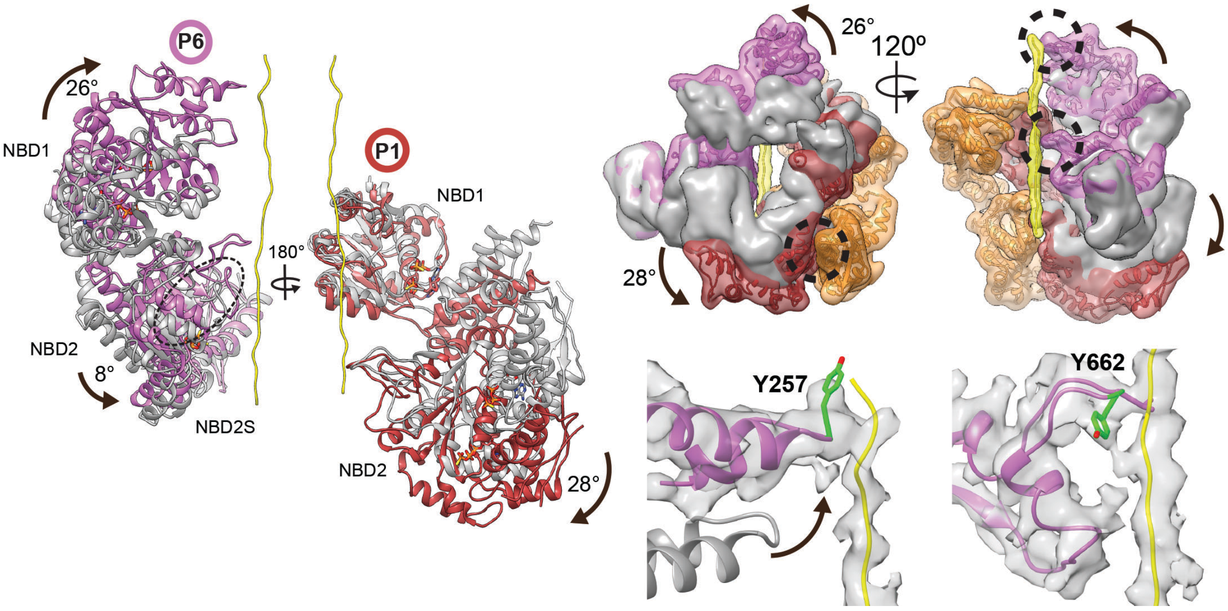

Figure 4-7 Conformational differences and pore loop-substrate contacts in the closed and extended states. (left) Overlay of the P6 and P1 protomers in the closed (grey) and extended (magenta and red, respectively) states following alignment of the hexamers identifying specific NBD1 and NBD2 rotations. (top, right) Filtered map of P1 (red) and P6 (magenta) overlaid with the corresponding closed-state protomers (gray) after alignment to P4 in the hexamer. NBD conformational changes (arrows) resulting in extended-state interactions (black circles) with substrate (yellow) and the P2-NBD2 (orange) are shown. (bottom, right) Model and map of the P6-NBD1 and -NBD2 pore loops showing change in the pore-loop position (arrow) compared to the closed state (gray) for NBD1 and substrate contact by Y257 and Y662 (green).

Protomers P2-P5 are identical to the closed state (RMSD = ~0.8 Å) and density for the polypeptide substrate is slightly extended at the top of the channel, but overall similar and localizes to the same region.

The closed-extended state conformational differences for P1 and P6 are substantial (RMSD = 13.7 Å and 11.5 Å, respectively) and involve rotations of P1-NBD1 and P6-NBD2 (Figure 4-7, top right). P6 rotates towards the channel axis and the pore loops become well-ordered and directly contact substrate. The P6 pore-loop tyrosines, Y257 and Y662, directly contact substrate similarly as the other protomers (Figure 4-7, bottom right). Conversely, P1-NBD2 rotates counterclockwise, releasing its interaction with P6 to contact P2-NBD2 but maintains contact with the substrate.

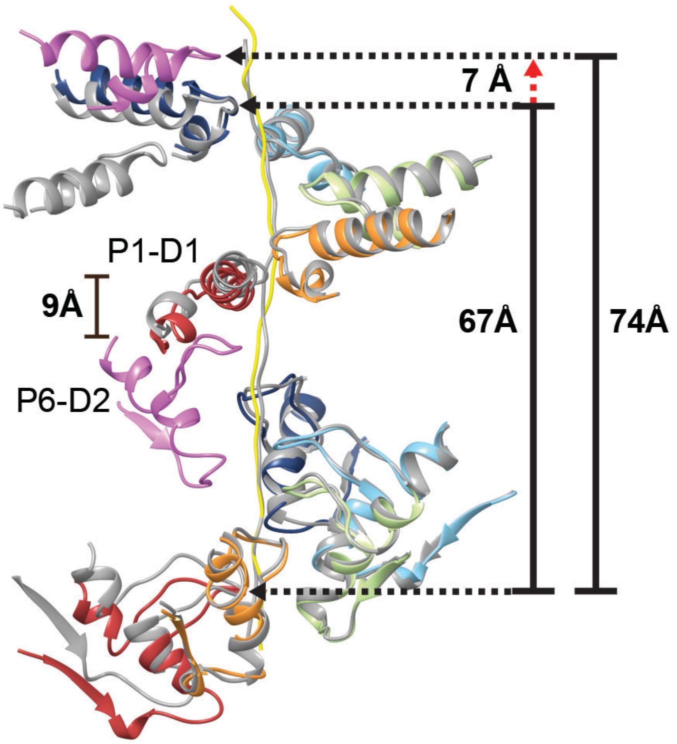

Figure 4-8 Pore loop overlay of closed and extended states. Overlay of the of the pore loops and polypeptide substrate in the closed (grey) and extended (colored by protomer) states showing complete substrate engagement and a 7 Å translocation step along the polypeptide that occurs in the extended state.

Remarkably, P6-Y257 becomes positioned at the topmost contact site along the polypeptide, advancing interactions by 2 amino acids (~7 Å) compared P5-Y257 (Figure 4-8). These changes bring P6 pore loops in register to form a two-turn right-handed spiral of contacts. Each pore loop rotates ~60° and rises ~6-7 Å, enabling evenly spaced Tyr-substrate interactions across a 74 Å-length of the channel. Together, the extended and closed states reveal a ratchet-like conformational change of the hexamer that yields a two-amino acid translocation step. While other conformations may exist that were not resolved, the extended and closed states predominate the dataset, therefore, these changes are likely critical for orchestrating substrate binding and release steps during translocation.

Coordinated Nucleotide Pockets

NBD1 and NBD2 nucleotide pockets were examined to determine how nucleotide state is coupled to substrate interactions. P3-P5 nucleotide pockets are identical with well-resolved density and a bound ATPγS (Figure 4-10). In NBD1, R334 from the clockwise neighboring promoter contacts the γ-phosphate, establishing this residue as the Arg finger (Wendler et al., 2007). R333 is adjacent the α/β-phosphates, acting potentially as a sensor residue considering that the NBD1 does not contain a cis sensor 2 motif (Erzberger and Berger, 2006). In the NBD2 pocket, the Arg finger, R765, interacts with the γ-phosphate while the sensor 2, R826 in the cis protomer, is positioned adjacent the α/β-phosphates (Figure 4-10). Thus, for P3-P5, which make well-defined contacts with the substrate in both states, NBD1 and NBD2 are primed for ATP hydrolysis.

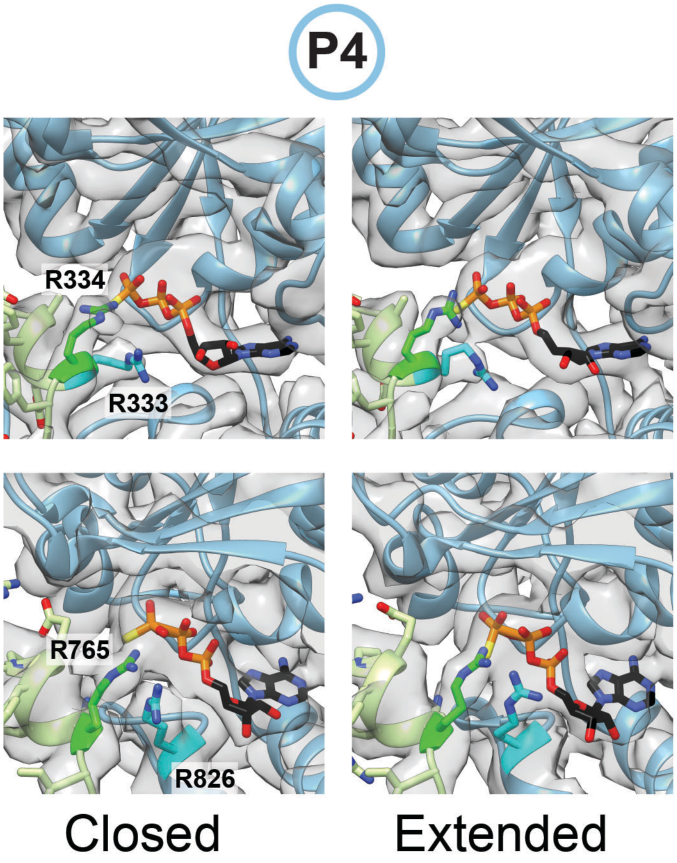

Figure 4-9 Arrangement of the nucleotide pockets in the closed and extended states. Cryo-EM density and model for the NBD1 and NBD2 nucleotide pockets of P3-P5, in the closed and extended states, showing an active configuration. The Arg finger residues (green), R334 (NBD1) and R765 (NBD2), from the adjacent protomer (helix B8 and helix D12, respectively) and the putative NBD1 sensor 2, R333 (cyan) and the NBD2 sensor 2, R826 (cyan) are shown.

Conversely, the mobile promoter (P6, P1, and P2) NBDs (Figure 4-11), are in different active and inactive configurations, based on the position of Arg fingers and nucleotide density. For the P6 protomer, both NBDs appear inactive in the closed state with P5-R334 ~12 Å away and P5-R765 ~6 Å from the respective NBD1 and NBD2 γ-phosphate in P6. In contrast, both P5-R334 and P5-R765 in the extended state are identified to contact the respective γ-phosphates directly, indicating these sites are in an active configuration. Notably, the closed-extended conformational change results in both nucleotide-pocket activation and substrate contact by P6.

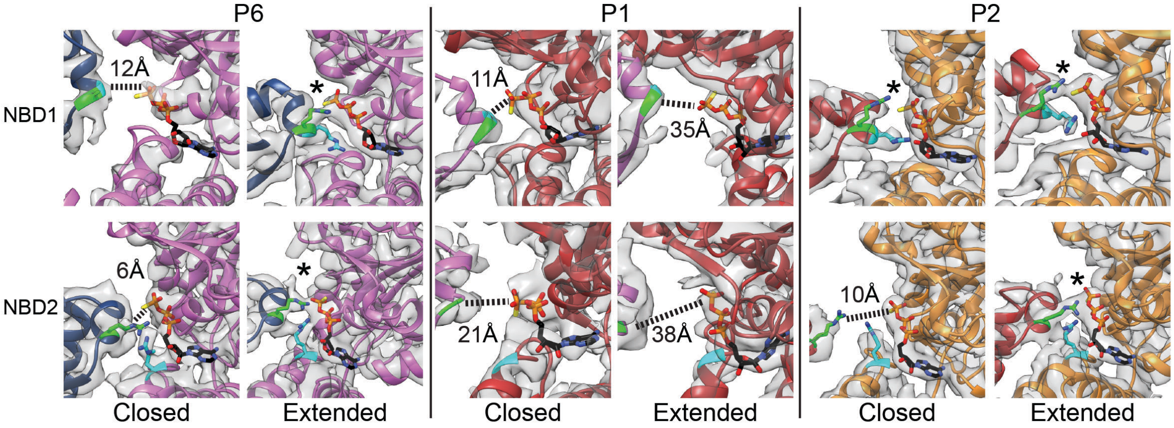

Figure 4-10 Classification of nucleotide binding pockets in closed and extended states. Map and model of the P6, P1, and P2 nucleotide pockets. Arg fingers NBD1-R334 and NBD2-R765 are shown (green) with γ-phosphate contact indicated (*) for the active sites and distances shown for the inactive sites. Sensor 2 residues NBD1-R333 and the NBD2-R826 are shown (cyan).

P1 contacts substrate at the lowest position in the hexamer and appears inactive in both states. In the closed state, P6-R334 is ~11 Å away and P6-R765 is ~21 Å from the respective γ-phosphate in P1. These Arg residues are further separated from the nucleotide pockets in the extended state, with R333, R334, and R765 more than 30 Å away. For P2, NBD1 is in an active configuration in both states. However, P2-NBD2 switches from inactive in the closed state to active in the extended state due to the P1-NBD2 conformational change that brings R765 adjacent the γ-phosphate. Finally, based on difference maps, density for nucleotide is present in all sites, but appears reduced at certain sites: NBD1 in P6 and P1 for the closed state, and the NBD2 in P1 for both states, indicating partial occupancy or a post-hydrolysis state.

The NBD states along with substrate interactions are depicted in a schematic to explain how active site rearrangements and the closed-extended conformational changes drive substrate translocation (Figure 4-11). In the closed state, substrate is bound by five protomers with four NBD1 sites and three NBD2 sites in an active (ATP) configuration. By contrast, in the extended state, substrate is bound by six protomers with five NBD1 sites and five NBD2 sites in an active state. Importantly, the 'off' protomer (P6) that is unbound to substrate in the closed state becomes active in the extended state and binds substrate at the next position. The protomer counterclockwise from this position is in the lowest 'down' position (P1) and remains inactive in both states, but undergoes a rotation in the extended state that activates NBD2 of the neighboring protomer.

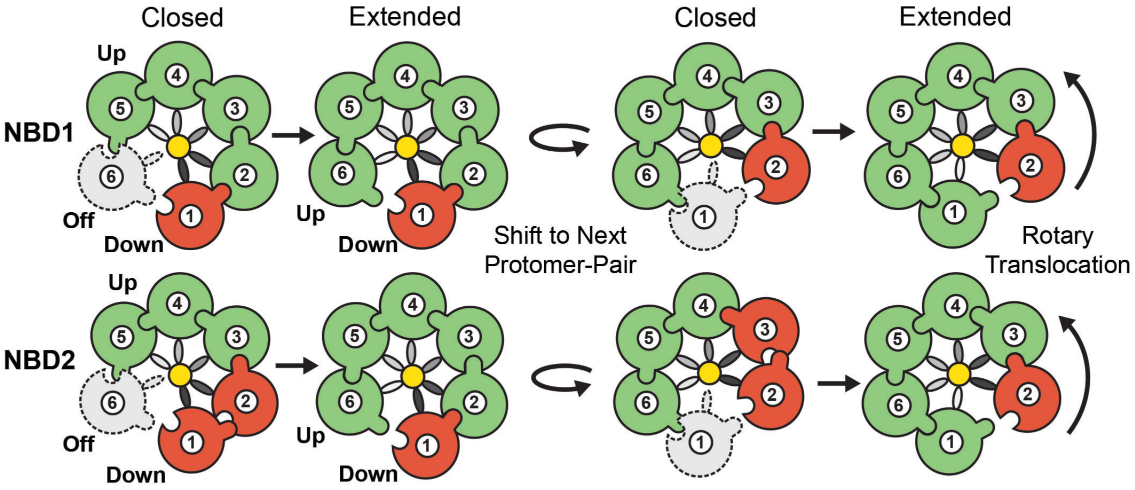

Figure 4-11 Nucleotide hydrolysis is couple to translocation Rotary translocation model showing closed-to-extended states resulting in active (green), inactive (red), and unbound or inactive (gray dash) states of the NBDs. Pore-loop spiral (gray gradient) is shown contacting substrate (yellow). Arg-finger contact and NBD activation is depicted by the interlocking contact.

These results suggest a rotary-type translocation mechanism whereby four protomers remain bound to substrate in a similar configuration with the NBDs primed for hydrolysis, while two protomers at the transition site between the lowest and highest position undergo conformational changes that alter substrate interactions. Given the right-handed spiral of pore loops, position of the ‘up’ and ‘down’ protomers, and NBD1-NBD2 direction of translocation, peptide movement could occur through a counterclockwise cycling of these closed and extended states. Based on this model the inactive protomer in the ‘down’ position could release substrate and re-engage in the ‘up’ position, thereby advancing translocation by a two-amino acid step. Transmitting these changes counterclockwise would enable the hexamer to advance processively along the polypeptide during translocation. Some variability in the step size, potentially to accommodate bulky residues, could be achieved by conformational changes in the extended-state protomer in the ‘up’ position that shift its pore-loop contact. These results parallel the right-handed substrate interactions and rotary-driven hydrolysis models for DNA/RNA helicases, including AAA+ (E1, DnaA and MCM) (Abid Ali et al., 2016; Enemark and Joshua-Tor, 2006; Erzberger and Berger, 2006)and RecA (Rho) (Thomsen and Berger, 2009) families. Thus, this ratcheting mechanism may be conserved among many ATP-driven translocases.

Allosteric Control by the MD

The Hsp104-AMPPNP structure revealed a MD-NBD1 interaction that suggested an allosteric control mechanism (Yokom et al., 2016). To further explore the MD and the role of nucleotide in the Hsp104 conformational cycle we determined the cryo-EM structure of Hsp104 incubated with ADP to 5.6 Å resolution (Gates et al., 2017). The reconstruction revealed an identical AAA+ arrangement compared to Hsp104-AMPPNP (RMSD = 2.5 Å) but isolated a unique MD-MD interaction. This interaction forms a crisscross MD network and may serve as in important regulator of Hsp70 interaction, ATPase allosteric control and hexamer stability. However, both of these MD positions were seen in fully saturating conditions with all ATP or ADP bound AAA+ domains.

Therefore, to determine MD conformations in the casein-bound complex, additional 3D sub-classification analysis and refinement was performed on the Hsp104 closed-state data without applying a mask (Figure 4-12). Three classes with distinct MD arrangements were identified: MD Class 1, Class 2 and Class 3, which refined to 6.7-6.9 Å (Figure 4-12). For these maps, the AAA+ core and substrate density are identical to the closed-state structure.

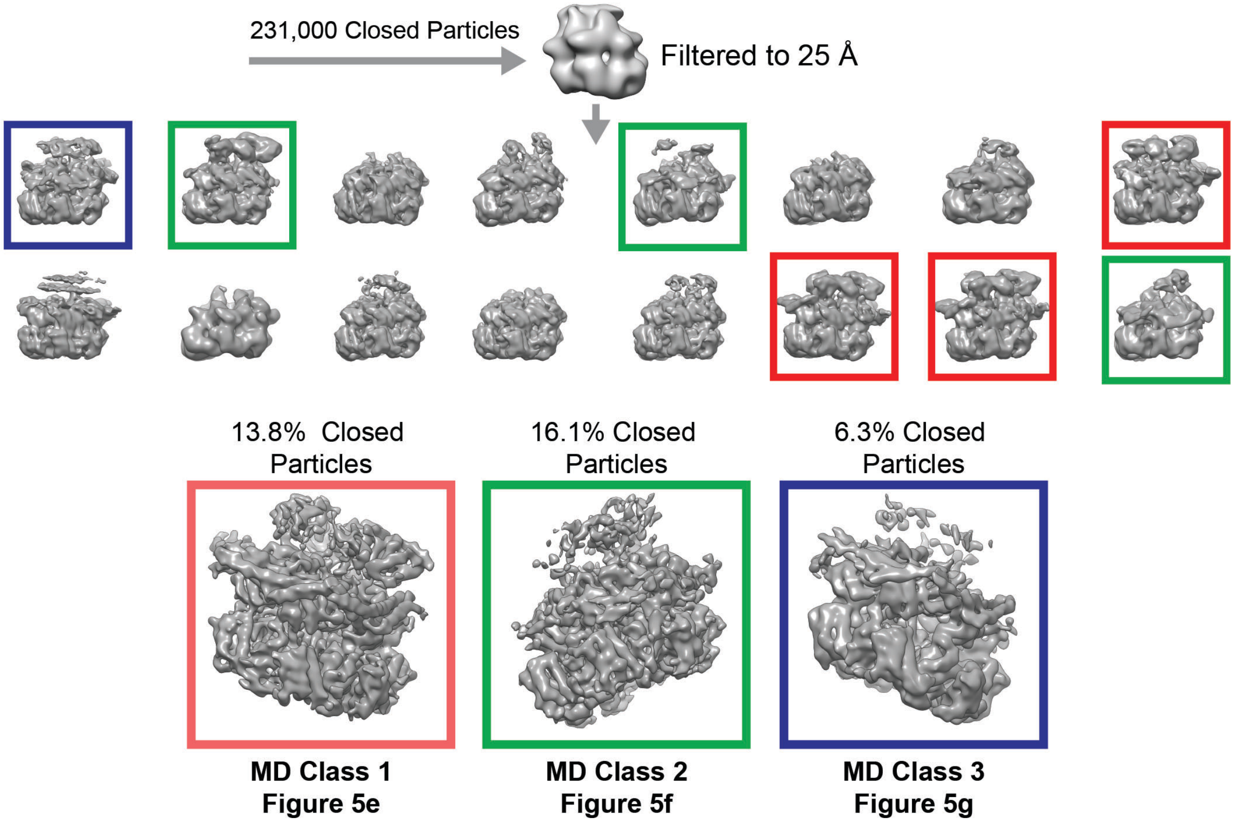

Figure 4-12 3D classification scheme and refinement of MD Class1-3. Scheme showing 3D sub-classification of the closed state classes performed following initial classification (Fig. S2D) resulting in MD Class 1 (red) Class 2 (green) and Class 3 (blue) reconstructions that identify distinct ATP- and ADP-state MD conformations.

In the MD Class1, density corresponding to the MD coiled-coil is identified for 4 protomers (P1, P2, P5 and P6), revealing an ADP-state, crisscross arrangement around the P6-P1 mobile-protomer face (Figure 4-14, left). Notably, the NTDs for all protomers are also resolved in this class, revealing that they interact together in an alternating, triangular arrangement with the polypeptide strand oriented asymmetrically in the channel, towards the P3 and P5 NTDs (Figure 4-13). This arrangement fits well with previous NTD substrate binding surfaces which highlight a hydrophobic cleft for recognition (Rosenzweig et al., 2015). Furthermore, recent crystal structures of the *Saccharomyces cerevisiae* and *Candida albicans* Hsp104 NTDs has revealed that the *S. cerevisiae* has a propensity to form dimers. The two hydrophobic patches are turned toward each other and could form a large surface for different substrate engagement. Of note, this arrangement is seen in our trianglular NTD architecture, between P5-P4, P3-P2 and P1-P6. Lower resolution of the MD class 1 model does not allow precious positioning of side chains in this region.

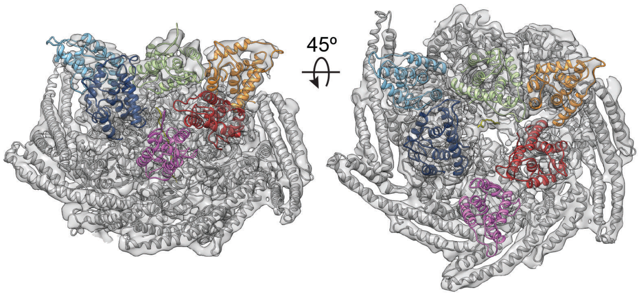

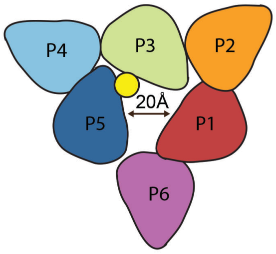

Figure 4-13 Arrangement of NTDs in MD Class1. (top) Map and model of MD Class 1 showing the NTD-NBD1 region, NTDs colored corresponding to protomer, as above. (bottom) Schematic based on the model showing alternating orientation of the NTDs and triangular arrangement of the channel entrance with substrate (yellow) positioned off-center, adjacent P3 and P5.

For MD Class 2, density corresponding to MD helices L1 and L2 is identified for protomers P3-P5 revealing L1 is positioned across the clockwise protomer, indicating an ATP-state conformation (Figure 4-14, middle). For Class 3 both MD conformations are identified: P1, P5, and P6 adopt the ADP-state, while P3 and P4 are in the ATP-state (Figure 4-14, right). This classification captures specific MD conformations that are in remarkable agreement with our analysis of the nucleotide pockets (Figure 4-10, 4-11). Thus, in an actively translocating hexamer, MD conformational changes likely propagate around the hexamer in accordance with nucleotide state. The MD could function to lock the ATP state for protomers that are in contact with substrate (P2-P5) and transition to a release, ADP-state towards the mobile face, thereby allosterically tuning the closed and extended conformational changes that advance substrate.

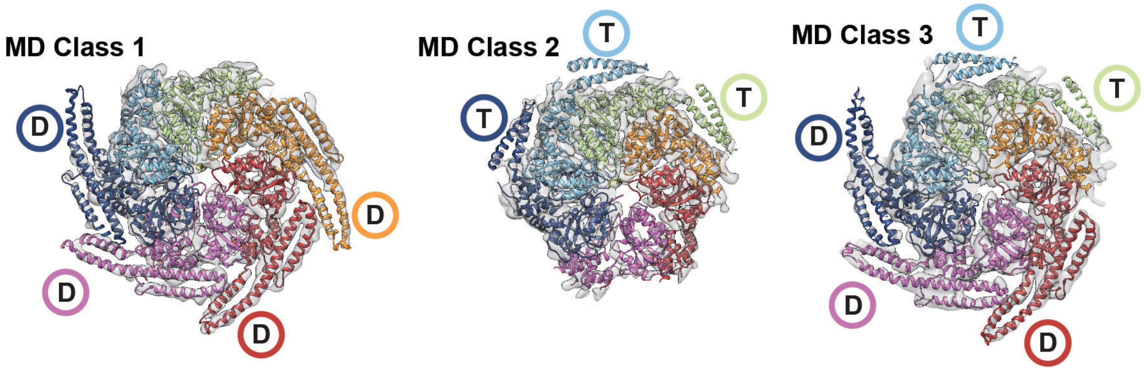

Figure 4-14 Nucleotide-specific MD conformations around the hexamer, Final reconstructions and models of Hsp104:casein after classification analysis identifying the ADP-state (D) or ATP-state (T) MD conformation.

To determine how the open and closed states may function together, cryo-EM datasets of wildtype and mutant Hsp104 incubated with different nucleotides were analyzed by 2D and 3D classification methods (Figure 4-15). As expected, AMPPNP and ADP datasets classify with 100% of the data matching the open conformation. With ATP incubations, alone and with substrate, Hsp104 primarily adopts the open conformation (>80%), however a notable fraction (10-20%) is in the closed state. A 3D reconstruction of the Hsp104-ATP was determined to 6.7 Å and is identical to the AMPPNP and ADP-bound structures (cross-correlation = 0.98). Thus, during active hydrolysis the open state is favored, however both conformations exist in equilibrium. With ATPγS, nearly 80% of hexamers are in the closed state (Figure 4-15) which increases to 100% with casein, demonstrating that ATPγS and substrate together trigger complete conversion to the closed state.

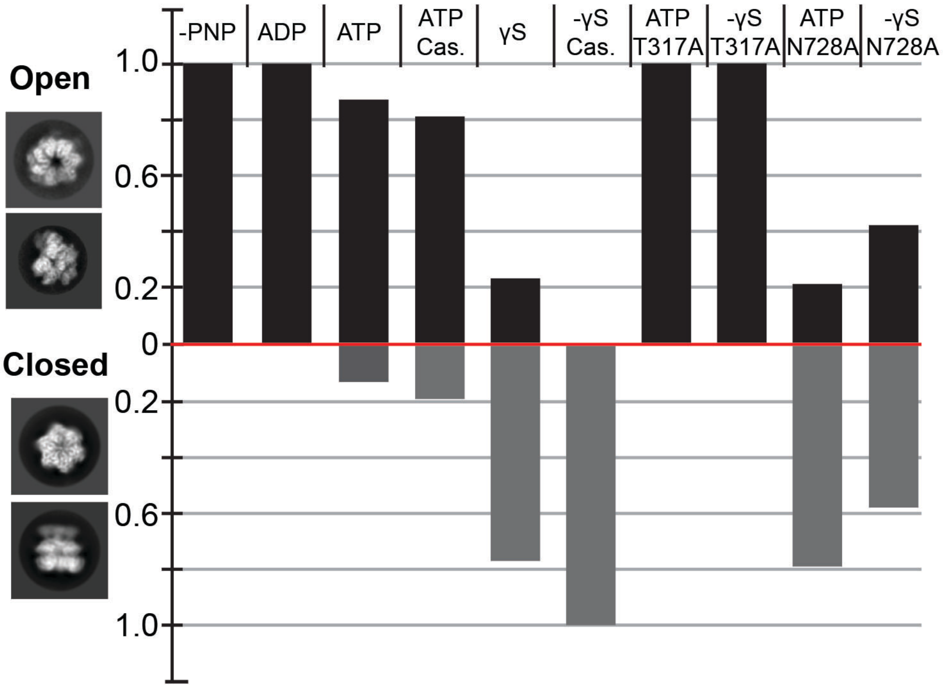

Figure 4-15 Nucleotide-state and NBD function in the open-closed conformations The fraction of open and closed conformations, determined by 3D classification analysis, is shown for wild-type Hsp104 and sensor 1 ATPase mutants (T317A in NBD1 and N728A in NBD2) after incubation with indicated nucleotides and substrate (-PNP stands for AMP-PNP; -γ-S stands for ATP-γ-S).

The sensor 1 ATPase mutants (Hattendorf, 2002), T317A in NBD1 and N728A in NBD2, were investigated to determine the role of NBD1 and NBD2 function. In contrast to wildtype, T317A incubated with ATP or ATPγS classifies with 100% matching the open state, indicating that a hydrolysis-active NBD1 promotes the closed conformation. Conversely, ~80% and 60% of N728A hexamers match the closed state in the presence of ATP and ATPγS, respectively. In casein-binding experiments (Figure 4-16), N728A binds with high affinity (K_d ~33nM), while wildtype and T317A show weak binding (K_d > 2μM) (Fig. 6B) in the presence of ATP. With ATPγS, both wildtype and N728A bind with a high affinity (K_d ~16-20nM), whereas T317A has a reduced affinity, in comparison (K_d

~1.4μM). Thus, Hsp104 exists in open-closed conformational equilibrium that is differentially controlled by NBDs. Hydrolysis by NBD1 promotes the closed state, while hydrolysis by NBD2 favors the open state. Substrate binding and the open-closed conformational change (Figure 4-17) are coupled and likely driven by NBD1 function, whereas NBD2 may be important for substrate release steps.

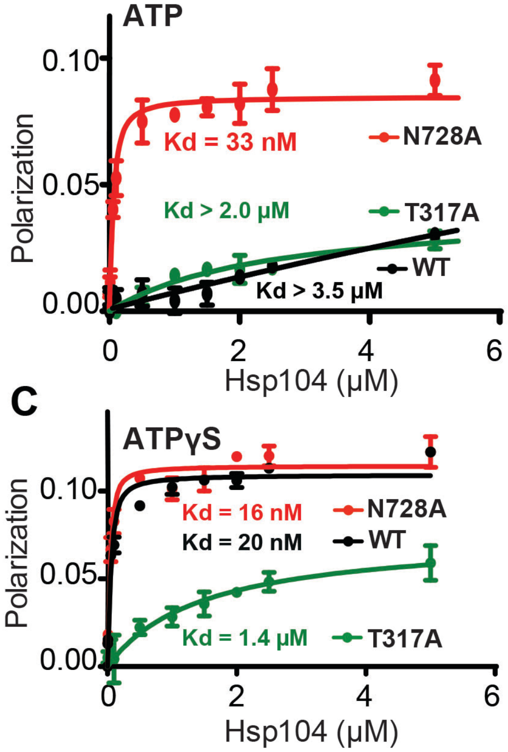

Figure 4-16 Fluorescence polarization of mutant Hsp104 complexes. FITC-casein (60 nM) binding to Hsp104 wild type (black) and mutants T317A (green) and N728A (red) in the presence of (2 mM) ATP (B) or ATP-γ-S (C). Values represent mean ± SD (*n* = 3).

Massive conformational changes are required to transition between the open and closed states. In the open state, protomer P1 is in the topmost position and the hexamer adopts a left-handed spiral with P6 ~50 Å below, along the axial channel. Upon conversion to the closed state, P6 shifts by ~65 Å, and rotates towards the channel by ~60°, resulting in a right-handed spiral and a channel that has narrowed by ~10 Å.

Considering that substrate interactions and hydrolysis by NBD1 are critical for the closed state, we propose that this large conformational change drives substrate binding and release steps of the cycle (Figure 4-18). When the conformational change is modeled with substrate, nearly 30 residues can be translocated into the channel. Additionally, similar open ‘lock-washer’ conformations are populated by other translocases (Lyubimov et al., 2012; Skordalakes and Berger, 2003; Śledź et al., 2013; Zhao et al., 2015), which may represent a conserved ‘off-state’.

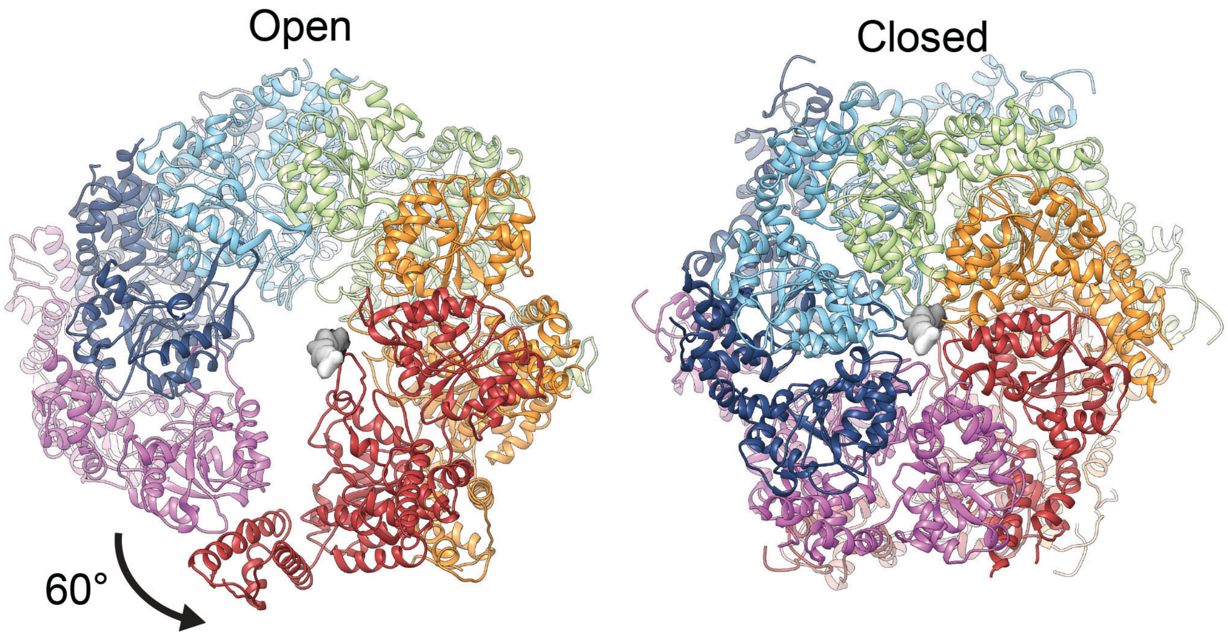

Figure 4-17 Comparison of the channel in the open and closed state. Top views of open and closed states, colored by protomers, showing the hexamer undergoes a ~60° rotation.

4.4 Discussion

Disaggregation involves nonprocessive and processive mechanisms (DeSantis et al., 2012; T. Li et al., 2015). Cycling between the open and closed states may enable nonprocessive bind/release “pulling” events (Figure 4-18). Alternatively, the two-different substrate-bound states suggest a processive mechanism whereby two protomers undergo ratchet-like conformational changes that enable substrate binding and release steps to occur while the hexamer remains engaged. This rotary-like mechanism could drive disaggregation when coupled to stepwise cycles of ATP hydrolysis around the ring. Such a cooperative mechanism could enable dissolution of more stable aggregates or amyloids (DeSantis et al., 2012). While this mechanism contrasts with 'stochastic' models proposed for ClpX (Olivares et al., 2014), Hsp104 may exhibit different conformational cycles tuned to different substrates (DeSantis et al., 2012). Remarkably, both extended and closed states reveal a precise 6-7 Å separation of the pore loop-substrate contacts. A two-amino acid step involving conformational changes at the spiral interface would continually maintain this register during translocation. This pore-loop spacing is observed in related AAA+ rings (Glynn et al., 2009; Matyskiela et al., 2013; Wehmer and Sakata, 2016), and likely represents a conserved feature of translocases. While additional states are likely involved, our structures reveal the remarkable structural plasticity of Hsp104, which enables adaptable mechanisms of protein disaggregation (DeSantis et al., 2012; Sweeny and Shorter, 2016).

Overall the structure determination of substrate bound Hsp104 has given us the first complete model for Hsp104 translocation (Figure 4-18). The three distinct structures, open, closed and extended explain previous biochemical data and tremendously advanced our understanding of this chaperone system.

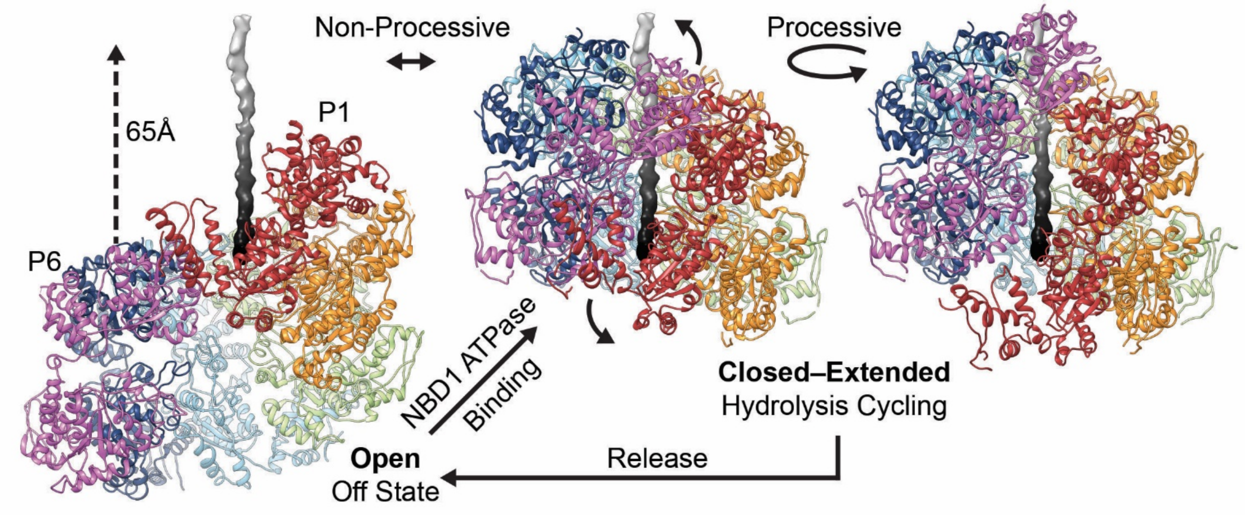

Figure 4-18 Hsp104 translocation mechanism involves processive and non-processive modes Proposed models for non-processive and processive modes of translocation involving open to closed conformational change upon substrate engagement/release and ratchet-like open-to-extended protomer changes that occur around the hexamer during cycles of ATP hydrolysis.

4.5 Methods

Purification, Fluorescence Polarization, and Size Exclusion Chromatography

All Hsp104 variants were generated using QuikChange site-directed mutagenesis (Agilent) and confirmed by DNA sequencing. Hsp104, Hsp104^{T317A}, Hsp104^{N728A}, Hsp104^{E412K}, Hsp104^{R194E}, Hsp104^{E427K}, Hsp104^{R353E}, Hsp104^{D434K}, and Hsp104^{R366E} were purified as described (Jackrel et al., 2014; Torrente et al., 2014). Hsc70 and Hdj2 were from Enzo Life Sciences. For fluorescence polarization studies, Hsp104^{WT}, Hsp104^{T317A}, or Hsp104^{N728A} were exchanged into 40 mM Hepes-KOH pH 7.4, 20 mM $MgCl_2$, 150 mM KCl, 10% Glycerol (v/v), 2 mM 2-Mercaptoethanol. To assess FITC-casein binding, FITC-casein (60 nM) was incubated with increasing concentrations (0-5μM hexameric) of Hsp104, Hsp104^{T317A}, or Hsp104^{N728A} with 2 mM of the indicated nucleotide for 10 min at 25°C. For the ATP condition, an ATP regeneration system (5mM creatine phosphate and 0.125μM creatine kinase) was also included to maintain the ATP concentration. Fluorescence polarization was measured (excitation 470 nm, emission 520 nm) using a Tecan Infinite M1000 plate reader. The binding isotherms were analyzed using MicroMath Scientist 3.0. Parameters: IndVars=Xt; DepVars=P; Params: Bmax, K, Mtot; Xbar=Xf / (K + Xf); Xt=Xf+Xbar*Mtot; P=Bmax *Xbar; 0<Xf<Xt (P represents the fluorescence polarization values, Xt represents total $[Hsp104]_6$, Xf represents free $[Hsp104]_6$, Xbar represents degree of binding, and Mtot represents total [casein]).

Size exclusion chromatography (SEC) analysis and purification was performed by incubating wildtype Hsp104 (20 μM) with nucleotide (ATP, ATPγS, AMPPNP or ADP at 5 mM) in the presence or absence of FITC-casein (#C0528, Sigma) in buffer containing: 20 mM Hepes (pH=7.5), 50 mM KCl, 10 mM $MgCl_2$, 1 mM DTT. Samples were subsequently separated using a Superose 6 PC 3.2/30 column (GE Healthcare) in a running buffer containing: 40 mM Hepes (pH=7.5), 40 mM KCl, 10 mM $MgCl_2$, 1 mM DTT. Fractions were analyzed by SDS-PAGE to confirm the presence of Hsp104 and casein. Of note, SEC analysis of FITC-casein alone (Figure 1B and Fig. S1A) identified a monomer peak, eluting at ~1.7 mL, and a broad oligomer peak, eluting at ~1.2 mL, which is distinguishable from the ATPγS-Hsp104 and ATPγS-Hsp104:casein peaks, which elute at ~1.3 mL. The casein oligomer is attributed to its known polymerization capability (Redwan et al., 2015) and appears to be solubilized by Hsp104 considering it is significantly diminished in the presence of Hsp104 (Figure S1). For samples subjected to cryo-EM analysis, excess nucleotide (1mM) was added following fractionation to ensure binding during grid preparations.

Cryo-EM Data Collection and 3D Reconstructions

Protein samples were diluted to ~700µg/mL and applied to glow-discharged C-Flat holey carbon grids (CF-2/1-4C-T, Protochips) following SEC fractionation or incubation with various nucleotides (when casein was not present). Samples were plunge-frozen using a vitrobot (FEI Company) and imaged as indicated (Table S1), on a Titan Krios TEM operated at 300 keV (FEI Company). Images were recorded on a K2 Summit detector (Gatan Inc.) operated in counted mode at 50,000X nominal magnification corresponding to a calibrated 1.00 Å/pixel. Dose fractionated imaging was performed by semi-automated collection methods using UCSF Image 4 (X. Li et al., 2015). Six second exposures were collected at 100 msec/frame, with a total electron dose of 48 e- per micrograph in 60 frames (Table S1). Whole-frame drift correction was performed via Unblur (Grant and Grigorieff, 2015), removing the first 2 frames of the data due to the large degree of drift. Dose weighting was applied to frames above a 30-electron total dose.

Micrographs were CTF corrected using CTFFIND4 (Rohou and Grigorieff, 2015) in Relion (Scheres, 2012)and single particles were automatically selected using Appion template picker within the Leginon pipeline (Lander et al., 2009). Templates were determined from the previously published Hsp104:AMPPNP data (Yokom et al., 2016). Initial 2D classification was performed to assess data quality and remove contamination and incomplete hexamer particles; this amounted to < 5% of the data for the Hsp104-ATPγS:casein dataset. All 3D classification and refinement steps were performed with Relion (Scheres, 2012). For the Hsp104-ATPγS:casein data, the refinement scheme and resulting data are depicted. An initial 3D refinement was performed using the Hsp104-AMPPNP structure (Yokom et al., 2016), low pass filtered to 50 Å, as an initial model. The resulting reconstruction was used as the model for refinement using the total dataset, (~460,000 single particles from 3,000 micrographs). Although this structure refined to an estimated 3.9 Å, two protomer sites were identified to be poorly resolved. Therefore, a 10-class 3D classification was performed resulting in the identification of the 'closed' and 'extended' conformations. Extensive combinations of these classes were tested by 3D refinement in order to obtain the highest resolution models. A mask around the AAA+ core, determined with Relion, was imposed during refinement to exclude the flexible NTDs and MDs and improve the resolution. Combining classes 2 and 7 yielded the highest resolution map of the closed conformation (4.0Å). Additional sub-classifications of the 'closed-state' data (combining classes: 1,2, 5-8, and 10, or classes: 1, 5, 6, 8, 10) were performed, but did not yield improvements to the final map, and no additional conformations were identified. The final map of the extended state, at 4.1 Å resolution, was achieved by combining classes 3, 4 and 9 and performing a sub-classification with 6-classes, followed by refinement of two of the resulting classes. Refinement of the total extended state particles (classes 3,4 and 9) yielded a nearly identical structure at 4.0 Å resolution however the additional classification and refinement showed improved density for the NBD2 small domain of P1 and the NBD1 of P6.

To resolve the MD conformations in the Hsp104:casein complex, all closed-state data (~231,000 particles) were re-classified into 16 classes and a closed-state map (low-pass filtered to 50 Å) with the MDs and NTDs removed served as the starting model. The 3D classes were grouped by superposition and visual comparison of the MD conformations and then combined for refinement, resulting in three final models (MD Class 1-3) (Figure 4-12). This approach was performed with the extended-state data; however, the MDs were unable to be clearly resolved for the mobile protomers and thus not refined further. For all final maps, the “Post-processing” procedure was used to generate a soft mask for the two half maps prior to FSC estimation and automated B-factor sharpening was performed with the combined maps (Table 4-1). The local resolution was estimated using ResMap (Kucukelbir et al., 2013) for the unsharpened closed and extended-state maps.

	Total	Closed	Extended	MD Class 1	MD Class 2	MD Class 3	ADP
Data Collection							
Microscope	Titan Krios						
Direct Detector	Gatan K2 Summit						
Voltage	300 kV						
Magnification	50,000x						
Pixel Size	1.00Å						
Dose Rate	4.8 electrons/pixel/sec						
Total Dose	10 per sec						
# of Frames	48 electrons						
Defocus Range	1.5-3.5 µm						
Movies Taken	2764						2422
Data Processing							
Single Particles	454,924	146,463	68,459	31,969	37,361	14,494	124,933
Symmetry	C1	C1	C1	C1	C1	C1	C1
Resolution (Unmasked)	4.19 Å	4.57 Å	4.74 Å	7.31 Å	7.53 Å	7.76 Å	6.40 Å
Resolution (Masked)	3.94 Å	4.00 Å	4.13 Å	6.73 Å	6.73 Å	6.91 Å	5.64 Å
Applied B-Factor	-200	-176	-136	-381	-446	-183	-192
Model Composition							
Residues		3485	3502	4895			3906
Nucleotides		12	12	12			12
Model Scores							
Ramachandran Outliers		0.90%	1.41%	1.75%			1.65%
Ramachandran Favored		95.21%	94.02%	92.51%			92.67%
Molprobity Score		1.81	1.92	1.88			1.84
Clashscore		8.88	9.90	7.53			6.82
Poor Rotamers		0.71%	0.67%	0.14%			0.27%
Favored Rotamers		98.59%	98.39%	98.97%			99.25%
EMBD ID		8697	8746	8745			8744
PBD ID		5VJH	5VYA	5VY9			5VY8

Table 4-1 Data collection, processing and model parameters for all reconstructions and atomic models.

Atomic Modeling

Initial rigid body fitting of a SWISS-MODEL (Biasini et al., 2014) homology model based on ClpB (pbd=1qvr) served as the starting structure for model building using the closed-state map. Sub Domains (NBD1 Large/Small and NBD2 Large/Small) were segmented and rigid body fit using UCSF Chimera's *Fit in Map* function. P4 was selected for initial modeling as it showed the best resolution among protomers. Missing pore loop residues in P4 of the closed model were built de novo using COOT(Emsley et al., 2010) and Phenix (Afonine et al., 2012). Rosetta Comparative Modeling procedures (described below) were then used for refinement to achieve the complete hexamer model (DiMaio et al., 2015; Song et al., 2013).

Template models were selected through HHsearch against full-length *S. cerevisiae* Hsp104 sequence. This sequence was threaded onto the initial model, fit by rigid body methods, and the four top-scoring matches were selected using the *partial_thread* tool within Rosetta (pbd=1qvr, 5d4w, 5kne, 1rxg). These templates were set to *template_weight=0.0* within the template mover of Rosetta CM, while our initial model was set to *template_weight=1.0*. Modeling and refinement of P4 was performed as a P3-P4 dimer within a segmented map in order to accurately build the CTD, which was not available in published structures and forms part of the protomer interface. 1000 trajectories were sampled for this P3-P4 dimer and the top 20 models, based on rosetta energy score, were inspected for convergence. An additional template was used to ensure the convergence of the NBD2 pore loop (pdb=4fcv) (Biter et al., 2012), which was added to improve further trajectories of the loop region 639-686. The converged P4 model was rigid body fit into P2, P3 and P5 without change in the NBD1-NBD2 orientation, however both P1 and P6 are in substantially different conformations compared to the P4 model and modeled independently. This was achieved by rigid body-fitting the NBD1 and NBD2 domains using UCSF Chimera and then running trajectories in Rosetta CM for the P1-P6 protomer dimer with an additional 1000 models generated to obtain an accurate final model for P1 and P6. The extended-state model was determined by docking P2-P5 from the closed state and independently modeling P1 and P6, as above.

The final protomer models were combined into the full hexamer map with ATPyS molecules docked in all 12 NBD pockets. Additional density in the channel was attributed to an unfolded polypeptide from the FITC-casein substrate. The sequence could not be resolved, therefore a poly-Alanine chain (26 and 28 residues for the closed and extended states, respectively) was modeled. The N-terminus was arbitrarily oriented towards NBD2; Hsp104 may translocate either orientation of the substrate in the NBD1-to-NBD2 direction (Doyle et al., 2007; Hattendorf, 2002; Sweeny et al., 2015). To ensure the protomer interfaces were correctly modeled, 400 trajectories were sampled on the full hexamer complex. The 20 best models, which had the lowest energy and best electron density fit, were taken for manual inspection. Models converged well in all areas and the top model was chosen for local relax to ensure proper sidechain rotamer modeling. The final closed and extended models were relaxed into training maps derived from half of the respective data and checked for overfitting by comparing the FSC against the training or test maps. All images and movies were generated using UCSF Chimera (Pettersen et al., 2004).

Open/Closed Conformational Analysis

A specific 3D classification and analysis scheme was performed to determine the fraction of open and closed hexamer populations in the presence of different nucleotides and casein for Hsp104 wildtype, T317A and N728A. 3D classification was performed for each of the datasets with Relion using the MD Class 1 closed-state reconstruction low pass filtered to 30 Å as an initial model. Data were split into 4 classes in order to properly separate the open and closed states and account for poorly-resolved data that did not classify to either state. Both the open and closed-state reconstructions were tested as initial models but only the closed-state allowed convergence to either conformation in initial test datasets. The resulting maps were fit into the closed- and open-state reconstructions, low pass filtered to 15 Å, using the *Fit in Map* function in Chimera (Pettersen et al., 2004) to determine the cross-correlation (Table 4-2). Maps with a CC value ≥ 0.93 were designated as a match to that state. Maps that compared with a CC value < 0.93 to both the open and closed states were overall poorly resolved, thus the data were not included in subsequent analysis. Notably, top-view projections of the open and closed states show clear distinguishing features, including clear differences in the channel diameter, therefore 2D classification was performed on all data sets as well to verify proper classification.

Dataset		Class 1	Class 2	Class 3	Class 4	Total
AMPPNP	Particles	42562	43654	26405	48405	161026
	Open CC	**0.98**	**0.96**	0.88	0.92	100%
	Closed CC	0.90	0.91	0.90	0.90	0%
ADP	Particles	22101	38645	19539	44649	124934
	Open CC	**0.96**	**0.98**	0.89	**0.99**	100%
	Closed CC	0.91	0.92	0.92	0.87	0%
ATP	Particles	17737	37881	10344	13195	79157
	Open CC	**0.99**	**0.99**	0.85	**0.97**	87%
	Closed CC	0.90	0.89	**0.95**	0.93	13%
ATP Casein	Particles	13966	27109	18803	17627	77505
	Open CC	0.88	**0.97**	**0.95**	**0.98**	82%
	Closed CC	**0.93**	0.89	0.90	0.90	18%
ATPγS	Particles	26688	30966	41522	35170	134346
	Open CC	0.88	**0.96**	0.87	0.86	23%
	Closed CC	**0.94**	0.90	**0.96**	**0.96**	77%
ATPγS Casein	Particles	148006	136162	115782	54986	454936
	Open CC	0.86	0.84	0.85	0.87	0%
	Closed CC	**0.97**	**0.99**	**0.97**	**0.98**	100%
ATP T317A	Particles	5952	9890	8392	7826	32060
	Open CC	**0.96**	**0.99**	0.85	**0.99**	100%
	Closed CC	0.91	0.90	0.87	0.90	0%
ATPγS T317A	Particles	10820	10143	10336	3577	34876
	Open CC	**0.95**	**0.99**	**0.98**	0.89	100%
	Closed CC	0.90	0.90	0.91	0.90	0%
ATP N728A	Particles	11977	19951	7906	16123	55957
	Open CC	**0.94**	0.88	0.91	0.87	21%
	Closed CC	0.89	**0.95**	**0.96**	**0.93**	79%
ATPγS N728A	Particles	10624	5872	9105	21211	46812
	Open CC	**0.98**	0.88	**0.93**	0.86	42%
	Closed CC	0.91	**0.93**	0.91	**0.98**	58%

Table 4-2 Cross-correlation analysis and particle distributions for the open and closed hexamer states following 3D classification

4.6 Acknowledgements

Data from this chapter was published in the article “Ratchet-like polypeptide translocation mechanism of the AAA+ disaggregase Hsp104” in *Science*, June 2017. This was a co-author publication with Stephanie Gates, both co-authors contributed to electron microscopy data collection, processing and modeling. Along with writing of the manuscript and figure generation. Additionally, this highly collaborative project would not have been successful without the contributions of members from the Southworth

and Shorter laboratories whose contributions are outlined here. Stephanie Gates designed experiments, performed cryo EM sample preparation, data collection and analysis, and wrote the manuscript; Jiabei Lin and Meredith Jackrel purified Hsp104 variants, designed and performed experiments.; Alex Rizo collected and analyzed cryo EM data; Nathan M. Kendsersky ,Courtney E. Buell and Elizabeth A. Sweeny purified Hsp104 variants, designed and performed experiments; Korrie L. Mack, Edward Chuang, Mariana P. Torrente purified Hsp104 variants; Min Su supervised cryo EM data collection; James Shorter designed experiments and edited the manuscript; Daniel Southworth designed and supervised the study and edited the manuscript. Additionally, advise was given from Janet Smith and L. Rice on preparing the manuscript for publication and Frank DiMaio helped setup Rosetta for atomic modeling.

4.7 Accession Codes

Cryo EM maps and models are deposited in the Protein Data Bank: Hsp104:casein closed state (EMDB: 8697, PDB: 5VJH), extended state (EMDB: 8746, PDB: 5VYA), and middle domain conformation (EMDB: 8745, PDB: 5VY9).

4.8 References

Abid Ali, F., Renault, L., Gannon, J., Gahlon, H.L., Kotecha, A., Zhou, J.C., Rueda, D., Costa, A., 2016. Cryo-EM structures of the eukaryotic replicative helicase bound to a translocation substrate. Nat. Commun. 7, 10708. doi:10.1038/ncomms10708

Afonine, P.V., Grosse-Kunstleve, R.W., Echols, N., Headd, J.J., Moriarty, N.W., Mustyakimov, M., Terwilliger, T.C., Urzhumtsev, A., Zwart, P.H., Adams, P.D., 2012. Towards automated crystallographic structure refinement with *phenix.refine*. Acta Crystallogr. D Biol. Crystallogr. 68, 352–367. doi:10.1107/S0907444912001308

Biasini, M., Bienert, S., Waterhouse, A., Arnold, K., Studer, G., Schmidt, T., Kiefer, F., Cassarino, T.G., Bertoni, M., Bordoli, L., Schwede, T., 2014. SWISS-MODEL: modelling protein tertiary and quaternary structure using evolutionary information. Nucleic Acids Res. 42, W252–W258. doi:10.1093/nar/gku340

Biter, A.B., Lee, S., Sung, N., Tsai, F.T.F., 2012. Structural basis for intersubunit signaling in a protein disaggregating machine. Proc. Natl. Acad. Sci. U. S. A. 109, 12515–12520. doi:10.1073/pnas.1207040109

Carroni, M., Kummer, E., Oguchi, Y., Wendler, P., Clare, D.K., Sinning, I., Kopp, J., Mogk, A., Bukau, B., Saibil, H.R., 2014. Head-to-tail interactions of the coiled-coil domains regulate ClpB activity and cooperation with Hsp70 in protein disaggregation. eLife 3. doi:10.7554/eLife.02481

DeSantis, M.E., Leung, E.H., Sweeny, E.A., Jackrel, M.E., Cushman-Nick, M., Neuhaus-Follini, A., Vashist, S., Sochor, M.A., Knight, M.N., Shorter, J., 2012. Operational plasticity enables hsp104 to disaggregate diverse amyloid and nonamyloid clients. Cell 151, 778–793. doi:10.1016/j.cell.2012.09.038

DiMaio, F., Song, Y., Li, X., Brunner, M.J., Xu, C., Conticello, V., Egelman, E., Marlovits, T., Cheng, Y., Baker, D., 2015. Atomic-accuracy models from 4.5-Å cryo-electron microscopy data with density-guided iterative local refinement. Nat. Methods 12, 361–365. doi:10.1038/nmeth.3286

Doyle, S.M., Shorter, J., Zolkiewski, M., Hoskins, J.R., Lindquist, S., Wickner, S., 2007. Asymmetric deceleration of ClpB or Hsp104 ATPase activity unleashes protein-remodeling activity. Nat. Struct. Mol. Biol. 14, 114–122. doi:10.1038/nsmb1198

Emsley, P., Lohkamp, B., Scott, W.G., Cowtan, K., 2010. Features and development of *Coot*. Acta Crystallogr. D Biol. Crystallogr. 66, 486–501. doi:10.1107/S0907444910007493

Enemark, E.J., Joshua-Tor, L., 2006. Mechanism of DNA translocation in a replicative hexameric helicase. Nature 442, 270–275. doi:10.1038/nature04943

Erzberger, J.P., Berger, J.M., 2006. EVOLUTIONARY RELATIONSHIPS AND STRUCTURAL MECHANISMS OF AAA+ PROTEINS. Annu. Rev. Biophys. Biomol. Struct. 35, 93–114. doi:10.1146/annurev.biophys.35.040405.101933

Gates, S.N., Yokom, A.L., Lin, J., Jackrel, M.E., Rizo, A.N., Kendsersky, N.M., Buell, C.E., Sweeny, E.A., Mack, K.L., Chuang, E., Torrente, M.P., Su, M., Shorter, J., Southworth, D.R., 2017. Ratchet-like polypeptide translocation mechanism of the AAA+ disaggregase Hsp104. Science. doi:10.1126/science.aan1052

Glynn, S.E., Martin, A., Nager, A.R., Baker, T.A., Sauer, R.T., 2009. Structures of asymmetric ClpX hexamers reveal nucleotide-dependent motions in a AAA+ protein-unfolding machine. Cell 139, 744–756. doi:10.1016/j.cell.2009.09.034

Grant, T., Grigorieff, N., 2015. Measuring the optimal exposure for single particle cryo-EM using a 2.6 Å reconstruction of rotavirus VP6. eLife 4, e06980. doi:10.7554/eLife.06980

Hattendorf, D.A., 2002. Cooperative kinetics of both Hsp104 ATPase domains and interdomain communication revealed by AAA sensor-1 mutants. EMBO J. 21, 12–21. doi:10.1093/emboj/21.1.12

Jackrel, M.E., DeSantis, M.E., Martinez, B.A., Castellano, L.M., Stewart, R.M., Caldwell, K.A., Caldwell, G.A., Shorter, J., 2014. Potentiated Hsp104 variants antagonize diverse proteotoxic misfolding events. Cell 156, 170–182. doi:10.1016/j.cell.2013.11.047

Jackrel, M.E., Shorter, J., 2014. Potentiated Hsp104 variants suppress toxicity of diverse neurodegenerative disease-linked proteins. Dis. Model. Mech. 7, 1175–1184. doi:10.1242/dmm.016113

Kucukelbir, A., Sigworth, F.J., Tagare, H.D., 2013. Quantifying the local resolution of cryo-EM density maps. Nat. Methods 11, 63–65. doi:10.1038/nmeth.2727

Lander, G.C., Stagg, S.M., Voss, N.R., Cheng, A., Fellmann, D., Pulokas, J., Yoshioka, C., Irving, C., Mulder, A., Lau, P.-W., Lyumkis, D., Potter, C.S., Carragher, B., 2009. Appion: an integrated, database-driven pipeline to facilitate EM image processing. J. Struct. Biol. 166, 95–102.

Lee, J., Kim, J.-H., Biter, A.B., Sielaff, B., Lee, S., Tsai, F.T.F., 2013. Heat shock protein (Hsp) 70 is an activator of the Hsp104 motor. Proc. Natl. Acad. Sci. 110, 8513–8518. doi:10.1073/pnas.1217988110

Lee, S., Sowa, M.E., Watanabe, Y., Sigler, P.B., Chiu, W., Yoshida, M., Tsai, F.T.F., 2003. The structure of ClpB: a molecular chaperone that rescues proteins from an aggregated state. Cell 115, 229–240.

Li, T., Weaver, C.L., Lin, J., Duran, E.C., Miller, J.M., Lucius, A.L., 2015. Escherichia coli ClpB is a non-processive polypeptide translocase. Biochem. J. 470, 39–52. doi:10.1042/BJ20141457

Li, X., Zheng, S., Agard, D.A., Cheng, Y., 2015. Asynchronous data acquisition and on-the-fly analysis of dose fractionated cryoEM images by UCSFImage. J. Struct. Biol. 192, 174–178. doi:10.1016/j.jsb.2015.09.003

Lum, R., Tkach, J.M., Vierling, E., Glover, J.R., 2004. Evidence for an Unfolding/Threading Mechanism for Protein Disaggregation by *Saccharomyces cerevisiae* Hsp104. J. Biol. Chem. 279, 29139–29146. doi:10.1074/jbc.M403777200

Lyubimov, A.Y., Costa, A., Bleichert, F., Botchan, M.R., Berger, J.M., 2012. ATP-dependent conformational dynamics underlie the functional asymmetry of the replicative helicase from a minimalist eukaryote. Proc. Natl. Acad. Sci. 109, 11999–12004. doi:10.1073/pnas.1209406109

Matyskiela, M.E., Lander, G.C., Martin, A., 2013. Conformational switching of the 26S proteasome enables substrate degradation. Nat. Struct. Mol. Biol. 20, 781–788. doi:10.1038/nsmb.2616

Oguchi, Y., Kummer, E., Seyffer, F., Berynskyy, M., Anstett, B., Zahn, R., Wade, R.C., Mogk, A., Bukau, B., 2012. A tightly regulated molecular toggle controls AAA+ disaggregase. Nat. Struct. Mol. Biol. 19, 1338–1346. doi:10.1038/nsmb.2441

Olivares, A.O., Nager, A.R., Iosefson, O., Sauer, R.T., Baker, T.A., 2014. Mechanochemical basis of protein degradation by a double-ring AAA+ machine. Nat. Struct. Mol. Biol. 21, 871–875. doi:10.1038/nsmb.2885

Pettersen, E.F., Goddard, T.D., Huang, C.C., Couch, G.S., Greenblatt, D.M., Meng, E.C., Ferrin, T.E., 2004. UCSF Chimera?A visualization system for exploratory research and analysis. J. Comput. Chem. 25, 1605–1612. doi:10.1002/jcc.20084

Redwan, E.M., Xue, B., Almehdar, H.A., Uversky, V.N., 2015. Disorder in milk proteins: caseins, intrinsically disordered colloids. Curr. Protein Pept. Sci. 16, 228–242.

Rohou, A., Grigorieff, N., 2015. CTFFIND4: Fast and accurate defocus estimation from electron micrographs. J. Struct. Biol. 192, 216–221. doi:10.1016/j.jsb.2015.08.008

Rosenzweig, R., Farber, P., Velyvis, A., Rennella, E., Latham, M.P., Kay, L.E., 2015. ClpB N-terminal domain plays a regulatory role in protein disaggregation. Proc. Natl. Acad. Sci. 112, E6872–E6881. doi:10.1073/pnas.1512783112

Scheres, S.H.W., 2012. RELION: Implementation of a Bayesian approach to cryo-EM structure determination. J. Struct. Biol. 180, 519–530. doi:10.1016/j.jsb.2012.09.006

Skordalakes, E., Berger, J.M., 2003. Structure of the Rho Transcription Terminator. Cell 114, 135–146. doi:10.1016/S0092-8674(03)00512-9

Śledź, P., Unverdorben, P., Beck, F., Pfeifer, G., Schweitzer, A., Förster, F., Baumeister, W., 2013. Structure of the 26S proteasome with ATP-γS bound provides insights into the mechanism of nucleotide-dependent substrate translocation. Proc. Natl. Acad. Sci. U. S. A. 110, 7264–7269. doi:10.1073/pnas.1305782110

Song, Y., DiMaio, F., Wang, R.Y.-R., Kim, D., Miles, C., Brunette, T., Thompson, J., Baker, D., 2013. High-resolution comparative modeling with RosettaCM. Struct. Lond. Engl. 1993 21, 1735–1742. doi:10.1016/j.str.2013.08.005

Sweeny, E.A., Jackrel, M.E., Go, M.S., Sochor, M.A., Razzo, B.M., DeSantis, M.E., Gupta, K., Shorter, J., 2015. The Hsp104 N-Terminal Domain Enables Disaggregase Plasticity and Potentiation. Mol. Cell 57, 836–849. doi:10.1016/j.molcel.2014.12.021

Sweeny, E.A., Shorter, J., 2016. Mechanistic and Structural Insights into the Prion-Disaggregase Activity of Hsp104. J. Mol. Biol. 428, 1870–1885. doi:10.1016/j.jmb.2015.11.016

Tessarz, P., Mogk, A., Bukau, B., 2008. Substrate threading through the central pore of the Hsp104 chaperone as a common mechanism for protein disaggregation and prion propagation. Mol. Microbiol. 68, 87–97. doi:10.1111/j.1365-2958.2008.06135.x

Thomsen, N.D., Berger, J.M., 2009. Running in Reverse: The Structural Basis for Translocation Polarity in Hexameric Helicases. Cell 139, 523–534. doi:10.1016/j.cell.2009.08.043

Torrente, M.P., Castellano, L.M., Shorter, J., 2014. Suramin inhibits Hsp104 ATPase and disaggregase activity. PloS One 9, e110115. doi:10.1371/journal.pone.0110115

Wehmer, M., Sakata, E., 2016. Recent advances in the structural biology of the 26S proteasome. Int. J. Biochem. Cell Biol. 79, 437–442. doi:10.1016/j.biocel.2016.08.008

Wendler, P., Shorter, J., Plisson, C., Cashikar, A.G., Lindquist, S., Saibil, H.R., 2007. Atypical AAA+ Subunit Packing Creates an Expanded Cavity for Disaggregation by the Protein-Remodeling Factor Hsp104. Cell 131, 1366–1377. doi:10.1016/j.cell.2007.10.047

Yokom, A.L., Gates, S.N., Jackrel, M.E., Mack, K.L., Su, M., Shorter, J., Southworth, D.R., 2016. Spiral architecture of the Hsp104 disaggregase reveals the basis for polypeptide translocation. Nat. Struct. Mol. Biol. 23, 830–837. doi:10.1038/nsmb.3277

Zhao, M., Wu, S., Zhou, Q., Vivona, S., Cipriano, D.J., Cheng, Y., Brunger, A.T., 2015. Mechanistic insights into the recycling machine of the SNARE complex. Nature 518, 61–67. doi:10.1038/nature14148

Chapter 5

Architecture of the Nitric-oxide Synthase Holoenzyme Reveals Large Conformational Changes and a Calmodulin-driven Release of the FMN Domain[1]

5.1 Abstract

Nitric oxide synthase (NOS) is required in mammals to generate NO for regulating blood pressure, synaptic response and immune defense. NOS is a large homodimer with well-characterized reductase and oxygenase domains that coordinate a multi-step, inter-domain electron transfer mechanism to oxidize L-arginine and generate NO. Ca^{2+}-calmodulin (CaM) binds between the reductase and oxygenase domains to activate NO synthesis. While NOS has long been proposed to adopt distinct conformations that alternate between interflavin and FMN-heme electron transfer steps, structures of the holoenzyme have remained elusive and the CaM-bound arrangement is unknown. Here we have applied single particle electron microscopy (EM) methods to characterize the full-length of the neuronal isoform (nNOS) complex and determine the structural mechanism of CaM activation. We have identified that nNOS adopts an

---

[1] Data in this chapter published in :
Yokom, A.L., Morishima, Y., Lau, M., Su, M., Glukhova, A., Osawa, Y., Southworth, D.R., 2014. Architecture of the Nitric-oxide Synthase Holoenzyme Reveals Large Conformational Changes and a Calmodulin-driven Release of the FMN Domain. J. Biol. Chem. 289, 16855–16865. doi:10.1074/jbc.M114.564005

ensemble of open and closed conformational states and CaM binding induces a dramatic rearrangement of the reductase domain. Our 3D reconstruction of the intact nNOS:CaM complex reveals a closed conformation and a cross-monomer arrangement with the FMN domain rotated away from the NADPH-FAD center, towards the oxygenase dimer. This work captures, for the first time, the reductase-oxygenase structural arrangement and the CaM-dependent release of the FMN domain that coordinates to drive electron transfer across the domains during catalysis.

5.2 Introduction

Nitric oxide (NO) serves fundamental roles in neurotransmission, cardiovascular function and cellular defense (Bogdan, 2001; Bredt and Snyder, 1990). The three major NOS isoforms in mammals, neuronal (nNOS), endothelial (eNOS), and inducible (iNOS), produce NO in diverse signaling pathways critical to physiology. Calmodulin (CaM) is an essential activator of NOS, binding to nNOS and eNOS in a Ca^{2+} -concentration dependent manner, but binds iNOS at all intracellular Ca^{2+} concentrations (Marletta, 1994). Dysfunctional NOS produces reactive oxygen species and lowers NO, contributing to oxidative stress in stroke, diabetes and neurodegeneration (Förstermann and Sessa, 2012).

NOS is a large (260-330 kDa) homodimer distinguished by a C-terminal reductase and N-terminal oxygenase domains that together catalyze the conversion of L-arginine (Arg) and molecular oxygen to citrulline and NO. Crystal structures of the oxygenase domain identified substrate, heme, and tetrahydrobiopterin (BH_4) binding sites that are required for oxidizing Arg during catalysis and stabilizing the dimer interface in the holoenzyme complex (Crane et al., 1998; Ghosh et al., 1999). NOS is a diflavin oxidoreductase, homologous to cytochrome P450 (CYPOR), that contains distinct FAD and FMN domains that are connected by a hinge that facilitates stepwise NADPH-FAD-FMN-heme electron transfer (Iyanagi et al., 2012). The final FMN-heme electron transfer step is rate limiting and proposed to involve a trans-monomer mechanism (Adak et al., 2001a; Miller et al., 1999). CaM interacts with a recognition sequence in a flexible region between the reductase and oxygenase domains and accelerates flavin reduction by NADPH and FMN-heme electron transfer (Craig et al., 2002; Gachhui et al., 1996).

In the nNOS reductase domain structure the FMN cofactor is buried and positioned adjacent the NADPH and FAD sites to give a 5 Å separation that would facilitate FAD-FMN electron transfer (Garcin et al., 2004). However, this orientation is not compatible for subsequent electron transfer to the heme. Kinetic and biochemical experiments have led to models proposing that the FMN subdomain rotates about the hinge in a conformational switch from a ‘shielded’ to ‘deshielded’ state where the FMN becomes accessible and transfers electrons to the oxygenase domain of the adjacent monomer (Welland et al., 2008). Although structures of CYPOR have identified flexibility about this hinge, the large change in the position of the FMN domain proposed by kinetic experiments and other models has never been observed structurally (Daff, 2010). CaM interactions increase FMN-heme electron transfer, possibly by destabilizing the shielded state through bridging contacts with the FMN or interactions with the reductase-connecting domain (CD) (Abu-Soud and Stuehr, 1993; Adak et al., 2001b; Knudsen et al., 2003; Roman et al., 2000; Xia et al., 2009). Electrostatic interactions via structural control elements in the reductase domain, including the autoinhibitory (AI) loop, C-terminal tail (CT) and CD, favor the shielded state and are proposed to become disrupted for precise release of the FMN domain during the catalytic cycle (Haque et al., 2012; Tejero et al., 2010).

The dual function of CaM in promoting both intra- and inter-domain electron transfer in nNOS indicates the CaM-bound complex is likely structurally dynamic, and can support conformational states that coordinate FAD-FMN and FMN-heme electron transfer (Panda et al., 2001; Rozhkova et al., 2002). Recent hydrogen-deuterium exchange experiments of isolated iNOS domains identify interaction surfaces between the oxygenase, FMN domain and CaM, supporting a CaM-dependent arrangement for electron transfer to the heme (Smith et al., 2013). However, structures of the full-length complex have not been solved, thus the arrangement of the reductase and oxygenase domains as well as CaM-bound conformation of the holoenzyme remain fundamental questions in understanding the NOS catalytic cycle.

Here we have characterized the structure of the nNOS holoenzyme complex by electron microscopy (EM) and identified distinct domain arrangements of the dimer and a CaM-dependent re-organization of the reductase domain that together explain the conformational changes required for FMN-heme electron transfer. 2D classification and analysis of nNOS reveals an ensemble of extended, V-shaped and closed conformations, as well as a dramatic opening of the reductase domain following CaM binding. By chemical crosslinking we stabilized nNOS:CaM in the closed conformation and performed a 3D reconstruction. In the complete 3D model, the reductase domains are positioned adjacent to the oxygenase dimer while FMN domain is rotated away from the NADPH-FAD center towards the oxygenase domain of the adjacent monomer. From this work we propose that the NO synthesis cycle involves large conformational changes that transiently position the reductase domains across the oxygenase dimer, while CaM-specific activation triggers release and rotation of the FMN subdomain to expose the flavin for electron transfer to the heme.

5.3 Results

Solution Conformation, Activity and negative-stain EM of nNOS and nNOS:CaM.

Current models indicate NO synthesis by NOS likely involves large conformational changes and CaM-dependent rearrangements to bring the reductase and oxygenase domains together (Daff, 2010). However, the architecture of the full-length NOS holoenzyme complex is unknown. To begin we examined the overall size and shape of purified, recombinant rat nNOS with and without CaM by size exclusion chromatography and multi-angle light scattering (SEC-MALS). In the absence of CaM, nNOS elutes as a single peak at 7.9 mls by SEC with an average molecular weight (M_w) of 330 kDa (Figure 5-1 left). This indicates that purified nNOS alone forms a stable dimer complex when compared to the 164 kDa M_w of the monomer calculated from the amino acid sequence (M_{waa}). Following incubation with excess CaM, a single peak elutes earlier, at 7.7 ml with a M_w of 360 kDa determined by MALS, indicating complete binding of CaM at a 2:2 ratio of nNOS to CaM when compared to the M_{waa} of 361 kDa for the holoenzyme complex. To characterize the overall shape of nNOS in solution the hydrodynamic radius (R_H) was determined by dynamic light scattering (DLS). For nNOS alone and nNOS:CaM an R_H of 85 Å and 86 Å was determined, respectively (Figure 5-1 left). Based on comparison to a known globular protein of similar size, mammalian phosphofructokinase tetramer (345 kDa), which has an R_H of 63 Å (Erickson, 2009; Paradies, 1979), nNOS is predicted to be in an elongated arrangement in solution and CaM-binding results in no significant change in the overall R_H.

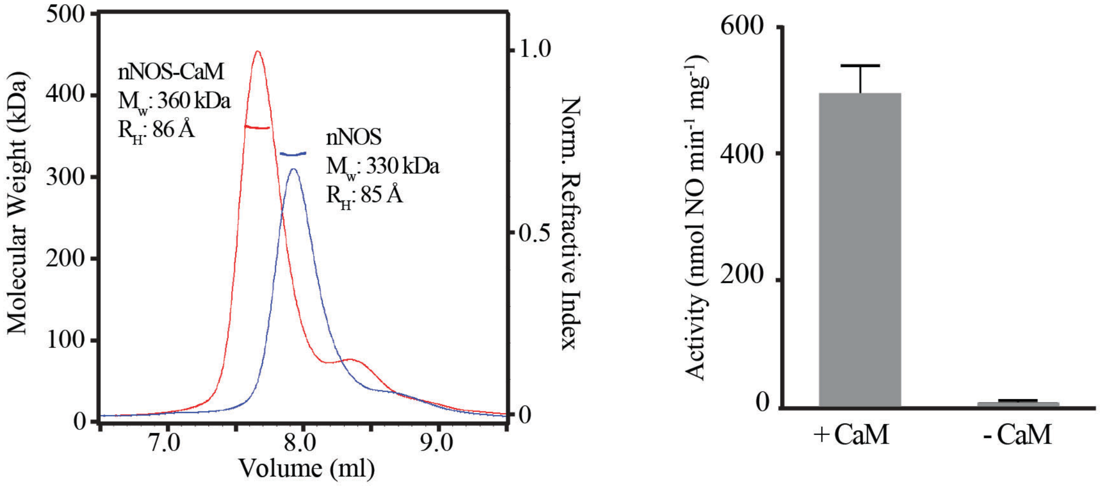

Figure 5-1 Solution analysis of nNOS and nNOS-CaM (left) SEC-MALS analysis of the nNOS dimer (blue), showing a 7.9-ml elution volume. Following incubation with CaM, the nNOS-CaM complex (red) elutes at 7.7 ml. (right) NO synthesis activity for nNOS incubated with CaM and nNOS alone, measured by the oxyhemoglobin assay. Activity assay was performed by the Osawa Lab.

NO synthesis activity was investigated by an oxyhemoglobin activity assay for these nNOS and nNOS:CaM preparations and the rates were determined to be 6 and 492 nmol NO per min per mg, respectively (Figure 5-1 right). This significant 80-fold increase in activity indicates the critical dependence on CaM binding for the catalytic activation of nNOS. Based on the unchanged elongated state of nNOS:CaM in solution it remained unclear how electron transfer could occur across the domains. We hypothesized that while the average shape of nNOS:CaM may be extended, additional conformations that support NO synthesis may exist in equilibrium.

To explore the conformation and structure of nNOS and nNOS:CaM we used single particle EM. Because of the expected flexibility of the nNOS complexes, high-contrast negative-stain methods were used. Following SEC-MALS analysis, samples were collected and immediately prepared for EM. In micrographs and single particle images, nNOS (Figure 5-2 left) and nNOS:CaM (Figure 5-2 right) were confirmed to be in an overall elongated conformation with an approximate length of 250 Å. Additional conformations were also prevalent including V-shaped structures with a variable open angle and a more compact, closed structure. This demonstrates that indeed nNOS exists in an ensemble of conformational states. The presence of saturating amounts of substrate (Arg) and active site inhibitors (N^G-hydroxy-L-Arg and 7-nitroindazole) was also tested with and without CaM, however no differences in nNOS were observed.

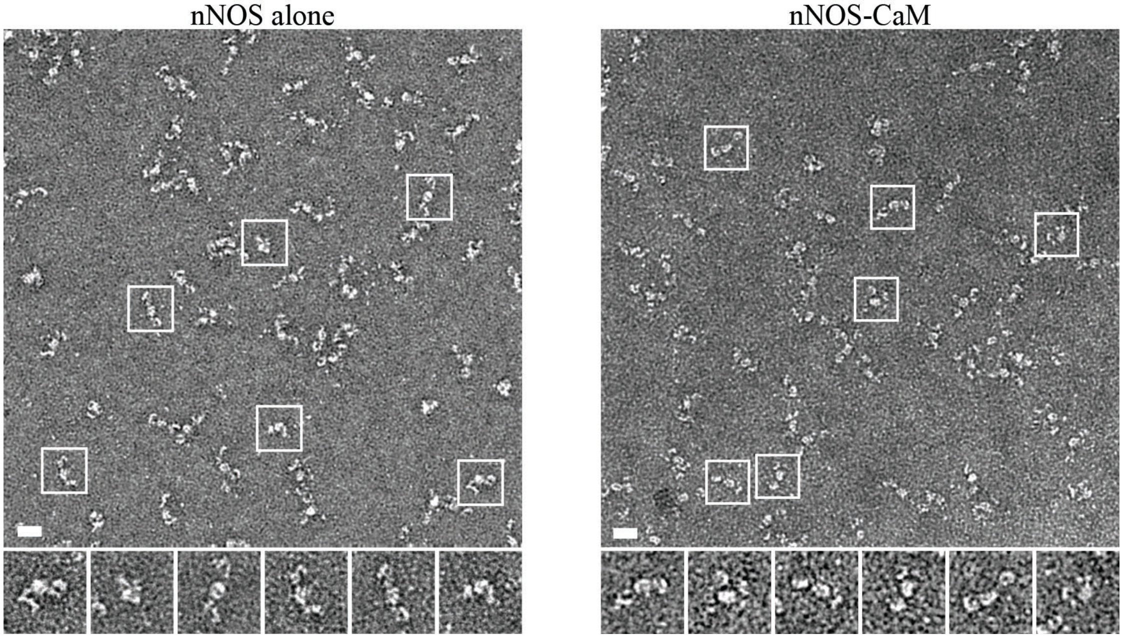

Figure 5-2 Selected negative stain micrographs of nNOS and nNOS-CaM
Representative micrograph images and boxed single particles of negatively stained nNOS (left) and nNOS-CaM (right) isolated by SEC-MALS (scale bar= 200Å)

Distinct Conformational States of nNOS and nNOS:CaM

To further characterize the conformational states of NOS and the consequence of CaM binding we collected single particle data sets of nNOS alone and nNOS:CaM and performed 2D reference-free averaging and analysis using the recently-developed ISAC method (Yang et al., 2012). Three lobes of density are well defined in the majority of 2D averages of nNOS alone, enabling domain localization based on comparisons with crystal structures (Figure 5-3). The oxygenase dimer forms a central, oval-shaped structure, while reductase domains are distal with little density connecting the domains.

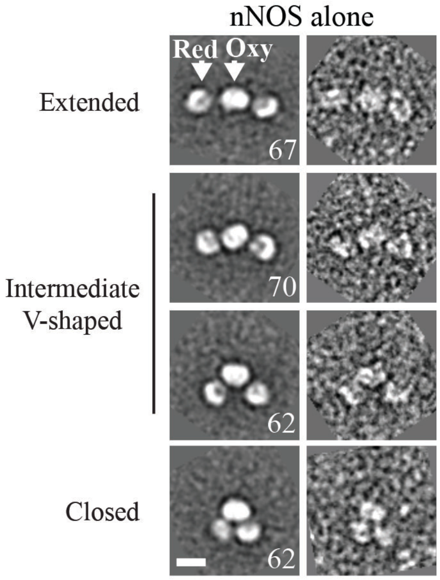

Figure 5-3 2D class averages of nNOS show conformational states
Representative averages and single particle images from each class, highlighting an extended-to-closed conformational change for the nNOS dimer. Position of the Oxy and Red domains are labeled (*scale bar* = 100 Å)

Extended, V-shaped and closed conformations are clearly apparent in the 2D averages (Figure 5-3). Notably, the V-shaped structures have a symmetrical arrangement of the reductase domains, indicating the extended-to-closed conformational change is potentially coordinated across the monomers. In the 2D averages of the nNOS:CaM complex both reductase domains are well defined and similar extended, V-shaped and closed conformations are observed. However, two significant distinctions are apparent compared to nNOS alone. First, additional density is observed between the reductase and oxygenase domains. Although small, this density is observed on both sides of the dimer and appears to increase the connectivity between the domains compared to NOS alone. This likely corresponds to CaM based on the known binding site between the domains. Difference images were generated between nNOS and nNOS:CaM in an attempt to better visualize the density, but additional conformational changes prevented precise alignment.

Secondly, in the CaM-bound complex the reductase domains are in an alternate conformational state, forming a clamp-like structure with a subdomain portion that separates and rotates away from the complex in several distinct arrangements (Figure 5-4). This large rearrangement of the reductase domain is not observed in the 2D averages of nNOS alone.

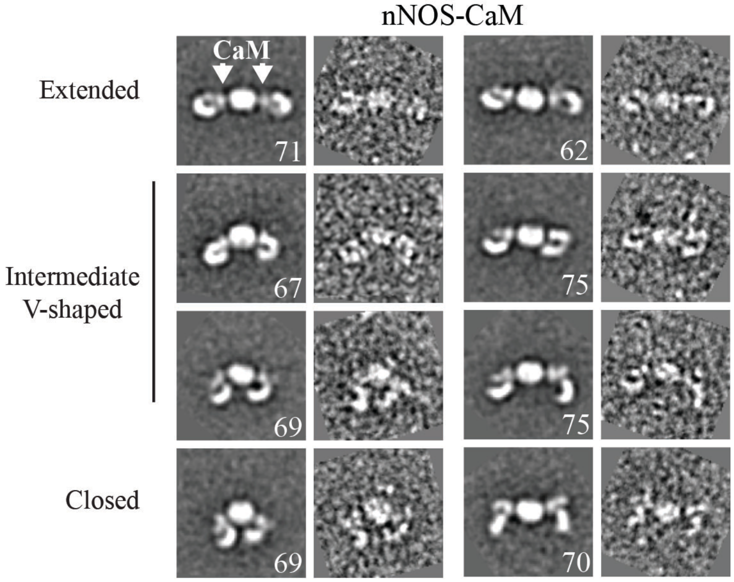

Figure 5-4 Representative 2D class averages of nNOS-CaM show domain and Red conformational changes Class averages and single particles of nNOS-CaM are shown highlighting conformational changes in the reductase domain. CaM density is label and located between the Oxy and Red domains. The number of single particle images for each average is shown (*scale bar* = 100 Å)

The overall conformational equilibrium was characterized for nNOS and nNOS:CaM by comparing the fraction of particles that adopt extended, intermediate and closed conformations, based on the 2D averages (Figure 5-5).

For nNOS alone about 40% are extended while 10% are in the closed conformation compared to 30% extended and 15% closed for nNOS:CaM. This indicates a slight shift to the closed conformation for nNOS:CaM, however both complexes are primarily in an intermediate arrangement (53% and 55%, respectively). From this we conclude that CaM-binding does not significantly alter the overall conformational equilibrium of the dimer, supporting our SEC-MALS analysis.

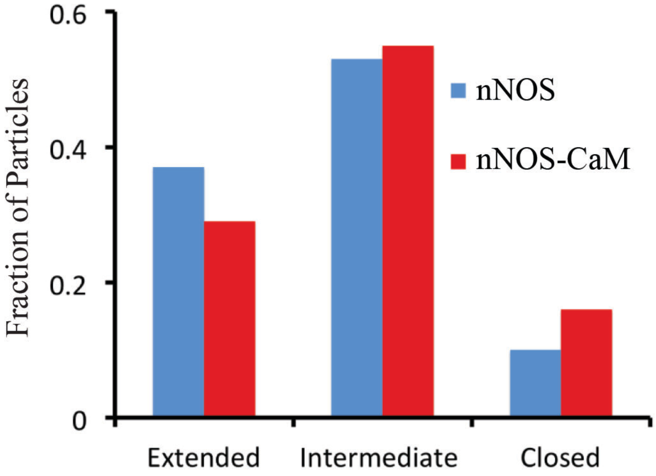

Figure 5-5 Conformational equilibrium of nNOS Bar graph showing the fraction of nNOS and nNOS-CaM single particles that adopt extended, intermediate V-shaped, or closed conformations, based on the arrangements identified in the two-dimensional averages.

For complete characterization of the changes in the reductase domain resulting from CaM binding, the entire set of class averages of nNOS alone and nNOS:CaM are shown (Figure 5-6). The reductase domains remain globular for nearly all averages of nNOS alone, but clearly adopt a variety of different structural states in the averages of the nNOS:CaM complex. While this conformational change appears symmetrical in some averages, many are asymmetric with each reductase domain adopting a different arrangement.

Furthermore, these reductase conformations are present in combination with the different extended-closed states of the dimer. Overall these results demonstrate that nNOS and nNOS:CaM undergo a large extended-to-closed conformational change that brings the reductase domains together. CaM is localized between the domains and induces a significant rearrangement of the reductase domain appearing as an opening clamp that separates the reductase domain into two distinct subdomains.

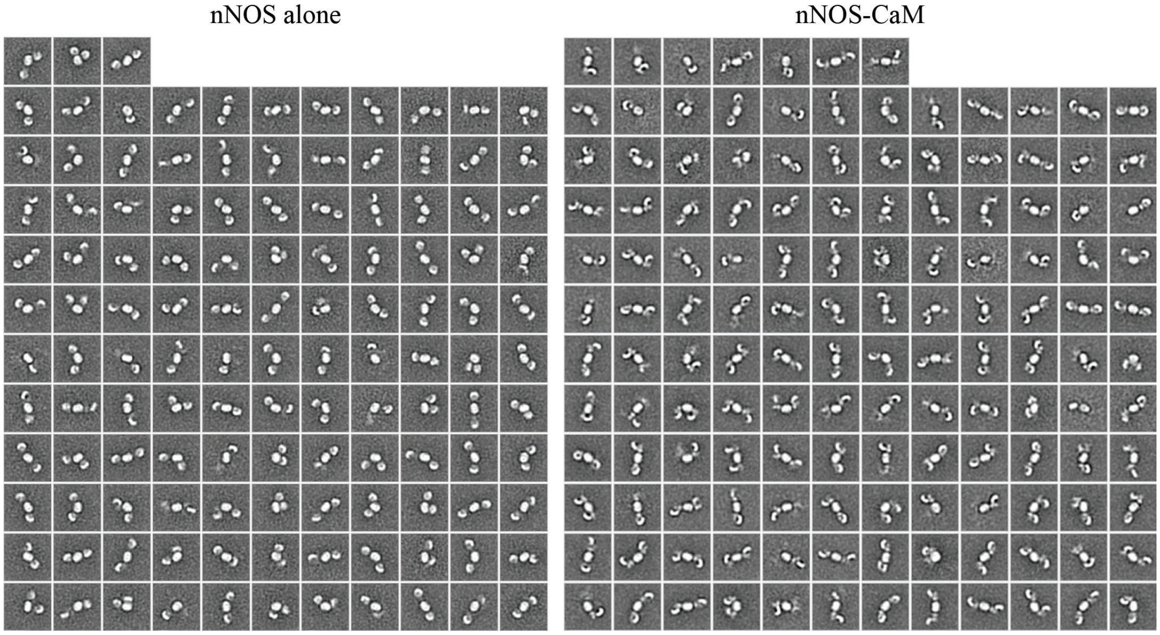

Figure 5-6 Complete set of reference-free two-dimensional class averages of nNOS and nNOS-CaM A total of 124 averages were determined from 7,326 particles for nNOS alone (*left panel*), and 139 classes were determined from 8,818 particles for nNOS-CaM (*right panel*)

Chemical Crosslinking Stabilizes nNOS:CaM in a Closed State.

While our 2D EM analysis points to significant structural changes that result from CaM binding, a 3D reconstruction was required to determine the architecture of this CaM-stabilized arrangement. However, the ensemble of different conformational states we identified presented significant challenges for determining a 3D reconstruction. Chemical crosslinking, typically with glutaraldehyde, is an established method we have used previously to stabilize a single conformation and improve homogeneity (Southworth and Agard, 2011; Stark, 2010). Therefore, we tested a glutaraldehyde crosslinking method where nNOS:CaM, isolated by SEC-MALS, was incubated with low concentrations (0.01%) of crosslinker for short time points and then quenched. Uniform crosslinking and the absence of aggregation were established by additional SEC separation of a single species (data not shown). In negative-stain micrographs and single particle images glutaraldehyde-crosslinked nNOS:CaM appeared remarkably homogeneous and in a closed conformational state (Figure 5-7).

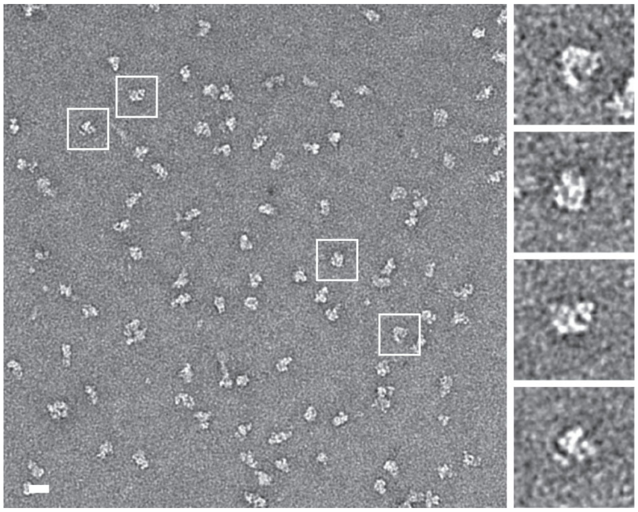

Figure 5-7 Crosslinked nNOS-CaM micrographs and single particles
nNOS-CaM cross-linked (*CXL*) with 0.01% glutaraldehyde is shown in a representative micrograph image and selected particles (scale bar=200 Å)

An initial single particle data set was collected and analyzed by reference-free 2D averaging methods. In the 2D projection averages the reductase domains are clearly identifiable in a closed arrangement adjacent the oxygenase dimer (Figure 5-8 top). This closed arrangement is similar to the small population of closed particles observed with nNOS:CaM (Figure 5-8 bottom). For the crosslinked complex the domains appear better defined with significant additional views. Crosslinked nNOS dimer alone was also tested and appeared to form a similar closed state. Because nNOS is inactive in the absence of CaM and the reductase domain rearrangement we observe was only found in the presence of CaM, additional structural characterization of the nNOS dimer alone was not performed. In previous work, crosslinking by glutaraldehyde was shown to stabilize nucleotide-dependent structural states of the heat shock protein 90 that are normally sampled during the conformational cycle (Southworth and Agard, 2008). Our data here demonstrate that crosslinking nNOS:CaM similarly captures a functional arrangement we observe in the uncrosslinked sample. Based on the shorter distance between the reductase and oxygenase domains compared to the other states, this closed conformation is the most probable arrangement for supporting a cross-monomer FMN-heme electron transfer mechanism.

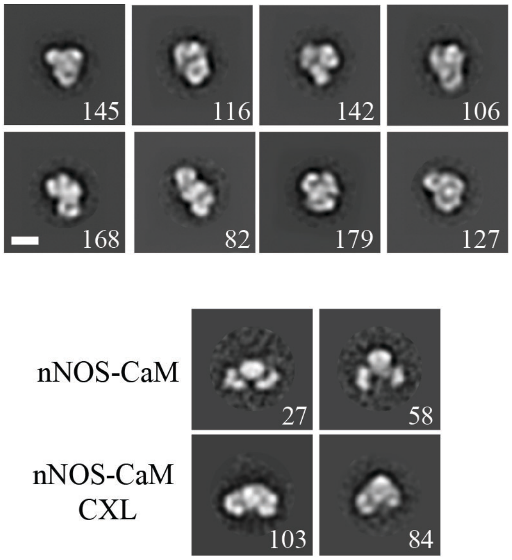

Figure 5-8 Two-dimensional reference-free averages of nNOS-CaM CXL
(top) Selected class averages with the number of single particles per average (*scale bar* = 100 Å). *(*bottom*)* Comparison of two-dimensional averages of uncross-linked nNOS-CaM in the closed conformation and nNOS-CaM CXL, following two-dimensional alignment.

3D EM Reconstruction of nNOS:CaM Identifies a Closed, Cross-Monomer Arrangement.

From our 2D analysis, the crosslinked nNOS:CaM complex appeared homogenous and adopted multiple orientations with clearly defined features, making it suitable for 3D reconstruction methods. To achieve an accurate 3D initial model we relied on the random conical tilt (RCT) method, where a 3D reconstruction from a single 2D class is determined from data tilted to 60° (Radermacher et al., 1987). We utilized this method to compare several reconstructions from different classes without imposing symmetry to generate unbiased initial models. The RCT models were then used as starting models in 3D refinements carried out with the entire untilted dataset. As with our initial 2D analysis above, untilted projection averages showed that the particles adopt multiple orientations. Following 3D backprojection of the tilted data from well-populated classes (>200 particles) it was clear that particles that orient with “side” views with three distinct domains provided the most consistent RCT reconstruction (Figure 5-9, left). Similar RCT reconstructions were achieved from several different classes, identifying a two-fold symmetric arrangement of the complex. The model from class 13 was used for the refinements with the full data set, but all models were tested and converged similarly. 3D refinements were then carried out using the RELION method (Scheres, 2012). Projections of the final model match the reference-free averages generated independently and there is good particle distribution among the projection angles, although some views were preferred (Figure 5-9, right).

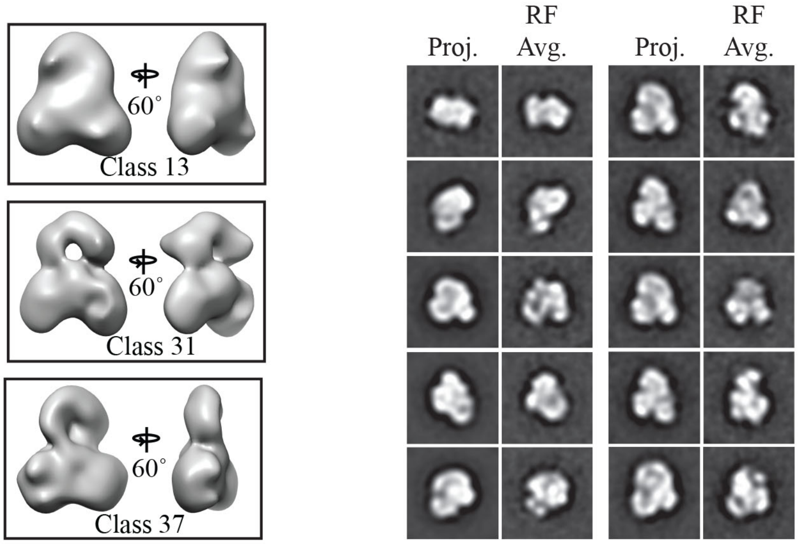

Figure 5-9 RCT initial model generation of nNOS-CaM CXL data (left) Three-dimensional RCT reconstructions, generated from tilted data corresponding to the indicated two-dimensional class. The reconstruction from class 13 was used as the starting model for additional three-dimensional refinement. (right) Two-dimensional projections (*Proj.*) of the final three-dimensional reconstruction aligned to reference-free class averages (*RF Av.*) of cross-linked nNOS-CaM.

The final 3D model was calculated to be at 23 Å resolution using the gold-standard Fourier shell correlation procedure. The model appears similar to the RCT models but with improved definition of the three lobes of density, identifying a cross-monomer arrangement (Figure 5-10).

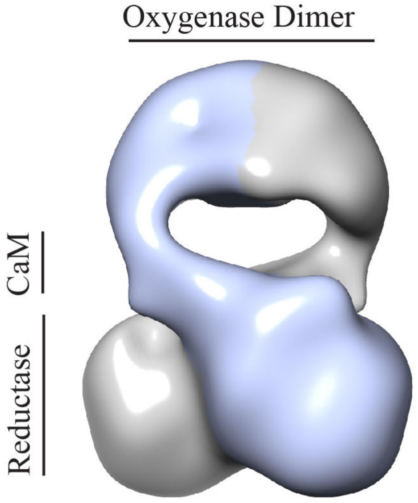

Figure 5-10 Three-dimensional model of nNOS-CaM 3D reconstruction colored along the two-fold axis to show the monomer arrangement.

In the structure a large ‘head’ domain is connected to two globular base domains by an ‘arm’ that extends across the structure, with a central space between the head and base domains. The crystal structure of the nNOS oxygenase dimer fits well into the head region of the structure with the C-terminus and α1-α2 helices aligning to where the arms project downward (Figure 5-11, left). Agreement with the crystal structure is further confirmed in a cross-section side-view that reveals a cavity that matches the solvent accessible site of the heme-binding pocket (Figure 5-11, right). Overall no significant conformational change is observed in the oxygenase dimer compared to the crystal structure. In this structural arrangement CaM is expected to be located in the connecting arms across the complex while the reductase domains are positioned adjacent the oxygenase domain of the alternate monomer.

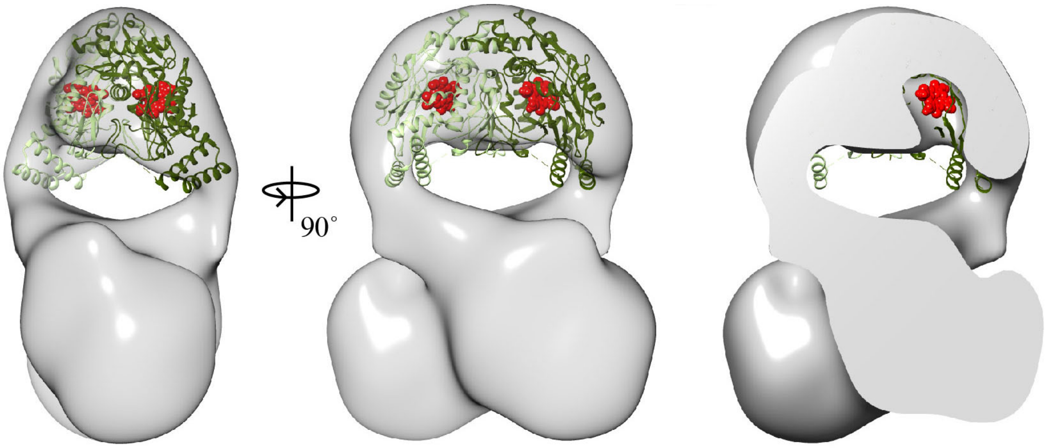

Figure 5-11 Docked Oxygenase domain of nNOS into final reconstruction
(left) The oxygenase dimer (Protein Data Bank (PDB) ID: 1RS9) docked into the EM map and locally optimized using Chimera. The heme cofactors are shown in *red*. (right*)*, cross-section view showing a pocket in the EM model that matches the location of the heme cofactor.

Molecular Model of the nNOS:CaM Complex Reveals an FMN Rotation to a Deshielded State

Next we worked to build a complete molecular model of the nNOS:CaM complex to determine whether nNOS is in a conformation that could support electron transfer across the domains. When the crystal structure of the nNOS reductase domain was docked into the EM map the NADPH and FAD domains aligned well to the curved globular base and the FMN domain was positioned above, near where the arms connect across to the oxygenase domain and where CaM is expected to be localized (Figure 5-12, left) (Garcin et al., 2004). The CaM binding helix was included in the fit and oriented based on the crystal structure of the FMN domain-CaM complex (Xia et al., 2009). In this arrangement the CaM binding helix projects away from the oxygenase domain, across the dimer in an orientation that is incompatible with the EM model. Furthermore, the FMN cofactor is positioned in the center of the reductase domain in a shielded conformation, nearly 100 Å away from the heme pocket, thus a different arrangement of the FMN domain would be required for electron transfer to the oxygenase domain.

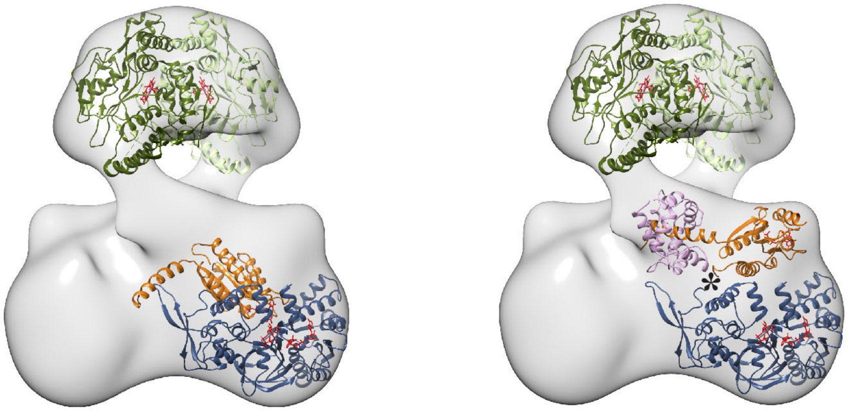

Figure 5-12 Rotation of FMN domain modeled for a single nNOS monomer (left) Fit of the reductase domain (PDB ID: 1TLL) showing the FMN domain (*orange*) in the shielded arrangement with the aligned CaM binding helix (PDB ID: 3HR4) and NADPH-FAD domains (*blue*). (right) Fit of the reductase domain with CaM (*pink*) and showing the rotation of the FMN domain around the flexible hinge (*) to a proposed FMN-released, deshielded state. Cofactors are shown in *red*.

To achieve a more accurate model, the FMN domain, including the CaM binding helix, was rotated to fit in the density that extends toward the oxygenase domain (Figure 5-12, right). This was achieved by treating residues 511-951 as a rigid body and rotating around a pivot point set in the flexible ‘hinge’ region (residues 944 - 968). Notably, there are two forms of the reductase domain in the crystal structure that are related by a minor rotation about this hinge, supporting the basis for the rotation tested here (Garcin et al., 2004). The AI helix was excluded from the fit because of its known flexibility. In this proposed deshielded state the FMN domain fits more completely into the density and the cofactor is now exposed and projects upward towards the oxygenase domain of the adjacent monomer. In addition, CaM fits into the connecting arm with the CaM binding helix oriented towards the oxygenase domain. The 29 residues between the CaM binding helix and the oxygenase domain that are missing in existing crystal structures likely make up the remaining density in the connecting arm.

When this reductase-CaM conformation is symmetrized to form a complete holoenzyme complex there are no clashes across the dimer, supporting the overall arrangement (Figure 5-13). The β-finger that includes the CD2A loop (residues 1060-1082) in the reductase domain is positioned along the two-fold axis in our model, making possible contacts across the dimer that could support this closed dimer conformation. This loop forms part of a dimer interface in the crystal form of the reductase structure and has functional roles in facilitating CaM binding and NO synthesis (Garcin et al., 2004; Knudsen et al., 2003).

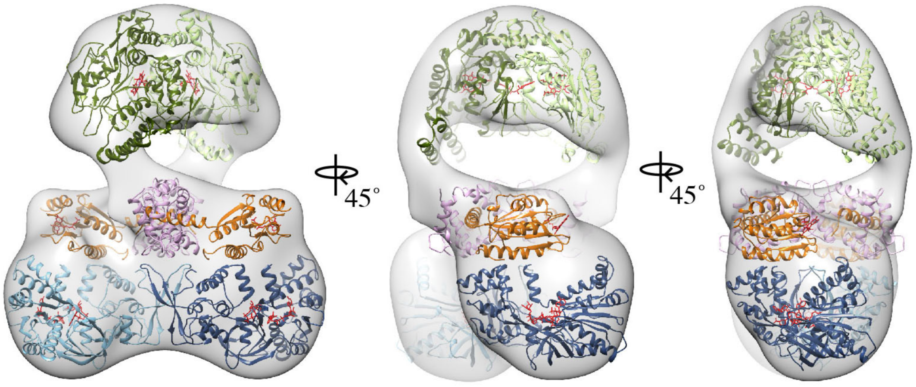

Figure 5-13 Complete molecular model the nNOS-CaM complex in the deshielded state.

The shielded-deshielded conformational change we identify here involves a large, 115° rotation of the FMN domain that re-orients the cofactor below the oxygenase domain of the adjacent monomer, at about 25 Å away (Figure 5-14, left). Importantly, this alternate reductase conformation highlights a rotation that would increase accessibility to the FMN cofactor and potentially favor electron transfer to the heme or other electron acceptors. To further verify the rotated position of the FMN domain, we compared 2D projections of our reductase-CaM deshielded model, calculated from the crystal structures, with the 2D averages of the uncrosslinked nNOS:CaM complex (Figure 5-14, right). An open clamp structure is identified in the 2D projections of the deshielded model and the conformation and position of CaM and the FMN domain agree with the 2D experimental class averages of nNOS:CaM. While a more extended reductase conformation is observed in some 2D averages, suggesting an increased rotation, the majority are similar to this open clamp structure, confirming that the proposed rotation of the FMN domain is the underlying CaM-dependent conformational change.

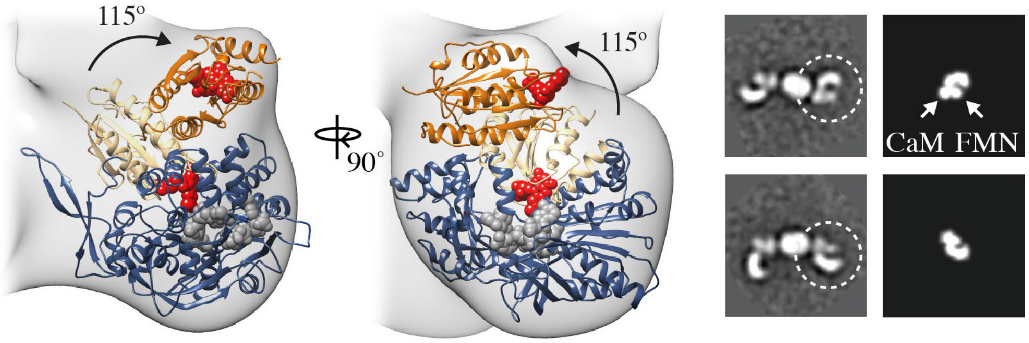

Figure 5-14 FMN deshielding compared in CXL and uncrosslinked nNOS (left) Close-up view of the reductase domain with the FMN in the shielded (*light orange*) and deshielded (*dark orange*) states indicating a 115° rotation. (right) comparison of two-dimensional averages of uncross-linked nNOS-CaM (*left panels*) and two-dimensional projections of the proposed reductase-CaM deshielded arrangement (*right panels)*

5.4 Discussion

From the data presented here we propose a model where large conformational changes of the nNOS dimer are coupled to CaM-driven release of the FMN domain during the NO synthesis cycle (Figure 5-15). In the absence of CaM, nNOS exists in an equilibrium of extended, intermediate and closed states, defined by changes in the connecting arm that alter the relative reductase-oxygenase position. The FMN domain remains protected in the shielded conformation and NO synthesis does not occur. CaM binding does not significantly change this equilibrium but induces flexibility in the reductase domain that causes the FMN domain to release and undergo a large rotation that exposes the FMN cofactor, enabling electron transfer across the domains.

Our EM structure and pseudo-atomic model of nNOS captures, for the first time, this CaM-dependent conformational change in the FMN that has been proposed in previous kinetic studies (Ilagan et al., 2008; Welland et al., 2008). Our 2D averages indicate the deshielded, FMN-released state occurs in extended, intermediate and closed dimer arrangements. Because of the long distance between the reductase and oxygenase domains in the more extended states (potentially > 100 Å) we argue FMN-heme electron transfer across the monomers would be improved in the closed state. However, given the dynamic conformations of nNOS:CaM we have identified, certain asymmetric arrangements of the complex may also facilitate FMN-heme electron transfer.

Flanking hinge elements are thought to enable the FMN to shift between shielded and deshielded states to favor respective NADPH-FAD-FMN and FMN-heme electron transfer (Haque et al., 2012). While the requirement of CaM binding is unique to NOS, flexibility of the FAD-FMN hinge has been observed in several CYPOR structures and is known to be important to catalytic function. Thus, the large rotation of the FMN we have identified here may be a conserved mechanism to control redox cycling by the oxidoreductase enzymes.

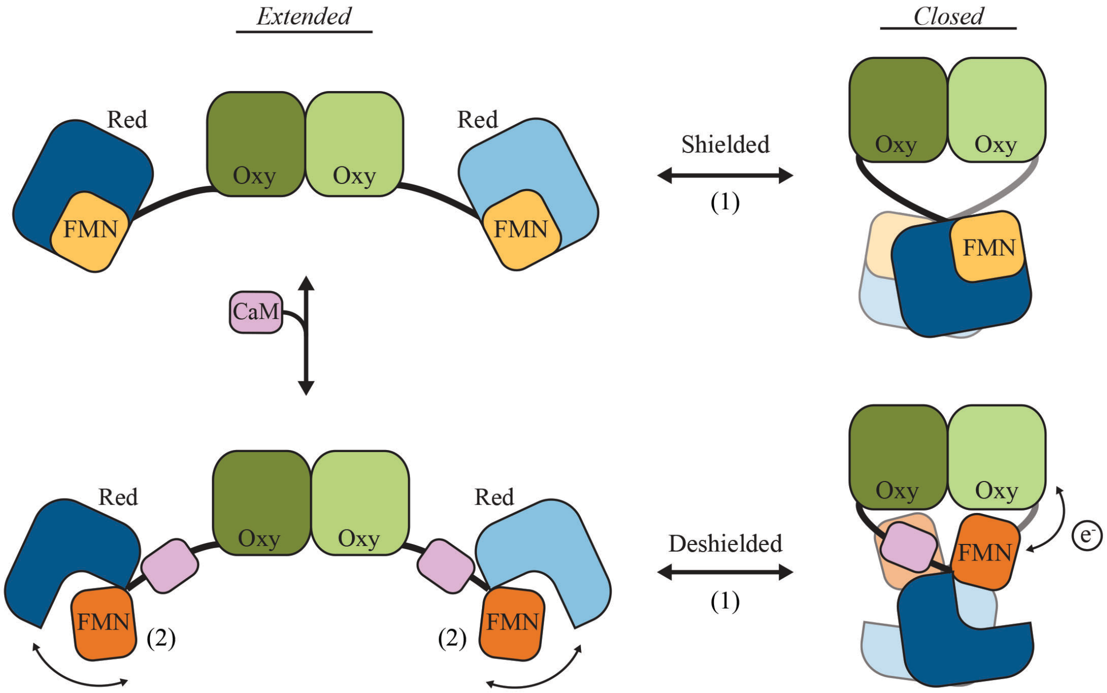

Figure 5-15 Proposed conformational model for NO synthesis by nNOS. NO synthesis involves two distinct changes in the NOS holoenzyme complex: 1) an extended-to-closed conformational equilibrium that brings the reductase domains together in a cross-monomer arrangement, and 2) release and rotation of the FMN domain triggered by CaM binding that positions the FMN cofactor for electron transfer across to the adjacent oxygenase domain in the closed state.

From our model the FMN domain does not directly contact the oxygenase domain, as proposed from previous work (Smith et al., 2013; Tejero et al., 2010). However, a minor rotation of the connecting arm would bring the domains closer and position the FMN adjacent the heme pocket. Therefore, the cross monomer arrangement and FMN domain rotation captured in the EM structure are arguably the primary conformational changes on-path for the final steps of NO synthesis. The closed conformation in the 3D reconstruction appears to be supported by additional reductase-reductase interactions based on our molecular model. While this supports a potential role for a reductase-reductase interaction in stabilizing the arrangement, previous experiments established that heterodimer complexes containing one reductase domain are catalytically active (Siddhanta et al., 1996). Therefore this interaction would not be required for synthesis, but based on our model we argue the contacts, such as through the CD2A loop (Garcin et al., 2004; Knudsen et al., 2003), could provide additional catalytic or regulatory control. Additional experiments and higher resolution structures are required to better characterize this interaction and potential function.

From the 2D classification of nNOS:CaM the reductase domain adopts several conformations, suggesting that both shielded and deshielded states are accessible in the CaM-bound state. This fits with kinetic models where CaM remains bound throughout the catalytic cycle to accelerate both interflavin and FMN-heme electron transfer steps (Abu-Soud et al., 1994). The conformational equilibrium we observe indicates that the FMN domain would be closest to the oxygenase domain of the adjacent monomer in the closed state, supporting a cross-monomer electron transfer mechanism when this conformation is sampled. While the V-shaped and closed conformations in the 2D averages appear to be symmetric, indicating a coupling between the monomers, the CaM-dependent opening of the reductase domains is largely asymmetric. Thus, the final electron transfer step may occur independently or alternate between the monomers.

A conserved reductase domain Arg residue (R753 in nNOS), identified to form a salt bridge with CaM in the iNOS FMN domain-CaM structure was shown in recent studies to be important for enhancing CaM-dependent catalytic activity (Haque et al., 2012; Panda et al., 2013; Xia et al., 2009). Our results provide additional structural framework for this interaction and support a model whereby this salt bridge and other interactions that stabilize the FMN domain-CaM arrangement function to drive the release of the FMN domain from the shielded state and stabilize the open-clamp conformation we have identified. We argue that these changes function together with the inherent extended-to-closed conformational equilibrium to transiently position the FMN adjacent to the oxygenase domain.

Finally, while the core mechanism of electron transfer is highly conserved, the NO synthesis rates vary significantly among the isoforms and have been attributed to differences in sequence elements between the domains (Ilagan et al., 2008; Roman and Masters, 2006). In particular, the 40-residue AI loop found in nNOS and eNOS affects the Ca^{2+} response in CaM binding while the CT segment has been shown to regulate multiple steps in electron transfer (Tiso et al., 2007). Structurally how these elements might control the catalytic cycle is unknown, but this could occur by altering the open-closed conformational equilibrium or FMN-release state observed with nNOS, and thus provide a unique means for regulatory control of NO synthesis for the different, isoform-specific aspects of cellular function.

5.5 Methods

Expression and Purification of nNOS and CaM

The cDNA for rat nNOS was kindly provided by Dr. S. Snyder (Johns Hopkins University). (6R)-5,6,7,8-Tetrahydro-L-biopterin (BH_4) was purchased from Dr. Schirck's Laboratory (Jona, Switzerland). Heme, ATP, creatine phosphokinase, L-arginine, N^{G}-nitro-L-arginine, and N^{G}-nitro-D-arginine were purchased from Sigma (St. Louis, MO) and creatine phosphate was from Fluka (St. Louis, MO). Untagged nNOS dimer protein was expressed using a recombinant baculovirus, Sf9 insect cell system and purified by 2',5'-ADP Sepharose and gel-filtration chromatography as described (Bender et al., 1999). Heme was added as an albumin conjugate during the expression to convert all of the nNOS to the holo-nNOS dimer. The human CaM plasmid, pACYC/trc-hCaM, was a gift from the R. Neubig lab (University of Michigan) and expression and purification was performed essentially as described (Li et al., 2008).

NOS Activity assay and SEC-MALS analysis

NO synthesis activity was determined by measuring the conversion of oxyhemoglobin to methemoglobin, as described (Bender et al., 2000). Samples were incubated at 37°C in 100 μM $CaCl_2$, 100 μM L-arginine, 100 μM BH_4, 100 units/ml catalase, 5 μg/ml CaM, 25 μM oxyhemoglobin, and an NADPH regenerating system consisting of 400 mM $NADP^+$, 10 mM glucose-6-phosphate, and 1 unit/ml glucose-6-phosphate dehydrogenase, expressed as final concentrations, in a total volume of 180 μl of 50 mM potassium phosphate, pH 7.4. The rate of oxyhemoglobin oxidation was monitored by UV absorbance (λ= 401-411 nm) with a microplate reader. The average molecular weight (M_w) and hydrodynamic radius (R_H) of nNOS and nNOS:CaM were determined by separation using a WTC-050S5 SEC column (Wyatt Technology Corporation) with an Akta micro (GE Healthcare) and analysis with a DAWN HELEOS II MALS detector equipped with a WyattQELS dynamic light scattering (DLS) detector, and Optilab rEX differential refractive index detector using ASTRA VI software (Wyatt Technology Corporation). The M_w was determined from the Raleigh ratio calculated by measuring the static light scattering and corresponding protein concentration of a selected peak. Bovine serum albumin served as a calibration standard. For SEC-MALS, 30 μM nNOS was incubated with or without 60 μM CaM for 20 minutes on ice in the running buffer, containing 20 mM HEPES, pH 7.5, 100 mM KCl, 1 mM DTT, 2 mM $CaCl_2$ and 15 μM BH_4.

EM sample preparation and data collection.

Peak fractions collected following SEC-MALS were diluted 1/20 in buffer and negatively stained with 0.75% uranyl formate (pH 5.5-6.0) on thin carbon-layered 400 mesh copper grids (Pelco) as described (Ohi et al., 2004). Chemical crosslinking was performed following SEC-MALS by incubating nNOS:CaM with 0.01% glutaraldehyde for 20 minutes then quenching with 20 mM Tris pH 7.5, as previously described (Southworth and Agard, 2008). Crosslinked nNOS:CaM was then re-purified by SEC using a Superdex 200 Precision Column (GE Healthcare) and EM grids were prepared as above. Samples were imaged under low dose conditions using a G2 Spirit TEM (FEI) operated at 120 keV. Micrographs were taken at 52,000x magnification with 2.16 Å per pixel using a 4k x 4k CCD camera (Gatan). Single particles of nNOS and nNOS:CaM were manually selected using E2boxer (EMAN2) (Tang et al., 2007)and totaled 12,207 and 13,340, respectively. Data for RCT reconstructions was collected by imaging at 0° and 60° and selecting 12,323 single particle tilt pairs using e2RCTboxer (EMAN2).

EM data processing and molecular modeling

Reference free 2D classification of uncrosslinked nNOS and nNOS:CaM was performed using the Iterative Stable Alignment and Clustering (ISAC) method (Yang et al., 2012). The total particle sets were processed through 20 initial iterations of classification then five iterations of 2-way matching, generating 124 classes from 7,326 particles for nNOS and 139 classes from 8,818 particles for nNOS:CaM. For the RCT reconstructions, reference free 2D classification of the untilted data was performed and initial 3D maps were calculated from the single classes using the corresponding tilted data with SPIDER (Frank et al., 1996; Radermacher et al., 1987). 3D refinement using the untilted data was then performed with RELION (Scheres, 2012) where the RCT model was used as an initial model, low-pass filtered to 60 Å, and two-fold symmetry was imposed. The 3D classification procedure was used with two classes and 20 rounds of refinement. The map that agreed best with the oxygenase dimer crystal structure was from 5,570 particles and selected for an additional 6 rounds of refinement using 3D auto-refine. Crystal structures were docked in the final map using Chimera, with the 'Fit in Map' command for the oxygenase dimer and manually for the reductase domain (Pettersen et al., 2004). The 'deshielded' arrangement was achieved by manually rotating the FMN domain around a pivot point between residues 944 – 968. The structure of the CaM:FMN-CaM-binding helix complex was aligned to the FMN domain and the arrangement was symmetrized for the final molecular model. The degree of rotation between the FMN positions was determined from the angle between two planes drawn through the center of the domains using Chimera.

5.6 Acknowledgements

Data presented in this chapter was published in "Architecture of the Nitric-oxide Synthase Holoenzyme Reveals Large Conformational Changes and a Calmodulin-driven Release of the FMN Domain" in the *Journal of Biological Chemistry*, April 2014. This work was done in collaboration with Yoichi Osawa's laboratory and author contributions are outline as follows. Yoshihiro Morishima and Miranda Lau purified nNOS protein and performed biochemical assays. Min

Su supervised EM data collection. Alisa Glukhova purified calmodulin. Yoichi Osawa and Daniel Southworth designed and supervised the study.

5.7 Accession Codes

The three-dimensional map (EMDB = 5940) has been deposited in the Electron Microscopy Data Bank*.*

5.8 References

Abu-Soud, H.M., Stuehr, D.J., 1993. Nitric oxide synthases reveal a role for calmodulin in controlling electron transfer. Proc. Natl. Acad. Sci. U. S. A. 90, 10769–10772.

Abu-Soud, H.M., Yoho, L.L., Stuehr, D.J., 1994. Calmodulin controls neuronal nitric-oxide synthase by a dual mechanism. Activation of intra- and interdomain electron transfer. J. Biol. Chem. 269, 32047–32050.

Adak, S., Aulak, K.S., Stuehr, D.J., 2001a. Chimeras of nitric-oxide synthase types I and III establish fundamental correlates between heme reduction, heme-NO complex formation, and catalytic activity. J. Biol. Chem. 276, 23246–23252. doi:10.1074/jbc.M102509200

Adak, S., Santolini, J., Tikunova, S., Wang, Q., Johnson, J.D., Stuehr, D.J., 2001b. Neuronal nitric-oxide synthase mutant (Ser-1412 --> Asp) demonstrates surprising connections between heme reduction, NO complex formation, and catalysis. J. Biol. Chem. 276, 1244–1252. doi:10.1074/jbc.M006857200

Bender, A.T., Nakatsuka, M., Osawa, Y., 2000. Heme insertion, assembly, and activation of apo-neuronal nitric-oxide synthase in vitro. J. Biol. Chem. 275, 26018–26023.

Bender, A.T., Silverstein, A.M., Demady, D.R., Kanelakis, K.C., Noguchi, S., Pratt, W.B., Osawa, Y., 1999. Neuronal nitric-oxide synthase is regulated by the Hsp90-based chaperone system in vivo. J. Biol. Chem. 274, 1472–1478.

Bogdan, C., 2001. Nitric oxide and the immune response. Nat. Immunol. 2, 907–916. doi:10.1038/ni1001-907

Bredt, D.S., Snyder, S.H., 1990. Isolation of nitric oxide synthetase, a calmodulin-requiring enzyme. Proc. Natl. Acad. Sci. U. S. A. 87, 682–685.

Craig, D.H., Chapman, S.K., Daff, S., 2002. Calmodulin activates electron transfer through neuronal nitric-oxide synthase reductase domain by releasing an NADPH-dependent conformational lock. J. Biol. Chem. 277, 33987–33994. doi:10.1074/jbc.M203118200

Crane, B.R., Arvai, A.S., Ghosh, D.K., Wu, C., Getzoff, E.D., Stuehr, D.J., Tainer, J.A., 1998. Structure of nitric oxide synthase oxygenase dimer with pterin and substrate. Science 279, 2121–2126.

Daff, S., 2010. NO synthase: structures and mechanisms. Nitric Oxide Biol. Chem. 23, 1–11. doi:10.1016/j.niox.2010.03.001

Erickson, H.P., 2009. Size and shape of protein molecules at the nanometer level determined by sedimentation, gel filtration, and electron microscopy. Biol. Proced. Online 11, 32–51. doi:10.1007/s12575-009-9008-x

Förstermann, U., Sessa, W.C., 2012. Nitric oxide synthases: regulation and function. Eur. Heart J. 33, 829–837, 837a–837d. doi:10.1093/eurheartj/ehr304

Frank, J., Radermacher, M., Penczek, P., Zhu, J., Li, Y., Ladjadj, M., Leith, A., 1996. SPIDER and WEB: processing and visualization of images in 3D electron microscopy and related fields. J. Struct. Biol. 116, 190–199. doi:10.1006/jsbi.1996.0030

Gachhui, R., Presta, A., Bentley, D.F., Abu-Soud, H.M., McArthur, R., Brudvig, G., Ghosh, D.K., Stuehr, D.J., 1996. Characterization of the reductase domain of rat neuronal nitric oxide synthase generated in the methylotrophic yeast Pichia pastoris. Calmodulin response is complete within the reductase domain itself. J. Biol. Chem. 271, 20594–20602.

Garcin, E.D., Bruns, C.M., Lloyd, S.J., Hosfield, D.J., Tiso, M., Gachhui, R., Stuehr, D.J., Tainer, J.A., Getzoff, E.D., 2004. Structural basis for isozyme-specific regulation of electron transfer in nitric-oxide synthase. J. Biol. Chem. 279, 37918–37927. doi:10.1074/jbc.M406204200

Ghosh, S., Wolan, D., Adak, S., Crane, B.R., Kwon, N.S., Tainer, J.A., Getzoff, E.D., Stuehr, D.J., 1999. Mutational analysis of the tetrahydrobiopterin-binding site in inducible nitric-oxide synthase. J. Biol. Chem. 274, 24100–24112.

Haque, M.M., Fadlalla, M.A., Aulak, K.S., Ghosh, A., Durra, D., Stuehr, D.J., 2012. Control of electron transfer and catalysis in neuronal nitric-oxide synthase (nNOS) by a hinge connecting its FMN and FAD-NADPH domains. J. Biol. Chem. 287, 30105–30116. doi:10.1074/jbc.M112.339697

Ilagan, R.P., Tiso, M., Konas, D.W., Hemann, C., Durra, D., Hille, R., Stuehr, D.J., 2008. Differences in a conformational equilibrium distinguish catalysis by the endothelial and neuronal nitric-oxide synthase flavoproteins. J. Biol. Chem. 283, 19603–19615. doi:10.1074/jbc.M802914200

Iyanagi, T., Xia, C., Kim, J.-J.P., 2012. NADPH-cytochrome P450 oxidoreductase: prototypic member of the diflavin reductase family. Arch. Biochem. Biophys. 528, 72–89. doi:10.1016/j.abb.2012.09.002

Knudsen, G.M., Nishida, C.R., Mooney, S.D., Ortiz de Montellano, P.R., 2003. Nitric-oxide synthase (NOS) reductase domain models suggest a new control element in endothelial NOS that attenuates calmodulin-dependent activity. J. Biol. Chem. 278, 31814–31824. doi:10.1074/jbc.M303267200

Li, H., Das, A., Sibhatu, H., Jamal, J., Sligar, S.G., Poulos, T.L., 2008. Exploring the electron transfer properties of neuronal nitric-oxide synthase by reversal of the FMN redox potential. J. Biol. Chem. 283, 34762–34772. doi:10.1074/jbc.M806949200

Marletta, M.A., 1994. Nitric oxide synthase: aspects concerning structure and catalysis. Cell 78, 927–930.

Miller, R.T., Martásek, P., Omura, T., Siler Masters, B.S., 1999. Rapid kinetic studies of electron transfer in the three isoforms of nitric oxide synthase. Biochem. Biophys. Res. Commun. 265, 184–188. doi:10.1006/bbrc.1999.1643

Ohi, M., Li, Y., Cheng, Y., Walz, T., 2004. Negative staining and image classification — powerful tools in modern electron microscopy. Biol. Proced. Online 6, 23–34. doi:10.1251/bpo70

Panda, K., Ghosh, S., Stuehr, D.J., 2001. Calmodulin activates intersubunit electron transfer in the neuronal nitric-oxide synthase dimer. J. Biol. Chem. 276, 23349–23356. doi:10.1074/jbc.M100687200

Panda, S.P., Polusani, S.R., Kellogg, D.L., Venkatakrishnan, P., Roman, M.G., Demeler, B., Masters, B.S.S., Roman, L.J., 2013. Intra- and inter-molecular effects of a conserved arginine residue of neuronal and inducible nitric oxide synthases on FMN and calmodulin binding. Arch. Biochem. Biophys. 533, 88–94. doi:10.1016/j.abb.2013.03.004

Paradies, H.H., 1979. Structure of cross-linked rabbit muscle phosphofructokinase in solution. J. Biol. Chem. 254, 7495–7504.

Pettersen, E.F., Goddard, T.D., Huang, C.C., Couch, G.S., Greenblatt, D.M., Meng, E.C., Ferrin, T.E., 2004. UCSF Chimera?A visualization system for exploratory research and analysis. J. Comput. Chem. 25, 1605–1612. doi:10.1002/jcc.20084

Radermacher, M., Wagenknecht, T., Verschoor, A., Frank, J., 1987. Three-dimensional reconstruction from a single-exposure, random conical tilt series applied to the 50S ribosomal subunit of Escherichia coli. J. Microsc. 146, 113–136.

Roman, L.J., Martásek, P., Miller, R.T., Harris, D.E., de La Garza, M.A., Shea, T.M., Kim, J.J., Masters, B.S., 2000. The C termini of constitutive nitric-oxide synthases control electron flow through the flavin and heme domains and affect modulation by calmodulin. J. Biol. Chem. 275, 29225–29232. doi:10.1074/jbc.M004766200

Roman, L.J., Masters, B.S.S., 2006. Electron transfer by neuronal nitric-oxide synthase is regulated by concerted interaction of calmodulin and two intrinsic regulatory elements. J. Biol. Chem. 281, 23111–23118. doi:10.1074/jbc.M603671200

Rozhkova, E.A., Fujimoto, N., Sagami, I., Daff, S.N., Shimizu, T., 2002. Interactions between the isolated oxygenase and reductase domains of neuronal nitric-oxide synthase: assessing the role of calmodulin. J. Biol. Chem. 277, 16888–16894. doi:10.1074/jbc.M200642200

Scheres, S.H.W., 2012. RELION: Implementation of a Bayesian approach to cryo-EM structure determination. J. Struct. Biol. 180, 519–530. doi:10.1016/j.jsb.2012.09.006

Siddhanta, U., Wu, C., Abu-Soud, H.M., Zhang, J., Ghosh, D.K., Stuehr, D.J., 1996. Heme iron reduction and catalysis by a nitric oxide synthase heterodimer containing one reductase and two oxygenase domains. J. Biol. Chem. 271, 7309–7312.

Smith, B.C., Underbakke, E.S., Kulp, D.W., Schief, W.R., Marletta, M.A., 2013. Nitric oxide synthase domain interfaces regulate electron transfer and calmodulin activation. Proc. Natl. Acad. Sci. U. S. A. 110, E3577-3586. doi:10.1073/pnas.1313331110

Southworth, D.R., Agard, D.A., 2011. Client-loading conformation of the Hsp90 molecular chaperone revealed in the cryo-EM structure of the human

Hsp90:Hop complex. Mol. Cell 42, 771–781. doi:10.1016/j.molcel.2011.04.023

Southworth, D.R., Agard, D.A., 2008. Species-dependent ensembles of conserved conformational states define the Hsp90 chaperone ATPase cycle. Mol. Cell 32, 631–640. doi:10.1016/j.molcel.2008.10.024

Stark, H., 2010. GraFix: stabilization of fragile macromolecular complexes for single particle cryo-EM. Methods Enzymol. 481, 109–126. doi:10.1016/S0076-6879(10)81005-5

Tang, G., Peng, L., Baldwin, P.R., Mann, D.S., Jiang, W., Rees, I., Ludtke, S.J., 2007. EMAN2: An extensible image processing suite for electron microscopy. J. Struct. Biol. 157, 38–46. doi:10.1016/j.jsb.2006.05.009

Tejero, J., Haque, M.M., Durra, D., Stuehr, D.J., 2010. A bridging interaction allows calmodulin to activate NO synthase through a bi-modal mechanism. J. Biol. Chem. 285, 25941–25949. doi:10.1074/jbc.M110.126797

Tiso, M., Tejero, J., Panda, K., Aulak, K.S., Stuehr, D.J., 2007. Versatile regulation of neuronal nitric oxide synthase by specific regions of its C-terminal tail. Biochemistry (Mosc.) 46, 14418–14428. doi:10.1021/bi701646k

Welland, A., Garnaud, P.E., Kitamura, M., Miles, C.S., Daff, S., 2008. Importance of the domain-domain interface to the catalytic action of the NO synthase reductase domain. Biochemistry (Mosc.) 47, 9771–9780. doi:10.1021/bi800787m

Xia, C., Misra, I., Iyanagi, T., Kim, J.-J.P., 2009. Regulation of interdomain interactions by calmodulin in inducible nitric-oxide synthase. J. Biol. Chem. 284, 30708–30717. doi:10.1074/jbc.M109.031682

Yang, Z., Fang, J., Chittuluru, J., Asturias, F.J., Penczek, P.A., 2012. Iterative stable alignment and clustering of 2D transmission electron microscope images. Struct. Lond. Engl. 1993 20, 237–247. doi:10.1016/j.str.2011.12.007

Yokom, A.L., Morishima, Y., Lau, M., Su, M., Glukhova, A., Osawa, Y., Southworth, D.R., 2014. Architecture of the Nitric-oxide Synthase Holoenzyme Reveals Large Conformational Changes and a Calmodulin-driven Release of the FMN Domain. J. Biol. Chem. 289, 16855–16865. doi:10.1074/jbc.M114.564005

Chapter 6

Discussion and Future Directions

6.1 Abstract

Work presented in this dissertation aimed to use TEM to study a vast range of conformational changes within client and chaperone protein complexes. By studying Hsp104, three unique conformational states were captured and revealed remarkable insight into the structure of Hsp104, as well as substrate binding and translocation mechanisms of AAA+ domains. Having structural information of the full-length protein proved crucial in understanding how Hsp104 functions and the impact of hyperactive point mutations. Assessing the conformational states of NOS has shown a FMN deshielding mechanism, which is required for electron transfer. By using RCT the first 3D reconstruction of nNOS demonstrated precise positioning for a 115° rotation of the FMN domain. Visualization of this flexible dimer can aid in the efforts to selectively inhibit NOS isoforms in disease and cancer. Overall this work has been successful in using TEM to study conformational changes within both chaperone and client protein complexes. Studies to further understand the complicated conformational change mechanisms of Hsp104, NOS and other proteins are outlined below.

6.2 Hsp104 open conformation

Definitive characterization of the Hsp104 disaggregase mechanism has been a long-standing goal for understanding HSP100s function. Even with a wealth of biochemical studies, conclusive structural information is critical for this goal. Cryo EM was used to determine a 3D reconstruction of the AMP-PNP Hsp104 hexamer. From this characterization, a spiral asymmetric arrangement of AAA+ domains was observed. This formed an unprecedented heteromeric AAA+ interaction between the NBD1 and NBD2 domains. Moreover, the open state revealed a distinct MD position which interacts with the NBD1 of the adjacent monomer during the ATP state.

Asymmetric AAA+ hexamers

With the advancement of EM techniques, higher resolution structural models of AAA+ domains are being determined (Blok et al., 2015; Ripstein et al., 2017; Sun et al., 2017; Zhao et al., 2015). While some AAA+ x-ray crystallography and EM structures have been determined and validated as symmetric complexes, others have been shown to be highly asymmetric. Hsp104s heteromeric AAA+ contact seems to be in a catalytically active position that could be a site of hydrolysis during the initial stages of substrate binding (Yokom et al., 2016). However, this open state of Hsp104 is different from the previously determined symmetric reconstructions. The spiral offset in Hsp104 is the most extreme case of asymmetry in AAA+ proteins, spanning across ~50Å. AAA+ machines with two AAA+ domains seem to be more prone to an asymmetric state due to the size of the complexes and flexibility between AAA+ domains. Nevertheless, single ring AAA+ domain complexes have also shown a significant degree of asymmetry. Further studies, with different nucleotides, validated the open state of Hsp104. Since this state is present with substrate and under actively hydrolyzing conditions, it is plausibly a biologically important conformation. Understanding how this asymmetric arrangement directly impacts function is an outstanding question after the discovery of this extreme asymmetry. EM is a superb structural tool for studying AAA+ structure, as it can accommodate the typical size and asymmetry of these proteins, which may preclude crystallographic studies. Further work will rely on cryo EM to dissect the open state structure and its mechanism of action.

Hsp104 resting state

The AMP-PNP open state has 11 of 12 nucleotide-binding pockets occupied and likely is in a state primed for hydrolysis. However, as mentioned earlier, we have been unable to obtain substrate binding to the open state of Hsp104. Suggesting that when disaggregase function is not required, Hsp104's open, substrate-free state may serve as a resting state of Hsp104. The conformational change induced by substrate binding is distinctive and entails a large rearrangement of AAA+ domains to a collapsed closed hexamer formation, which we determined by solving two substrate bound states (Gates et al., 2017). While our studies have only observed substrate bound in the closed and extended conformations, other type 2 AAA+ structural studies show a similar closed conformation but without substrate in the central channel (Huang et al., 2016; Ripstein et al., 2017). This could point to a difference between the various AAA+ proteins translocation mechanism and needs to be studied more in depth.

Non-processive translocation

Within the field of AAA+ translocation there is considerable debate over the possibility of both non-processive and processive translocation mechanisms. Likewise, biochemical studies have generated a variety of different step sizes for translocation (Haslberger et al., 2010; Li et al., 2015). Having captured both an open and closed state for Hsp104 may have clarified how both are possible. A non-processive step could be highly dependent on the open conformation, as suggested by the presence of the open state in the ATP samples that were tested (Gates et al., 2017). This mechanism could be specific to substrates which are only pulled free from an aggregate and not fully translocated through the central channel. Alternatively, the non-processive translocation steps could use the open to closed conformational change as a release mechanism for stalled substrates. Our study of the closed to extended conformations suggest this is a processive translocation, therefore these structures show how the Hsp104 can accommodate both non-processive and processive mechanisms, yielding a new perspective on a universal AAA+ translocation mechanism which is discussed below.

6.3 Substrate bound AAA+ complexes

Universal mechanism of AAA+ translocation

My thesis work on the substrate bound conformations of Hsp104 has led to an intricate model for AAA+ translocation (Figure 4-18). This model contains a cycling of closed and extended states to processively pull apart protein aggregates and unfold proteins. Currently there are no other published studies, that have been able to characterize the difference between these two translocation conformations. Therefore, it is enticing to think that this model is a universal aspect of AAA+ translocation, which has not yet been discovered. Observing this translocation mechanism may serve as a unifying model for all AAA+ domain translocation. However, there is a possibility that the structures of Hsp104 display a unique mechanism relative to other AAA+ domains. This difference in mechanism may accommodate the various functions of AAA+ proteins (Figure 1-11). Recent studies have shown modest resolution models for AAA+ substrate binding. Vps4, a AAA+ present in the ESCRT system, was captured bound to a 20 amino acid peptide mimicking the native Vat1 substrate (Monroe et al., 2017; Sun et al., 2017). Additionally, a AAA+ unfoldase, VAT reconstruction, was determined in an auto-translocation state where the substrate was other neighboring VAT hexamers (Huang et al., 2016; Ripstein et al., 2017). These AAA+ models show similar tyrosine pore loop positions as our Hsp104 closed state (Figure 4-4). However, neither showed evidence of the extended state. This is not to say it doesn’t exist but may have been overlooked or difficult to capture. In order to decipher the AAA+ mechanism in more detail, further structural and functional characterization of both Hsp104 and other AAA+ proteins is required.

Translocation in HSP100s

HSP100s function on a wide range of substrates but maintain a high sequence identity with Hsp104. Each member may utilize different translocation mechanisms to accommodate for the differences in substrates and activity (Gottesman et al., 1998; Haslberger et al., 2010). Obtaining structural information on ClpA, ClpB and Hsp78 will aid in understanding the mechanism of HSP100s. Furthermore, HSP100s are a class of type 2 AAA+ proteins, which contain two AAA+ rings. Dissecting substrate binding information for other type 2 AAA+ machines will serve to further deconstruct the complex translocation mechanism.

Hsp104 recruitment via Hsp70/40

Hsp70 serves as the recruitment factor for Hsp104 to insoluble protein aggregates *in vivo (Carroni et al., 2014)*. Studying this interaction has been challenging thus far, due to the nature of chaperone interactions and the dynamic nature of Hsp104. Reconstitution of the Hsp70/104 complex has not yet been achieved *in vitro* but is a critical aspect of Hsp104 biology. Work presented here has used structural information to gain immense insight into the biological function of Hsp104 alone and will be crucial in understanding how Hsp70/104 function *in vivo*.

6*.4 Future studies of Hsp104*

While the cryo EM structures of Hsp104 AMP-PNP, and Hsp104 ATPγS: casein have revealed a wealth of conformational changes present in Hsp104 the overall mechanism needs to be verified. The open state has been determined in a variety of nucleotide states (AMP, ADP, ATP, ATPγS) and is present during translocation (Figure 4-15). Studying how the open state fits into the disaggregase model for Hsp104 and other AAA+ machines is a fundamental in understanding the complete mechanism and the AMP-PNP Hsp104 model can guide these future studies. The open state AMP-PNP structure resolved incomplete densities for the tyrosine pore loops and three of six MDs. Furthermore, NTD density was of low resolution and limited our ability to analyze this region. This anisotropy in structural information is likely due to functional flexibility inherent to Hsp104. Obtaining a high-resolution model of the open conformation either in non-hydrolyzing (AMP-PNP, ADP) or hydrolyzing (ATP) samples will give more insight into the conformational changes taking place in these regulatory domains. To this end obtaining a higher resolution structure via cryo EM remains a vital prospect for further research. Cryo EM studies can use an assortment of methods, such as increasing the amount of single particle data, isolation of a static conformation by cross-linking or studying truncated Hsp104 complexes to pursue this better resolved reconstruction. Approaches such as super resolution microscopy and hydrogen deuterium exchange mass spectrometry are suitable alternatives to a higher resolution cryo EM model. *In vivo* studies of Hsp104 would aid in understanding the equilibrium of conformational states within the cellular environment providing more validation to the open state and are especially important in future studies.

Another aspect of Hsp104 function that is poorly defined is the transition between open and closed states. Isolating this transition can be a challenging task but would reveal vital aspects of the disaggregation mechanism. Studying this transition is currently outside the capabilities of cryo EM as the time scale of transition appears to be rapid. Therefore, other biochemical and structural techniques need to be employed to obtain this information. Previous strategies used to study mixed AAA+ hexamers could serve as a solution to this problem. In this system, 1-6 hydrolysis-active monomers can be inserted into the Hsp104 hexamer. By reducing the number of active protomers, the transition from open to closed may slow down or hydrolysis can be sequestered to a single monomer. The use of mutagenesis and targeted cross-linking studies based on the AMP-PNP model could also separate this transition from the closed to extended transition. Tracking the rate at which the open to closed transition occurs would be essential for *in vivo* understanding of Hsp104. Use of optical tweezer experiments would be ideal for such a study and would work in combination with a tethered Hsp104 hexamer.

Having determined the structure of substrate bound Hsp104 answered critical questions around substrate engagement to the tyrosine pore loops but has revealed new key questions. The first is how Hsp104 accommodates other substrates. It is known that Hsp104 translocates different substrates with different efficiency. Future studies can focus on capturing these substrates with Hsp104 such as RepA-GFP or Poly-A binding protein. Utilizing the power of cryo EM many substrates can be quickly screened for unique conformations similar to the 3D classification method used to sort open from closed (Figure 4-15). Hsp70 bound Hsp104 is now of major importance and should be studied alone or in conjunction with a variety of substrates. Overall, relying on cryo EM as a main structural tool is the future of dissecting the AAA+ mechanism in Hsp104 and other systems.

6.5 NOS conformational changes for regulation

There have been many structural studies of NOS domains but full-length structural information was lacking. Studying the full-length structure of nNOS via negative stain EM has advanced the understanding of the NO catalytic cycle and gave the first 3D model for nNOS (Figure 5-15). Even at the modest resolution obtained, the domain positioning of nNOS:CaM was determined and 2D classification revealed a heterogeneous position of the Red domains. Regulation by CaM binding was shown to deshield the FMN domain moving it close to the Oxy domain. This position likely allows for docking to the Oxy domain and efficient electron transfer, which are required for NO production (Smith et al., 2013).

Regulation by conformation

The range of conformational states seen by negative stain EM revealed NOS to be highly heterogeneous. This was further shown in a study from the Marletta group, which used negative stain to study all three isoforms of NOS and saw a similar heterogeneity. The NOS Red domain position may serve a regulatory role in NO production. Electron transfer is greatly decreased in the dynamic open state of NOS. Only upon CaM binding will the necessary FMN docking occur to promote electron transfer to the heme. Therefore, the regulation of this mechanism is highly reliant on both the binding of CaM as well as the region of flexibility flanking the CaM binding helix. This unstructured segment seems to play a role in conformational states. When the linker region is shortened the range of Red conformational change shrinks and could increase the amount of NO produced. There is some *in vivo* evidence for this hypothesis (Ihara et al., 2017; Jang et al., 2015). Splice variants of nNOS are expressed in differing ratios within neurons and are proposed to reduce ROS production. Interestingly, these splice variants have shortened flexible linkers. Studying these shortened nNOS variants could reveal a smaller conformational range for NOS and inform our understanding of this critical regulatory region.

6.6 Future studies of NOS flexibility

Future studies can focus on the changes in the flanking regions around the CaM binding helix. By focusing studies on this region, truncations can be used to make cryo-EM studies more straight forward and increase the structural information acquired. High-resolution structural information is needed to better characterize the NOS mechanism. Determining a structure below 10Å is a challenging task for the highly dynamic NOS dimer but is possible with the improvements of TEM. Recent unpublished cryo-EM data from our lab has revealed full-length nNOS in vitreous ice. In 2D classification, density for the Red domains is blurred suggesting the flexibly seen in negative stain EM is true in solution. Further data processing will hopefully lead to the 3D structure of this complex and give new insights into the conformational regulation of NOS.

Furthermore, studying NOS alone has yielded a wealth of knowledge, but all of the current work has been outside the scope of client-chaperone interactions. Reconstitution and study of NOS isoforms in complex with Hsp70 and Hsp90 are critical to understand the maturation and degradation pathways surrounding NOS function. This complex will be a challenging cryo EM target, since the complex will have flexibility from both NOS and the chaperones, and is known to be a transiently formed complex. Using cell biology methods this complex may pull down in immunoprecipitation methods or *in vitro* formation can be attempted. Having a stable complex will be vital for structural determination and NSEM can serve as a tool for prescreening these complexes before structure determination.

6.7 TEM a tool for studying protein conformational change

Electron Microscopy is a rapidly advancing field which is tackling structural biology questions which were previously a significant challenge. X-ray crystallography often does not have the capability to capture conformational changes in proteins. In contrast, single particle EM is a powerful tool in capturing these states. Sorting single particle data into separate conformations vastly increases the information gained from dynamic protein processes and expands our understanding of complex biological systems. Negative stain and cryo EM support structural determination techniques that can be used to study a wide range of resolutions. Even lower resolution models from NSEM can lead to great advancements in our mechanistic understanding of heterogeneous samples.

More advancements of electron microscopy

TEM has been revolutionized in recent years by the introduction of direct electron detectors, automated data collection, new microscopes and other advances. However, this technique continues to expand into uncharted territories. Cryo electron tomography aims to image proteins within the cellular environment and has begun to utilize high-resolution techniques to study structures *in vivo* and produce sub tomogram averages of structures near 10Å resolution (Dodonova et al., 2017; Turoňová et al., 2017). Additionally, phase plate technology is beginning to gain traction (Danev and Baumeister, 2017). This technique uses a thin layer of material, often carbon, to modulate the phase and contrast of an electron micrograph. This results in a boost in signal making smaller and more flexible proteins visible within the vitreous ice. The ability to study much smaller proteins with cryo EM will vastly increase the number of successful studies, high-resolution structure determination of characteristically difficult structural targets.

Direct electron detectors (DED) have proven to be critical for the rapid improvement and expansion of cryo EM. More development has been underway to further improve DEDs. Focus has been placed on improving the DQE of this next generation, allowing for collection of more data near the nyquist range.

6.8 Concluding Remarks

Utilizing EM to study Hsp104 has revealed three unique models for this dynamic protein system, which previously had no high-resolution models. Single particle analysis and 3D classification techniques were crucial for determination of these reconstructions for both substrate free and substrate bound Hsp104. The different conformational states seen clarify previous biochemical data and are a prime example of the strength of cryo EM. The AMP-PNP, open state model revealed a unique AAA+ heteromeric interaction and a spiral arrangement of AAA+ domains. Upon the addition of substrate, both closed and extended states were determined within the same sample. EM studies determined for the first time a polypeptide bound AAA+ domain and showed direct pore loop contacts. These models display a two-residue translocation step, which can function sequentially around the hexamer. The regulatory domains NTD and MD, are partially resolved and confirm the idea that they are highly mobile around the hexamer. Advancements in cryo EM techniques were vital for capturing these dynamic states and will serve as a main technique in the study of AAA+ domains moving forward.

Negative stain EM was critical for the study of the highly flexible nNOS dimer. nNOS repositions the Red domain in a wide range of positions and only by using cross-linking was a homogeneous sample obtained. By using a reference free initial model method (RCT), this cross-linked sampled led to the first full-length structure of NOS. Docking previously known crystal structures identified CaM binding to induce FMN deshielding, which is crucial for electron transfer and NO production. The capability to study proteins at modest resolutions remains a mainstay of the EM technique and yields great insight into the flexibility of protein systems.

The proteins studied all exhibit a wide degree of conformational change. In the case of Hsp104, conformational change was an ATP dependent process, while in NOS conformational change was independent of ATP but critical for function. The range of protein dynamics likely is different for every system but examining these dynamics is crucial for understanding function *in vivo*. The structures determined here have expanded our understanding of these biological systems and can serve as models for further structural and biochemical characterization. EM is a rapidly growing technique that will continue to develop and greatly improve structural biology research in the decades to come.

6.9 References

Blok, N.B., Tan, D., Wang, R.Y.-R., Penczek, P.A., Baker, D., DiMaio, F., Rapoport, T.A., Walz, T., 2015. Unique double-ring structure of the peroxisomal Pex1/Pex6 ATPase complex revealed by cryo-electron microscopy. Proc. Natl. Acad. Sci. 112, E4017–E4025. doi:10.1073/pnas.1500257112

Carroni, M., Kummer, E., Oguchi, Y., Wendler, P., Clare, D.K., Sinning, I., Kopp, J., Mogk, A., Bukau, B., Saibil, H.R., 2014. Head-to-tail interactions of the coiled-coil domains regulate ClpB activity and cooperation with Hsp70 in protein disaggregation. eLife 3. doi:10.7554/eLife.02481

Danev, R., Baumeister, W., 2017. Expanding the boundaries of cryo-EM with phase plates. Curr. Opin. Struct. Biol. 46, 87–94. doi:10.1016/j.sbi.2017.06.006

Dodonova, S.O., Aderhold, P., Kopp, J., Ganeva, I., Röhling, S., Hagen, W.J.H., Sinning, I., Wieland, F., Briggs, J.A.G., 2017. 9Å structure of the COPI coat reveals that the Arf1 GTPase occupies two contrasting molecular environments. eLife 6. doi:10.7554/eLife.26691

Gates, S.N., Yokom, A.L., Lin, J., Jackrel, M.E., Rizo, A.N., Kendsersky, N.M., Buell, C.E., Sweeny, E.A., Mack, K.L., Chuang, E., Torrente, M.P., Su, M., Shorter, J., Southworth, D.R., 2017. Ratchet-like polypeptide translocation mechanism of the AAA+ disaggregase Hsp104. Science. doi:10.1126/science.aan1052

Gottesman, S., Roche, E., Zhou, Y., Sauer, R.T., 1998. The ClpXP and ClpAP proteases degrade proteins with carboxy-terminal peptide tails added by the SsrA-tagging system. Genes Dev. 12, 1338–1347.

Haslberger, T., Bukau, B., Mogk, A., 2010. Towards a unifying mechanism for ClpB/Hsp104-mediated protein disaggregation and prion propagation. Biochem. Cell Biol. Biochim. Biol. Cell. 88, 63–75. doi:10.1139/o09-118

Huang, R., Ripstein, Z.A., Augustyniak, R., Lazniewski, M., Ginalski, K., Kay, L.E., Rubinstein, J.L., 2016. Unfolding the mechanism of the AAA+ unfoldase VAT by a combined cryo-EM, solution NMR study. Proc. Natl. Acad. Sci. U. S. A. 113, E4190-4199. doi:10.1073/pnas.1603980113

Ihara, H., Kitamura, A., Kasamatsu, S., Ida, T., Kakihana, Y., Tsutsuki, H., Sawa, T., Watanabe, Y., Akaike, T., 2017. Superoxide generation from nNOS splice variants and its potential involvement in redox signal regulation. Biochem. J. 474, 1149–1162. doi:10.1042/BCJ20160999

Jang, J.H., Kang, M.J., Ko, G.P., Kim, S.J., Yi, E.C., Zhang, Y.H., 2015. Identification of a novel splice variant of neuronal nitric oxide synthase, nNOSβ, in myofilament fraction of murine cardiomyocytes. Nitric Oxide Biol. Chem. 50, 20–27. doi:10.1016/j.niox.2015.07.005

Li, T., Weaver, C.L., Lin, J., Duran, E.C., Miller, J.M., Lucius, A.L., 2015. Escherichia coli ClpB is a non-processive polypeptide translocase. Biochem. J. 470, 39–52. doi:10.1042/BJ20141457

Monroe, N., Han, H., Shen, P.S., Sundquist, W.I., Hill, C.P., 2017. Structural basis of protein translocation by the Vps4-Vta1 AAA ATPase. eLife 6. doi:10.7554/eLife.24487

Ripstein, Z.A., Huang, R., Augustyniak, R., Kay, L.E., Rubinstein, J.L., 2017. Structure of a AAA+ unfoldase in the process of unfolding substrate. eLife 6. doi:10.7554/eLife.25754

Smith, B.C., Underbakke, E.S., Kulp, D.W., Schief, W.R., Marletta, M.A., 2013. Nitric oxide synthase domain interfaces regulate electron transfer and calmodulin activation. Proc. Natl. Acad. Sci. U. S. A. 110, E3577-3586. doi:10.1073/pnas.1313331110

Sun, S., Li, L., Yang, F., Wang, X., Fan, F., Yang, M., Chen, C., Li, X., Wang, H.-W., Sui, S.-F., 2017. Cryo-EM structures of the ATP-bound Vps4(E233Q) hexamer and its complex with Vta1 at near-atomic resolution. Nat. Commun. 8, 16064. doi:10.1038/ncomms16064

Turoňová, B., Schur, F.K.M., Wan, W., Briggs, J.A.G., 2017. Efficient 3D-CTF correction for cryo-electron tomography using NovaCTF improves subtomogram averaging resolution to 3.4Å. J. Struct. Biol. doi:10.1016/j.jsb.2017.07.007

Yokom, A.L., Gates, S.N., Jackrel, M.E., Mack, K.L., Su, M., Shorter, J., Southworth, D.R., 2016. Spiral architecture of the Hsp104 disaggregase reveals the basis for polypeptide translocation. Nat. Struct. Mol. Biol. 23, 830–837. doi:10.1038/nsmb.3277

Zhao, M., Wu, S., Zhou, Q., Vivona, S., Cipriano, D.J., Cheng, Y., Brunger, A.T., 2015. Mechanistic insights into the recycling machine of the SNARE complex. Nature 518, 61–67. doi:10.1038/nature14148